Non-ideal projection data in X-ray computed tomography

Inauguraldissertation
zur Erlangung des akademischen Grades
eines Doktors der Naturwissenschaften
der Universität Mannheim

vorgelegt von
Matthias Ebert
aus Görlitz

Mannheim, 2001

Dekan: Professor Dr. Herbert Popp, Universität Mannheim
Referent: Professor Dr. Reinhard Männer, Universität Mannheim
Korreferent: Professor Dr. Thomas Bortfeld, Boston, USA

Tag der mündlichen Prüfung: 30. Oktober 2001

Abstract

This thesis deals with various aspects of X-ray computed tomography (CT) from non-ideal projection data that do not permit the successful application of standard image reconstruction methods. A versatile calibration method was implemented allowing an adequate correction for geometric flex effects introduced by non-ideal geometry during data acquisition. A filtered back-projection algorithm was modified such that the geometric information from the calibration can be considered with high accuracy and in a computationally efficient way. The methods proposed here were evaluated by means of computer simulations and measurements using two experimental cone-beam CT scanners. Results are presented that demonstrate their excellent performance. Furthermore, a new retrospective image restoration scheme was developed in order to tackle the problem of inconsistent projection data due to internal organ motion. This scheme was applied to simulated projections as well as clinical CT data of a beating heart. The results of these investigations indicate that the image restoration approach is a promising alternative to existing, well-established image reconstruction methods if considerable organ motion occurs during data acquisition.

Zusammenfassung

Diese Arbeit behandelt verschiedene Aspekte der Röntgencomputertomographie (CT) auf Basis nicht-idealer Projektionsdaten, welche einer erfolgreichen Anwendung von etablierten Bildrekonstruktionsverfahren nicht zugänglich sind. Ein flexibles Kalibrierverfahren wurde implementiert, um eine adäquate Korrektur der durch geometrisch instabile Röntgengeräte verursachten Effekte zu ermöglichen. Ein Algorithmus zur gefilterten Rückprojektion wurde derart modifiziert, daß die von der Kalibrierung zur Verfügung gestellte, geometrische Information sowohl sehr genau als auch effizient berücksichtigt werden kann. Die ausgezeichnete Leistungsfähigkeit der Verfahren wurde durch deren Evaluation mit Hilfe von Computersimulationen und Messungen an zwei experimentellen Kegelstrahl-CT-Scannern gezeigt. Darüber hinaus wurde ein neues, retrospektives Verfahren zur Bildwiederherstellung entwickelt, um dem Problem inkonsistenter Projektionsdaten, verursacht durch die Bewegung innerer Organe, zu begegnen. Das Verfahren wurde an simulierten Projektionen und an klinischen CT-Daten eines schlagenden Herzens getestet. Die Ergebnisse dieser Untersuchungen lassen erkennen, daß der hier verfolgte Ansatz eine vielversprechende Alternative zu etablierten Bildrekonstruktionsverfahren ist, wenn während der Datenakquisition nennenswerte Organbewegungen auftreten.

Acknowledgements

I would like to thank Prof. Dr. Reinhard Männer for giving me the opportunity to do my doctorate at the faculty of mathematics and computer science of the University of Mannheim and for being the first referee of this thesis. Grateful thanks are also due to Prof. Dr. Thomas Bortfeld who had the idea for the interesting and challenging topic of this thesis. I gained a lot from being a member of his working group. I am much obliged to PD Dr. Jürgen Hesser for useful discussions and for offering me constructive criticism.

It was a great pleasure to be at the Deutsches Krebsforschungszentrum in the department headed by Prof. Dr. Wolfgang Schlegel. I would never have written this thesis if he had not stimulated my particular interest in medical imaging by the excellent lectures he gave during my university studies.

Special thanks go furthermore to PD Dr. Uwe Oelfke, Dr. Lothar Spies, Dr. Burkhard Groh and Stefan Wesarg for many inspiring discussions about my work and to Simeon Nill for solving any possible computer problem I was not able to tackle. I would also like to thank Susanne Schmitt who settled all concerns of the graduate course I took part in extremely well. The nice atmosphere in our office was very much due to Silvia Handlos. In particular, I always enjoyed our relaxing lunch and tea (or coffee) times.

I appreciate the friendship and the help provided by Dr. Mike Partridge. He was patiently answering my never ending questions regarding the English language. I gratefully thank him for carefully proofreading the manuscript and for his valuable comments.

Last but not least, I am very much indebted to my parents for their loving care and their continuous prayers during the last three years. Grateful thanks are also due to all members of my house group and many other people from my church for their friendship. They took an interest in all bright and dark periods of my PhD time and kept encouraging me, especially during the phase of writing up this thesis.

Contents

Chapter 1

Introduction

The creation of images of a patient's internal anatomy is one of the most important pillars of modern medical diagnosis. There are few persons in industrialized countries who have not been subject to one or the other medical imaging procedure at least once in their life. The use of ultrasound to monitor pregnancies and the acquisition of radiographs to visualize fractures are only two well-known examples across a wide spectrum of imaging techniques currently available.

Nowadays it is hardly recognized that there has passed only about a century since Wilhelm Conrad Röntgen pioneered the era of medical imaging with all its fascinating inventions. Before 8 November 1895, the noteworthy day he discovered the X-rays, the only way to see inside the human body had been via invasive operation. Such diagnostic interventions often posed a high risk to the patients. The enormous potential benefit of non-invasive imaging to the patient was apparent when Röntgen presented his discovery. Not surprisingly, the development of clinical radiology, once initiated, proceeded with dramatic speed.

Within a year after this breakthrough in clinical diagnosis, the need for three-dimensional imaging techniques had been voiced. Although planar radiographs were found to be satisfactory for various purposes as, for example, bone imaging, their lack of depth information was noticed immediately. Early attempts to overcome this limitation of X-ray imaging were driven by the desire to accurately localize lesions within the patient. The problem of locating embedded projectiles, escalating during the First World War, was frequently solved by one of the very first imaging methods today collectively referred to as classical tomography.

This generic term should not hide the fact that there have been proposed numerous different techniques for obtaining some kind of three-dimensional information about a patient's anatomy. The most obvious classification of these early attempts is into blurring tomography and stereo-radiography [130]. In blurring tomography, a single X-ray image is acquired in which a deliberately chosen plane of interest is more in focus than the others. This is achieved by introducing a well-defined movement of X-ray source and detector relative to the patient during exposure. The methods labelled as stereo-radiography utilize at least two planar radiographs taken with the X-ray source in different locations in order to obtain some depth information.

In fact, the techniques summarized above were able to enlarge the range of diagnostic possibilities significantly, and some of them are still in use. Nevertheless, none of these methods provides truly three-dimensional information. Using blurring tomography, the contributions of parts of the body other than the desired cross-section may be confusing, although they are smeared out. Stereo-radiography relies on the fact that corresponding points can be clearly identified in different planar X-ray images. This can be cumbersome or even impossible in practical situations.

For various reasons, it would take almost another 80 years from the discovery of X-rays until the dream of real section imaging came true. The history of this period of time regarding tomography is characterized by several independent developments. Only the most important milestones selected from the thorough review by Webb [130] are mentioned in the following.

The Bohemian mathematician Radon proved in 1917 that an N-dimensional function is uniquely determined if its integral values over all hyperplanes are available [93]. The two-dimensional case of this general mathematical framework indicates that, in principle, the linear attenuation coefficients of a body section can be calculated from the integrals along all lines through this slice of interest. Ignoring, for the moment, some physical problems related to data acquisition and the fact that an infinite number of measurements can never be recorded in practice, these line integrals are provided by X-ray transmission data. Radon's theory was first applied to radioastronomy by Bracewell in 1956 [8]. Unfortunately, there was little response to his work, and it did not influence the field of medical imaging at the time.

The idea of reconstructing the distribution of attenuation coefficients within a human body section from X-ray transmission data was first published by Cormack in 1963 [15]. He postulated that even very small attenuation differences of various soft tissue types could be distinguished, but he was never able to prove this method in practice. A long time later he heard about Radon's theory; had he been aware of this earlier, it would have saved him a lot of effort.

The first successful implementation of an X-ray computed tomography (CT) scanner was accomplished by the English engineer Hounsfield. Again, what seems to be so typical for the history of tomography, he did not know the previous work at all [50]. However, it would not be worthwhile speculating how CT developments could have gone otherwise. The use of computer technology, which had only just become available, was a mandatory precondition for Hounsfield's success in reconstructing tomograms in practice.

Hounsfield was employed by the British company EMI that had only made records and electronic devices before. The EMI scanner recorded 180 views equally spaced over an angular range of 180°, each of them comprising 160 transmission measurements along parallel stripes. Scanning time for one transverse CT slice was about 6 minutes because all of the 28,800 measurements were taken sequentially using one scintillation detector. Images were reconstructed iteratively into a matrix of 80×80 pixels [43]. The pixel size was $3 \times 3\,\mathrm{mm}^2$, the thickness of one transaxial CT slice could be chosen to be 8 mm or 13 mm [2].

On 1 October 1971 the first clinical CT scan was acquired at the Atkinson Morley's Hospital in London. The images taken of a 41 year old female, who was suspected to suffer from a tumour, showed clearly an intracranial cyst [50, 130]. When these images were presented at the 1972 British Institute of Radiology Conference, the scientific community were amazed at what had been achieved. The Nobel Prize was awarded to Hounsfield and Cormack in 1979. They are often called the pioneers of computed tomography, although there were many important contributions by other scientists.

For about two years EMI was the only company selling CT scanners. In 1974, when Siemens followed by providing a CT device, there were already 60 EMI installations. By the end of the first decade of computed tomography, there were about 10,000 installations and 18 companies selling CT scanners [50]. Many of these companies, including EMI, were not able to keep up with the competition. During these years, a lot of patents improving the basic CT principle were applied for [130]. Very soon Hounsfield proposed to collect several transmission measurements simultaneously using multiple detectors, in order to reduce scanning time. It did not take a long time for fan-beam computed tomography became the state of the art, and iterative reconstruction techniques were replaced by filtered backprojection algorithms.

After this first rapid CT boom, the 1980s turned out to be rather silent, since the peak of developments had seemed to be already reached. In 1990 Kalender suggested the introduction of the helical scanning mode in addition to the well-established slice-by-slice collection of projection data [53]. The idea of rotating the X-ray source and moving the table continuously, which results in a helical trajectory of the focus with respect to the patient, was received quite sceptically. It took some time until the clinical advantages of reduced scanning time and continuous volume coverage were realized. Nowadays, the helical mode is frequently used since it allows, for example, the acquisition of a thorax scan within a single breath-hold. Meanwhile, the compromise between avoiding organ motion artefacts at the cost of introducing some new artefacts due to the approximations required in helical reconstruction algorithms has been thoroughly investigated and is clearly understood [51, 52].

Recently, multi-row detectors became available in modern CT scanners of various manufacturers [44]. With this technique, projection data for multiple transverse slices can be acquired simultaneously which further decreases scanning time. The reconstruction algorithms applied to multi-row data are mostly two-dimensional involving some kind of interpolation into planar projections. However, these approximations are fairly reasonable, since the axial opening angle of the X-ray beam exposing, typically, four adjacent transverse slices is still rather small.

The multi-row technique may be considered an intermediate step towards truly three-dimensional computed tomography. Although the idea of cone-beam CT is not new at all, it has only recently become a promising method due to the development of flat-panel imagers [135] and cone-beam reconstruction algorithms that can be used in practice [16]. However, there are still many technical, physical and mathematical problems to be solved, in order to implement cone-beam CT clinically. Some of these challenges, especially those arising if imaging is to be combined with therapeutic intervention, are introduced more specifically in the subsequent chapter.

Chapter 2

Motivation

The role of imaging has become increasingly important, not only in diagnosis, but also for supporting demanding therapeutic interventions. In numerous applications, the accuracy of treatment could be improved by means of image-guided procedures using reliable anatomical models [45, 101].

X-ray computed tomography (CT) exhibits remarkable potential concerning image guidance due to the high geometric accuracy and spatial resolution that are achievable. Magnetic resonance imaging (MRI) can provide much better soft tissue contrast than CT. However, metallic objects close to a region of interest can cause severe distortions in the images which may be cumbersome or even impossible to correct for. Furthermore, an MRI scanner requires a static set-up, whereas a mobile X-ray C-arm device may be easily moved across different operating theatres. Alternatively, the use of ultrasound (US) seems to be very attractive, especially due to its less demanding hardware and relatively low costs. Unfortunately, the image quality is often limited by coarse resolution and low signal-to-noise ratio. Typical US artefacts can even provide valuable diagnostic information, but are undesired in image-guided procedures.

To summarize these considerations, CT is expected to become one of the most important modalities utilized at various treatment sites. In section 2.1, the role of CT is further emphasized, picking the example of image guidance in radiotherapy. There are still a lot of technical, physical and mathematical problems that need to be solved in order to exploit the full potential of CT guidance. In section 2.2, some of the current challenges regarding image reconstruction algorithms are explained. Finally, section 2.3 provides an overview about the aims of this work in facing these challenges.

2.1 Image guidance in radiotherapy

The potential of image-guidance is demonstrated in the following using its application in radiotherapy. In the next two subsections, some very basic principles of radiotherapy are explained briefly. The need for image guidance in radiotherapy and the rationale for using computed tomography for that purpose is then outlined in the third subsection.[1] Radiotherapy, however, is only one example for the importance of the implementation of image-guided procedures.

2.1.1 The principle of radiotherapy

The aim of radiotherapy in oncology is to destroy a local tumour using ionizing radiation while sparing normal tissue and, in particular, structures that are very radio-sensitive (organs at risk). There are different biological and physical principles that enable the use of ionizing radiation to affect tumours.

- Most tumour entities are more radio-sensitive than healthy tissue. This is particularly true for fast growing tumours because cell damage due to radiation manifest mainly during the replication phase.
- After irradiation, normal tissue recovers faster than tumour tissue because of more efficient repair mechanisms within the cells. Therefore, it is often advantageous to split the total dose to be delivered into several (typically about 30) daily fractions, in order to enable these repair mechanisms in healthy cells. Such a fractionated scheme also increases the probability of irradiating tumour cells during replication, which is the most radio-sensitive phase within a cell cycle.
- Furthermore, the dose delivered to the patient can be spatially conformed to the tumour target. This is achieved by choosing multiple beams which intersect in the tumour, but spare, especially, adjacent radio-sensitive structures.

The most common form of radiotherapy, which is considered here, utilizes a linear accelerator delivering photons at mean energies of 1–5 MeV. An introduction to the main steps in a typical radiotherapy planning and treatment procedure is given in the following subsection.

[1] The reader who is familiar with the field of radiotherapy may safely skip to the following section.

2.1.2 A typical radiotherapy course

Figure 2.1 shows schematically the typical steps of a fractionated course of radiotherapy (such as implemented in leading research centres and hospitals), provided the diagnosis has already been made.

First of all, the patient is adequately immobilized. For targets within the skull, an individually shaped mask made of self-hardening bandages is frequently used. Vacuum pillows are a common tool to immobilize the extracranial part of the body. Beside these two techniques, numerous other immobilization methods have been proposed [126].

The images needed for treatment planning are then acquired. X-ray CT is applied in almost all cases in order to obtain an accurate three-dimensional model of the patient's anatomy. The tumour target and the organs at risk are contoured in the CT images. A treatment plan defining the delivery technique is then carried out. Based on a physical model, the dose which would be delivered according to the plan is calculated. Normally, an iterative optimization of the treatment plan is necessary in order to achieve a good compromise between sufficient target dose coverage and sparing of radiosensitive structures.

Prior to each treatment fraction, the patient is immobilized in the same way as for imaging. Positioning at the linear accelerator is then performed using mechanical and optical tools. When an accurate set-up has been achieved, the radiation is delivered according to the treatment plan.

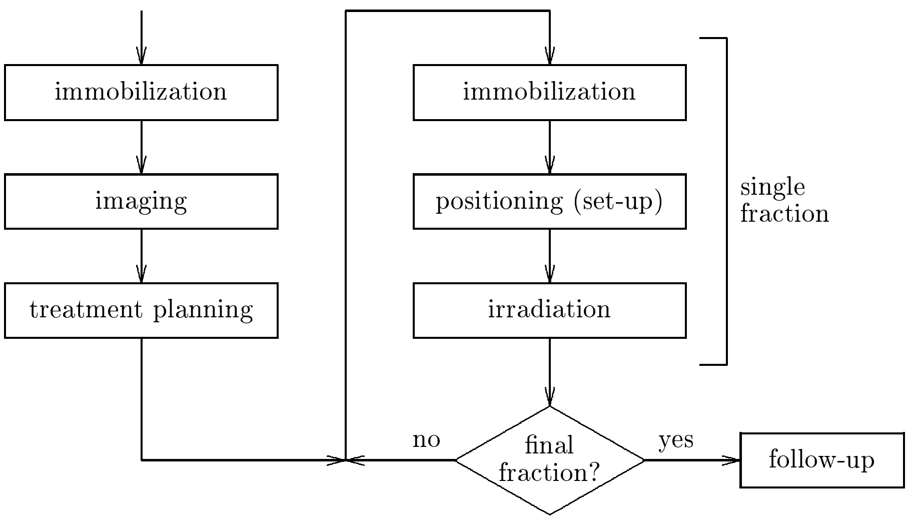

Figure 2.1: Schematic overview about a fractionated course of radiotherapy.

2.1.3 The need for image guidance

The treatment plan is normally defined once and then used in all fractions as indicated in figure 2.1. Safety margins are added to the clinical target volume (to be treated) in order to account for set-up uncertainties.h e reproducibility of patient set-up in a fractionated course of radiotherapy is often limited by the immobilization techniques which are currently available. Furthermore, the target volume and the organs at risk may move within the patient relative to bony structures and/or change its shape. These changes can be caused by gravitational effects, by variable filling of bladder, rectum or bowel as well as by tissue response to the radiation. Consequently, they affect the set-up from fraction to fraction. Figure 2.2 shows an example of anatomical changes between several fractions during a prostate treatment.

If organ motion has to be considered, the safety margins are often quite large to ensure sufficient dose coverage of the tumour. Consequently, the possible potential of modern techniques, which allow the delivery of dose distributions with very steep gradients around the target volume, may not be fully exploited in these cases. Therefore, various techniques dedicated to inter-fractional set-up verification have been suggested in the literature. They are reviewed briefly in the following paragraphs.

Numerous methods for patient set-up verification are based on (at least two, often orthogonal) X-ray transmission images taken in treatment position; see, for example, [74] and references therein. In all of these approaches, the actual transmission images are compared to digitally reconstructed radiographs which have been pre-calculated from CT planning data. Image registration algorithms utilized for this comparison involve either an itera-

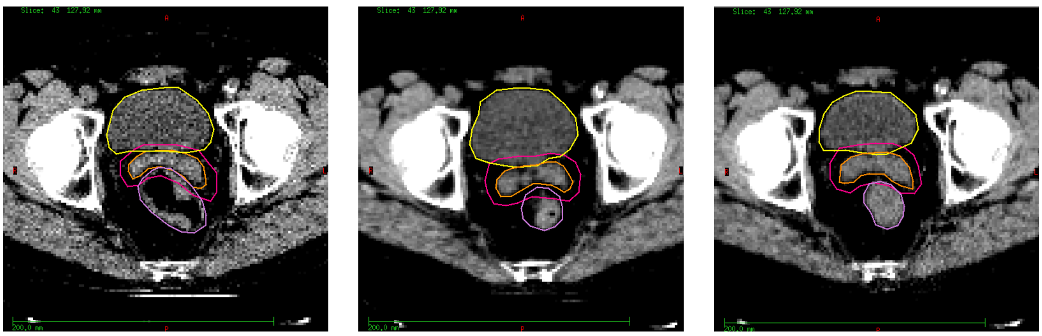

Figure 2.2: Anatomical changes between several fractions during a prostate treatment. The images were taken in weekly intervals. The contours of rectum, bladder and target volume overlaid on the CT slices show significant anatomical deviations.

tive optimization procedure [29] or the calculation of cross-correlation functions [26]. These techniques operating in projection space are well suited to inter-fractional set-up verification if the tumour and the organs at risk are not expected to move relatively to bony structures. Unfortunately, they are not applicable to targets in the abdominal region such as the prostate, since transmission images do not provide sufficient soft tissue contrast.

Alternatively, Balter et al. [4, 5] implant several radio-opaque markers transrectally in order to visualize the prostate in transmission images. Although the implantation of markers may overcome some of the limitations mentioned above, it cannot fully solve the problem. In many situations, the position, orientation and shape of the target volume might not be sufficiently determined by a few reference points.

The most promising method of overcoming the problems of the approaches described previously is the acquisition of a CT scan of the patient in treatment position, as suggested by Swindell et al. [119] originally. Various studies on image guidance in radiotherapy were presented recently; see, for example, [42, 45, 101] and references therein. The authors mention that a CT facility at a linear accelerator would be a very valuable tool for radiotherapy set-up verification. The implementation of a CT-guided procedure in fractionated radiotherapy might enable the use of tighter safety margins as well as dose escalation with potential benefit to the patient.

2.2 Problems in CT-guided procedures

X-ray projection data recorded during CT-guided procedures are often, in some sense, non-ideal. The limitations can be related to the devices used for data acquisition, to the aim of reducing dose load or to the scanning time available during an image-guided procedure. This section introduces three specific problems that are investigated in this thesis.

The following considerations are not restricted to radiotherapy, although the importance of image-guidance is explained for this example in the previous section. Similar problems arise in many other treatments as, for example, orthopaedic surgery or cardiac intervention. In all of these applications, accurate registration of the images employed in therapy planning with the actual anatomy of a patient is required, but imaging at the treatment site is subject to certain (technical) constraints.

2.2.1 Incomplete projection data

In CT-guided procedures, volumes of interest are to be scanned in short periods of time. The use of cone-beam data acquisition schemes that guarantee fast volume coverage (such as depicted in figure 3.1 on page 18) is therefore attractive.

From the technical point of view, the single-circular scan path in which the X-ray source rotates in a plane around the patient is often the only feasible one. Using existing hardware as, for example, angiography devices or linear accelerators, alternative trajectories would involve movements of a patient. This is often undesired, since a patient should be scanned exactly in treatment position. Furthermore, a synchronous movement of gantry and patient support table, as in diagnostic helical CT scanners, is not implemented in angiography devices or linear accelerators currently available.

Based on the single-circular source trajectory, mathematically exact reconstruction is possible only in the plane the source rotates in. Increasing the distance from this central plane, CT image quality is more and more deteriorated.

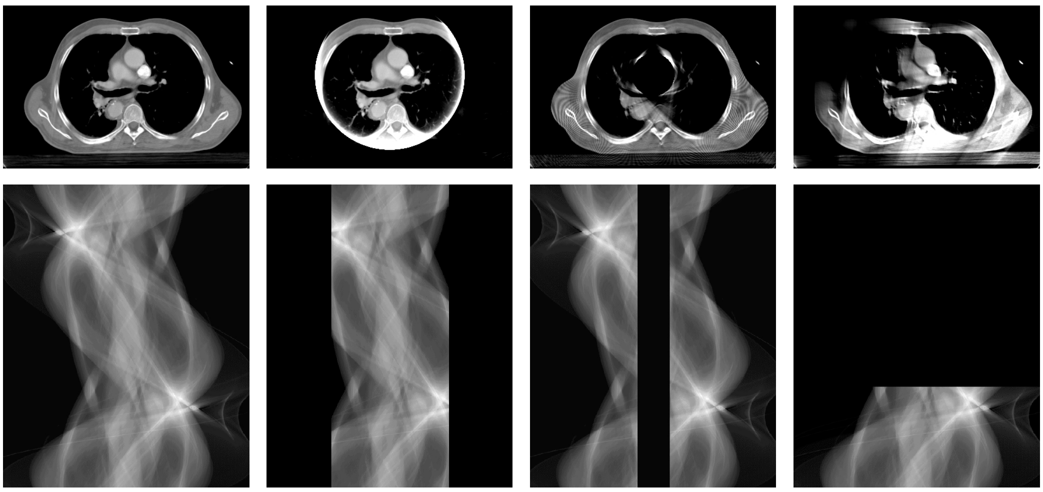

Figure 2.3: Effect of incomplete projection data. In the bottom row, the projections $g(\alpha, s)$ are displayed for complete, interior, exterior and limited-angle data (from left to right). In these sinograms, the view angle α is plotted vertically and the detector coordinate s is plotted horizontally. The value of each measured line integral is represented by a grey value from black (zero) to white (maximum line integral). Missing data are set to zero, i.e., they appear black. The corresponding images $f(\boldsymbol{r})$ reconstructed by standard filtered backprojection are depicted in the top row.

Beside this well-known incompleteness of single-circular cone-beam projections, other problems can occur in X-ray CT imaging. In the following, typical incomplete data situations are explained for parallel-beam projections for the sake of simplicity.[2] Let $f(\boldsymbol{r})$ be the object to be reconstructed and $g(\alpha, s)$ the projection data set, where α is the view angle and s is the detector coordinate.[3]

1. The *interior problem* means that $g(\alpha, s)$ is given only for $|s| \leq s_{\text{max}}$, i.e., the beam does not cover the object completely. This is often denoted as *lateral truncation* in medical applications. Of course, $f(\boldsymbol{r})$ is to be determined for $\|\boldsymbol{r}\| \leq s_{\text{max}}$ only.[4]

2. In the *exterior problem* (also denoted as *bagel problem*), $g(\alpha, s)$ is given only for $|s| \geq s_{\text{min}}$. This situation occurs if a highly absorbing structure is located inside the object such that the transmitted radiation cannot be registered by the detector. In this case, $f(\boldsymbol{r})$ is to be determined for $\|\boldsymbol{r}\| \geq s_{\text{min}}$ only.[4]

3. The *limited-angle problem* means that $g(\alpha, s)$ is given only for a set of view angles α that does not cover a range of at least π. This situation crops up if the rotation of the X-ray source is physically restricted to an angular range less than π or consistent projections of an object temporally changing cannot be collected over this range due to limited data acquisition speed.

Standard image reconstruction techniques such as filtered backprojection cannot be applied to these types of incomplete projections if a significant amount of data is missing. Figure 2.3 demonstrates the severe artefacts occurring when interior, exterior and limited-angle projections are processed by filtered backprojection.

In addition to incompleteness in mathematical sense, projection data acquired during image-guided procedures can be severely under-sampled. Frequently, the number of views recorded is far less than suggested by theoretical considerations in order to reduce scanning time and/or dose load [134]. As a consequence, a certain level of (typically streak-shaped) aliasing artefacts appearing in the CT images has to be accepted.

---

[2] Analogous considerations hold for fan-beam and cone-beam data.

[3] The view angle α utilized here replaces the direction vector $\hat{\boldsymbol{n}}$ in definition A.5 of the Radon transform; their relation is $\hat{\boldsymbol{n}} = (\cos\alpha, \sin\alpha)^{\mathrm{T}}$.

[4] A generalized investigation of this problem considering non-circular and non-centred regions in object space is not necessary for the purpose of this introduction.

2.2.2 Inconsistent projection data

The mathematical model of computed tomography relies on the fact that the object to be scanned is static. In other words, the three-dimensional distribution (of linear attenuation coefficients) is assumed to be constant while the transmission measurements are recorded. This condition is violated if the object moves or parts of the object change their geometric shape during data acquisition. Reconstructing such inconsistent projection data yields typically artefacts which are much more difficult to detect and interpret than other types like, e.g., streak artefacts.

In medical applications, movements of a patient can normally be avoided using adequate immobilization techniques. However, internal organ motion can be a serious problem if the temporal changes in the patient's anatomy are significant compared to CT scanning time. Acquisition times have been dramatically decreased in past years, and probably there is still technical potential to be exploited.

In modern diagnostic CT scanners, a full rotation of X-ray source (and detector) takes only half a second. Considering the redundancies of fan-beam geometry, a CT image can be reconstructed from projections collected over an angular range of 180° plus the aperture of the beam [75]. Using such a short-scan technique, the acquisition time is even reduced to about 300 ms. Current C-arm angiography devices allow to record about 100 cone-beam projections over a maximum angular range of 180° in less than 4 seconds. A full gantry rotation of a medical linear accelerator takes, depending on the dose rate chosen, between 1 and 2 minutes, but might be technically reduced to about 20 seconds in the future in order to allow reasonable imaging facilities.

Using up-to-date hardware as described above, a thorax scan can be performed within a single breath-hold, i.e., breathing artefacts can normally be completely avoided. CT imaging of the beating heart is, however, still one of the most challenging tasks, not only in image-guided procedures, but also in diagnostic imaging. Assuming a heart rate of 80 beats per minute,[5] the longest, nearly iso-volumetric phase lasts less than 200 ms [105]. This estimation may emphasize that heart motion is still significant with respect to the (even shortest) acquisition times mentioned above.

[5] A value of 80 beats per minute may be considered a fairly conservative estimation to illustrate the problem, since many patients exhibit higher heart rates due to a particular disease and/or psychological stress caused by the examination.

2.2.3 Geometric instabilities

Recently, angiography devices as well as linear accelerators combined with flat-panel imagers have been used for CT data acquisition in order to implement image guided procedures; see, for example, [33, 42, 45, 100, 134] and references therein. The mechanics of such devices is often not completely stable, especially if they have a C-arm shaped gantry instead of a ring gantry. There can be significant deviations from the ideal geometry desired for recording of projection data.

Such geometric misalignments, which are sometimes denoted as *flex* or *sag* effects, can cause serious artefacts in the reconstructed images if an ideal scan path is assumed and no corrections are applied. Even geometric uncertainties that are small compared to the detector pixel size can introduce noticeable artefacts [3].

Figure 2.4 shows CT slices of a humanoid phantom reconstructed assuming an ideal circular-orbit geometry, i.e., without any geometric calibration. The underlying X-ray projections were recorded using a flat-panel imager attached to the gantry of a therapy simulator such as described in subsection 4.2.2 in detail. The quality of the images is seriously degraded due to flex effects of the data acquisition system. CT slices exhibiting such significant blurring are unsuitable for image-guided procedures in which high geometric accuracy is required.

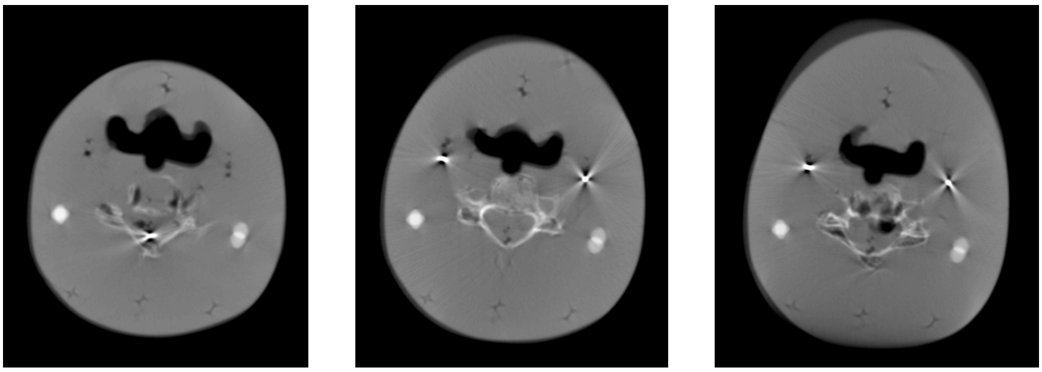

Figure 2.4: Three CT images of a humanoid phantom reconstructed without geometric calibration from projections taken at a therapy simulator.

The above example may demonstrate that a sophisticated *geometric calibration procedure* is required for reconstructing high-quality images from raw data recorded by geometrically unstable systems.

2.3 Aims of this work

The aim of this thesis is to investigate image reconstruction and restoration algorithms and their ability to operate on non-ideal projection data. The work is focused on fan-beam and cone-beam X-ray computed tomography using the third-generation scanning mode, since this is the most common data acquisition scheme in medical applications.[6]

More specifically, the three current challenges mentioned in the previous section are addressed.

1. A versatile *geometric calibration technique* that allows the correction of flex effects arising during projection data acquisition is implemented and evaluated. The method is applicable to various systems utilized in CT-guided procedures such as linear accelerators or angiography devices. Furthermore, the calibration information can be used in analytical as well as iterative image reconstruction and restoration algorithms. Beside careful simulation studies to analyse its performance, the calibration method is tested on a real C-arm device.

2. The effects caused by incomplete and/or under-sampled projection data recorded in a single-circular trajectory are investigated. The *influence of typical reconstruction artefacts* (e.g., due to aliasing, truncation and missing data) on further processing, particularly registration of various CT images, is studied.

3. The third aim of this thesis concerns inconsistent X-ray projections due to internal organ motion occurring during data acquisition. An investigation is carried out whether these inconsistencies can be corrected for retrospectively during the reconstruction step, in order to *reduce motion artefacts* in CT images. This question is studied using mathematical phantoms and real CT data of a beating heart.

Although there has been much research on CT reconstruction algorithms in recent years, these problems have not been exhaustively solved yet. This is outlined in the subsequent chapter in which the state of the art concerning X-ray computed tomography is described.

[6]CT scanning modes are introduced in section 3.1.

Chapter 3

State of the art

The purpose of this chapter is a brief literature review to enable comparisons of the actual results with those of previous work. A short, but more rigorous introduction to the theory of image reconstruction and image restoration is provided in appendix A.

As pointed out in chapter 1, different *data acquisition schemes* have been developed for X-ray computed tomography (CT), generally decreasing scanning time from one to the next generation. These schemes are sketched in section 3.1 for the reader who is not familiar with the terminology.

Section 3.2 provides an overview of some analytical *image reconstruction* methods. The description is not comprehensive, since a huge number of algorithms has been proposed in past years. The review is therefore restricted to historically important or very representative references. Techniques that are clearly not applicable to the problems of this thesis (such as analytical series expansion methods) are skipped completely.

As pointed out in the previous chapter, the reconstruction of images from incomplete projection data can be necessary for various reasons. The standard techniques such (mentioned in section 3.2) do not yield the desired results if a significant amount of projection data is missing. In this case, it is necessary to introduce prior knowledge in order to recover the object from its partial projections. Such *image restoration* methods are reviewed in section 3.3.

Section 3.4 deals with techniques for *geometric calibration* of X-ray imaging devices that have been utilized to correct for mechanical instabilities occuring during data acquisition.

3.1 Data acquisition schemes

In X-ray computed tomography, the raw data are recorded sequentially for different source and detector positions. This procedure is referred to as *scanning*. The scanning schemes that have been developed are introduced briefly in the following subsections. Although the parallel-beam schemes are not employed for practical X-ray transmission data acquisition any more, they are still of interest within theoretical framework and related to divergent-beam schemes via specific coordinate transforms.

3.1.1 Parallel-beam scanning

The very first X-ray CT scanners recorded a set of two-dimensional parallel-beam projections for each transverse slice.

In *first-generation* scanning, an X-ray source and a single detector element are translated in a straight line relative to the object in specific steps, while the line integral at each position is measured. This procedure is repeated for a large number of orientations (view angles) of the straight line with respect to the object.

In *second-generation* scanners, the single detector is replaced by an array of detector elements that record the transmission simultaneously, in order to accelerate the data acquisition. The detector array, however, is rather small such that all lines from the focus to the detector elements at a particular view angle can be considered parallel.

In a *full scan* over view angles in the range of 2π, each line integral is measured twice. The minimal complete *short-scan* data set, which allows exact image reconstruction covers an angular range of π.

3.1.2 Fan-beam scanning

A few years after the first successful CT implementation, the pencil beam was replaced by a fan beam that covers the entire object in transverse direction.

In *third-generation* scanning mode, the X-ray source and the (mostly curved) detector rotate together around the object. The number of views per full rotation is determined by the angular sampling pitch, whereas the ray sampling within each projection is given by the spacing of the detector bins.

Fourth-generation scanners employ a fixed ring of detector elements, within which the X-ray source rotates. This assembly is referred to as inverse-fan geometry, since the number of detector elements equals the number of views, each of them spanning a fan to the angular source positions.

The fourth-generation scanning mode is not generally superior to the third-generation scheme, as the names might suggest. In fact, most commercial scanners utilize the third-generation principle. This allows an effective rejection of scattered photons by using focused collimator septa between the detector elements. Furthermore, a rotating detector comprises only about a quarter of the elements of a ring detector to achieve a comparable sampling and is thus much cheaper.

In a *full scan* over 2π, each line integral is measured twice like in the parallel-beam case. The minimal complete fan-beam data set allowing an exact reconstruction covers a view angle range of π plus the aperture of the fan beam. Sometimes, this minimum range is extended by a particular over-scan. In *short-scan* data sets, some line integrals are measured twice, but others only once.

3.1.3 Cone-beam scanning

Recently, multi-row detectors have been utilized in diagnostic CT scanners, in order to further decrease the data acquisition time. For a small number of detector rows, the geometry can be sufficiently approximated by a stack of parallel fan beams. There are, however, already various CT applications employing large-area flat-panel detectors, which require an accurate consideration of the cone-beam geometry.

In pioneering theoretical work on cone-beam computed tomography the focus was assumed to meet all points of a (half) sphere around the object. Practical advances were achieved when data acquisition schemes with a one-dimensional, bounded trajectory of the focus as shown in figure 3.1 were investigated.

Concerning technical feasibility, *single-circular* and *helical source trajectories* in *third-generation* scanning mode are of major interest. The single-circular scheme, however, does not allow exact image reconstruction. This is obvious from the following necessary and sufficient condition for a complete set of cone-beam projections. Exact cone-beam reconstruction without analytical continuation is possible if and only if the focus meets every plane that intersects the object at least in one point. This *completeness condition* is

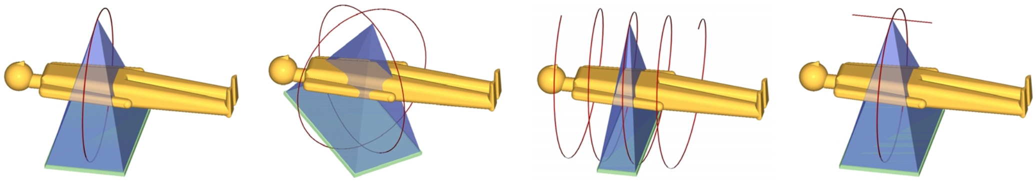

Figure 3.1: Feasible source trajectories in cone-beam computed tomography. A single-circular, a double-circular, a helical and a circle-and-line trajectory are shown schematically (from left to right).

based on the work of Tuy [124], Finch [25], Smith [112] and Grangeat [32]. Chen [13] generalized the completeness condition in order to consider local region-of-interest reconstructions.

Early investigations of cone-beam scanning schemes assume that all projections cover the entire object. In medical CT applications, this condition is clearly violated. The problem of *truncated projections* needs therefore to be solved for practical implementations. Furthermore, a particular region of interest (ROI) is often to be reconstructed. The volume exposed during scanning should not be larger (or only slightly larger) than the ROI, in order to minimize the dose load. This is known as the *long-object problem*.

3.1.4 Conclusion

In this thesis, fan-beam and cone-beam scanning in third-generation scanning mode are considered, since these are the most common schemes in medical applications. Current angiography devices or linear accelerators utilized for imaging at the treatment site provide only single-circular cone-beam projections if all projections are to be conveniently taken in a single run. The effect of incomplete and truncated projection data needs therefore to be evaluated for each specific application.

3.2 Image reconstruction

This section on image reconstruction algorithms is dedicated to transform methods. Iterative techniques are considered in the next section in the context of image restoration from partial projection data and the use of prior information.

In *transform methods*, the object f to be reconstructed and its projections g are primarily considered as functions of continuous variables. Data acquisition for a particular projection geometry is modelled by an integral transform such that $g = \mathcal{T} f$. An image reconstruction algorithm can then be derived by (at least approximate) inversion of the operator $\mathcal{T}$.

Transform methods depend strongly on the particular data acquisition geometry. This property is therefore used in the following to classify the algorithms into parallel-beam, fan-beam and cone-beam algorithms. Whereas the mathematics of two-dimensional computed tomography has been intensively studied previously [41, 77], there is still much current research on cone-beam techniques [16].

3.2.1 Parallel-beam algorithms

The parallel-beam acquisition scheme in a plane is described by the two-dimensional Radon transform, which maps a function onto a set of its integrals over all hyperplanes (see definition A.5). Various inversion formulae for the Radon transform have been derived, which lead to different image reconstruction algorithms.

The *Fourier method*, first proposed by Bracewell [8], comprises an immediate application theorem A.5, which is known as the Fourier-slice or projection theorem. The difficulty with the Fourier method lies in its practical implementation. For discrete projection data, the object is sampled on a polar grid in frequency space. Resampling onto a Cartesian grid is necessary, before an image can be calculated using an inverse, fast Fourier transform (FFT) algorithm. Stark et al. [116] presented a careful analysis of the interpolation kernels required for this resampling.

Smith et al. [113] introduced the *filtered-layergram* method, which is based on theorem A.6. The method starts with a backprojection of all parallel projections into the two-dimensional plane, which yields a very blurred image, the so-called layergram. The desired image is then obtained by a two-dimensional deconvolution. The major implementation problem is caused by the backprojection step, which yields an image of infinite spatial extent. Although the layergram vanishes in practice, the backprojection and deconvolution have to be performed on grids several times larger than the object, in order to achieve sufficiently accurate results.

The idea of image reconstruction by *filtered backprojection* was first presented by Bracewell and Riddle [9]. In this type of algorithms, the projections are filtered independently in one dimension and then backprojected into the image plane, as shown in theorem A.7. This is the most common image reconstruction method. Each projection can be processed (filtered and backprojected) independently of others, which allows for online reconstruction during data acquisition. The backprojection can also be performed in a region of interest in order to save computation time.

3.2.2 Fan-beam algorithms

Fan-beam projection geometry is modelled by the two-dimensional divergent-beam transform (see definition A.7). Reconstruction algorithms for fan-beam projections can be derived from parallel-beam formulae by using a corresponding coordinate transform.

In *parallel rebinning* algorithms as proposed by Dreike and Boyd [20], a set of equivalent parallel-beam projections is obtained from the recorded fan-beam data. Except for specific acquisition geometries, this so-called rebinning step requires two successive (linear) interpolations for each line integral in the parallel-beam data set. Spatial resolution is therefore potentially slightly decreased. Once the parallel projections have been estimated, one of the reconstruction methods described in the previous subsection is applied. Using the direct Fourier method, the truncation of the theoretically infinite interpolation kernels in practical implementations results in ring artefacts in the images. Peng and Stark [87], however, proposed a method to correct for this inevitable truncation.

The first development of a *filtered backprojection* algorithm that is appropriate for direct use on fan-beam data was carried out by Pavkovich [86]. Starting with parallel-beam filtered backprojection, the transform from parallel to fan coordinates results in an additional weighting of the projections by the fan angle cosine, a change of the filter kernel (for curved detectors) and an additional distance weighting factor within the backprojection.

The first mathematical treatment of fan-beam *short-scan* data sets was presented by Naparstek [75]. In practice, there are three different approaches to account for redundant line integrals in short-scan sets.

Parallel rebinning algorithms work as described above. For a short-scan data set, the corresponding parallel-beam projections lie in a view angle range of π. Redundant information in the input data is usually discarded in the rebinning step. The noise reduction is therefore not optimal.

In *complementary rebinning* techniques, the missing part of the short-scan projection data set is filled out using the measured rays. Standard fan-beam filtered backprojection is then applied. Complementary rebinning can be performed without interpolation on discrete data if the view angle pitch is twice the fan angle pitch. In practice, CT scanners take substantially fewer projections per turn than suggested by this condition.

In *sinogram windowing* techniques, a weighting function is applied to the short-scan data set before filtering and backprojection. For line integrals measured once the weight has to be unity, whereas for integrals measured twice the sum of the corresponding weights must equal one. The weighting function is furthermore required to be approximately band-limited in order to avoid streak-shaped aliasing artefacts in the reconstruction of discrete data. Parker [85] proposed such a smooth weighting function for minimal complete fan-beam sets, which was recently extended to data sets exhibiting an over-scan [111, 132].

The full-scan and short-scan reconstruction algorithms mentioned above assume that all fan-beam projections are measured in a plane. They are not immediately applicable to helical scans as introduced by Kalender [53]. In this case, a preceeding interpolation onto planar full-scan or short-scan sets is necessary. Numerous different interpolation schemes have been suggested; see, for example, [50, 91] and references therein.

3.2.3 Cone-beam algorithms

The choice of an appropriate cone-beam reconstruction algorithm depends on the particular scanning geometry and on the axial opening angle of the beam. Approximate algorithms are often applied even to projection data that satisfy the completeness condition, since exact cone-beam reconstruction is mathematically and computationally complex.

For *small cone angles* such as in diagnostic multi-row CT scanners, the combination of different axial interpolation schemes with two-dimensional filtered backprojection algorithms is frequently used. Hu [44] provided a detailed analysis of various interpolation algorithms and preferable pitch values. Noo et al. [82] proposed a single-slice rebinning method for helical cone-beam projections. In this approximation, a short-scan fan-beam sinogram is obtained from the cone-beam projections for each transaxial slice. The slices are then reconstructed using a standard filtered backprojection algorithm involving Parker weights [85].

For *intermediate cone angles*, approximate algorithms employing true three-dimensional backprojection are preferable to the above methods. Feldkamp, Davis and Kress [24] proposed a straight-forward extension of fan-beam filtered backprojection to a single-circular cone-beam geometry, which has been widely used since then.

Grass et al. [33] proposed a parallel rebinning technique, which comprises the application of the corresponding two-dimensional method to each row of a planar detector. Compared to the original Feldkamp algorithm [24], the intensity drop in axial direction due to the missing data is significantly decreased. An extension of this method considers the short-scan sufficiency condition for each voxel independently by means of an adaptive weighting scheme. Consequently, the reconstruction volume is considerably enlarged, and the noise properties are optimized.

The Feldkamp method [24] was also extended to elliptical, helical and circle-plus-line scan paths. Using a direct adaption as in [128, 137, 141], the projection data are not efficiently utilized. As a consequence, the dose delivered is not fully exploited, and the pitch of the helix is limited. Recent advances overcoming these problems are based on filtered backprojection of short-scan segments [56] or parallel rebinning techniques [123].

For *large cone angles*, complete projection data and exact reconstruction algorithms are required to avoid severe artefacts in the images. Tuy [124], Smith [112] and Grangeat [32] derived formulae that relate the cone-beam transform to the (Hilbert transform of the) first derivative of the three-dimensional Radon transform. These relations have been used to develop mathematically exact cone-beam reconstruction algorithms.

In *Radon rebinning* methods, one of the above intermediate functions is explicitly calculated from the cone-beam projections. The image is then reconstructed from the intermediate result by applying a Radon inversion formula. The first Radon rebinning implementations for several source trajectories were presented by Kudo and Saito [57], Weng et al. [131] and Zeng et al. [140]. Noo et al. [80] proposed a rebinning method for arbitrary data sets and defined a measure of what degree a set of cone-beam projections satisfies the completeness condition. All of these algorithms assume non-truncated projections. Kudo et al. [55] modified Grangeat's formula [32] in order to consider truncated helical data. They did not investigate partial scans of the object. Tam [122] proposed a solution of the long-object problem by adding two extra circles at both ends of the helix. A Radon rebinning algorithm that is capable to handle regions of interests in long objects without this additional requirement was recently presented by Schaller et al. [104].

The basic cone-beam inversion formulae were also used to derive *filtered backprojection* methods that do not rely on the storage of intermediate Radon data. They are therefore capable of processing the projections independently of each other. The algorithms by Defrise and Clack [17] as well as Kudo and Saito [58, 59] are appropriate for helical, double-circular and circle-and-line orbits, but assume non-truncated projections and short objects. Kudo et al. [55] suggested a modified algorithm that is capable of handling truncated projections. Tam et al. [120] presented a technique for region-of-interest reconstructions of long objects by adding two circles at the ends of a helix scan segment, as mentioned above. Defrise et al. [19] proposed an approximate, but very accurate solution to the combination of both of these problems. Their algorithm does not take the form of pure filtered backprojection, but is nevertheless computationally quite efficient.

3.2.4 Conclusion

In this thesis, fan-beam algorithms and cone-beam algorithms for intermediate cone angles are of particular interest due to the technical limitation of data acquisition schemes explained above. Exact cone-beam algorithms do not offer any advantage when applied to incomplete data. The algorithms proposed by Defrise and Clack [17] and Kudo and Saito [58, 59], for example, reduce to the approximate Feldkamp algorithm [24] when applied to single-circular cone-beam projections.

3.3 Image restoration

The object $f(\boldsymbol{r})$ can be reconstructed by means of analytical methods considered in the previous section if the Radon transform $\mathcal{R} f(\boldsymbol{r})$ is completely determined and sufficiently sampled by the projection data. In practical situations, however, the projection data can be incomplete for a number of reasons.

In subsection 2.2.1, three specific types of incomplete projection data are introduced. From the mathematical point of view, the *exterior problem* and the *limited-angle problem* are uniquely solvable, but severely ill-posed. The *interior problem*, in contrast, is not uniquely solvable. These general statements have been proved rigorously [77] using the assumptions listed in appendix A.

There is a huge literature on limited-data problems, both in two and three dimensions. However, care should be taken when reviewing the powerful mathematics that has been brought to tackle them [7]. Image restoration is often extremely sensitive to noise, but many methods have only been applied to noise-free simulated projection data. Even if noise is properly included, computer simulations may not resemble reality very well. Restricting the object to a narrow range of attenuation coefficients, for example, may not be applicable to clinical data.

An annotated bibliography of earlier work on image restoration from incomplete projection data comprising more than 250 references was presented by Rangayyan et al. [94]. The following subsections attempt to classify the huge number of techniques and algorithms roughly. Of course, only some selected publications are mentioned in this review.

3.3.1 Analytical continuation

In this subsection, a class of restoration techniques dedicated to the limited-angle problem is introduced. The methods reviewed in the following subsections are more general and therefore, in principle, applicable to all kinds of incomplete projection data.

The most intuitive understanding of the limited-angle problem is provided by theorem A.5, which relates the Radon transform to the Fourier transform of an object. From this theorem it is obvious that two V-shaped regions are missing in frequency space if parallel-beam projections are collected only over a limited angular range. This is sketched in figure 3.2.

This implies that no amount of linear filtering can ever restore the Fourier components lost in the data acquisition process. *Prior information* about the object, i.e., information that is available before making the measurements, is therefore the only hope for filling in the missing parts.

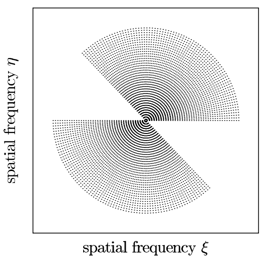

Figure 3.2: Schematic representation of the limited-angle problem. The dots indicate the area in frequency space that is covered by a parallel-beam scan over $\frac{3}{4}\pi$. Spatial frequencies are given in arbitrary units.

In real computed tomography applications, the object function $f(\boldsymbol{r})$ is spatially limited, i.e., for some $r_{\max}$, $f(\boldsymbol{r}) = 0$ if $\|\boldsymbol{r}\| > r_{\max}$. Its Fourier transform $F(\boldsymbol{\rho}) = \mathcal{F} f(\boldsymbol{r})$ is therefore an analytical (entire) function. An analytical function can be continued throughout the whole space from any finite, continuous segment [10]. Combining these two theorems yields the implication that finite support of the object is sufficient for the uniqueness of the limited-angle problem. The part of the Fourier transform of the object that is missing due to the restricted range of view angles can therefore, in principle, be always filled.

Direct continuation techniques based on series expansion of the known part of the function to be extrapolated suffer from intense noise amplification [27]. Gerchberg [27] and Papoulis [84] proposed therefore an iterative, less noise-sensitive continuation procedure that comprises successive Fourier and inverse Fourier transforms. In each iteration step, the object function is zeroed outside its a priori known spatial extent, and the spectrum is corrected for the measured part.[1]

Louis [66, 77] proposed an analytical continuation technique for parallel-beam data that operates in projection space. After estimating the missing projections, a standard filtered backprojection is applied. The continuation algorithm requires the solution of a highly ill-conditioned linear system of equations in order to obtain series expansion coefficients for the missing data. This badly conditioned system indicates once more that the limited-angle problem is severely ill-posed. The algorithm, however, is not capable of incorporating further prior information that might regularize the solution.

3.3.2 Projections onto convex sets

The method of *projections onto convex sets* (POCS) is a powerful tool in image restoration. The general idea of POCS is as follows.[2] Let $\mathcal{C}$ be an operator that enforces all constraints on the function f that is sought.[3] A consistent estimate $\tilde{f}$ remains unchanged when the constraint operator acts

[1] This method can be also employed to extrapolate band-limited functions (analytical functions exhibiting a finite frequency spectrum), which follows directly from the uniqueness of the Fourier transform.

[2] A thorough introduction to the method of projections onto convex sets can be obtained from Schafer et al. [103] or Youla and Webb [139]. For the reader's convenience, the theory of POCS is summarized briefly in section A.4.

[3] The term ‘projection’ in POCS refers to the application of a constraint operator $\mathcal{C}$. This term is not used in this thesis in order to avoid any potential confusion with the X-ray projections g of an object f.

on it, $\tilde{f} = \mathcal{C}\,\tilde{f}$. This means $\tilde{f}$ is a fixed point of the operator $\mathcal{C}$. The desired estimate can therefore be obtained by one of the standard iterative methods such as successive substitutions, steepest descent or conjugate gradients.

The first application of the theory of POCS to image restoration was reported by Youla [138]. This method allows for the incorporation of all kinds of prior knowledge as long as this knowledge can be associated with convex sets in the sense of definition A.10. In POCS, there is no difference between enforcing consistency of an object f with its measured X-ray projections g and other constraints as, for example, finite spatial extent or non-negativity of f. The feasibility of various constraints in image restoration from incomplete projection data was investigated by Sezan and Stark [107], Lent and Tuy [61], Oskoi-Fard and Stark [83], Stark et al. [115] and others.

The method of projections onto convex sets reduces to the well-known *additive algebraic reconstruction technique*[4] (AART) if consistency of a discretized object with the measured line integrals is employed as the only constraint. The iterative scheme of AART was originally proposed by Kaczmarz [48] for solving consistent linear systems of equations.

Using finite spatial extent of the object and a measured part of its Fourier transform as constraints yields the *Gerchberg-Papoulis algorithm* [27, 84] mentioned above. For complete data, one iteration step is equivalent to the *direct Fourier method* (DFM). Image restoration from limited-angle data using POCS was reported for parallel-beam [88, 102, 108, 121] and fan-beam [89] projections. In the latter case, parallel rebinning was employed in order to apply the DFM to fan-beam data.

Due to the projection theorem, the consistency of the object with the measured line integrals can be enforced in projection rather than in Fourier space. Such iterative schemes comprising successive filtered backprojection and reprojection were proposed by Nassi et al. [76] and Medoff et al. [69]. This approach is even more general. It can not only be applied to the limited-angle problem, which corresponds to a particular region missing in frequency space, but to any kind of incomplete projection data. Kim et al. [54] showed that the iterative backprojection and reprojection procedure can be completely realized in Radon space. Potential cumulative interpolation errors arising from the discrete implementation of backprojection and reprojection are therefore avoided.

[4] The name ‘algebraic reconstruction technique’ (ART) is a historical accident; ART is no more ‘algebraic’ than in other iterative procedures. However, this name is widely used for the type of algorithms in which all line integrals are accessed successively.

3.3.3 Optimization methods

Another common approach in image restoration is to define an *objective function* $O(f)$ that enforces consistency of the image f with its projection data. $O(f)$ is, depending on its particular definition, maximized or minimized in order to compute the desired estimate $\tilde{f}$. Prior information can be considered directly by means of *penalty terms* in $O(f)$ or indirectly by the introduction of *constraint operators* into the iterative optimization. The definition of an additional criterion is required if the objective function does guarantee a unique solution. Typical secondary criteria such as *minimum norm*, *minimum variance* and *maximum entropy* of f are discussed by Herman [41].

The optimization can be handled conveniently when both the objective function and the constraints are convex.[5] One common approach is to minimize the mean difference between measured and reprojected line integrals. Without further constraints, this approach yields the *simultaneous iterative reconstruction technique* (SIRT) [28], which is also known as *Richardson's method* in numerical analysis. The theory of convex optimization allows the incorporation of any convex constraints like in POCS.

A more sophisticated objective function incorporating statistical information is, in principle, very attractive. The image f and the projection data g are then considered as samples of corresponding probability distributions.

In the *Bayesian approach*, a particular estimate $\tilde{f}$ is sought that maximizes the a posteriori conditional probability $P(f \mid g)$ for the image f given the measured projection data g. This probability is computed using Bayes' law in terms of the conditional probability $P(g \mid f)$ and the a priori probability distributions $P(f)$ and $P(g)$. Hanson and Wecksung [40] suggested this framework for the limited-angle problem. The assumptions about the a priori probability distribution of the images employed in their simulation studies, however, are quite restrictive. In real applications, it is almost impossible to obtain reliable statistical information on all objects to be imaged.

To avoid these problems, the conditional probality $P(g \mid f)$ of observing the measured projection data g given the image f (the likelihood of f) can be maximized separately instead. This approach of *maximum likelihood expectetation maximization* (MLEM) reduces to the *multiplicative algebraic reconstruction technique* (MART) if the Poisson statistics of the projection data are modelled. In MART, non-negativity of the estimate $\tilde{f}$ is guaran-

[5] The mathematical theory of *convex optimization* is not explained in detail here; see, for example, [10] for further information.

teed. Vollmar et al. [127] demonstrated how other prior information can be included in an MLEM procedure.

3.3.4 Alternative approaches

Yagle [136] presented a closed-form solution of the discrete limited-angle problem. The method for extrapolating the projection data is computationally efficient and avoids the solution of a large ill-conditioned system of equations. A successful application to real data, however, seems questionable due to quite restricitve assumptions. The amplitude of additive noise is assumed to be negligible such that it can be completely eliminated by rescaling the line integrals and rounding them to integer numbers. The view angles of the parallel-beam projections have to be chosen in such way that frequency space is sampled along concentric squares, i.e., the projections are not equiangular.

Brunetti and Golosio [12] proposed a morphological technique for tackling the limited-angle problem. They applied a novel curve matching algorithm, which is based on recent advances in computer graphics, for approximating the missing part of the sinogram. The preliminary results look quite promising, although no specialized prior knowledge on the objects to be restored was utilized. This remains a challenge for future research in order to further improve the performance of the method.

Various other methods have been employed for image restoration from incomplete projection data. Geometric deconvolution techniques [31] as well as backpropagation algorithms utilized in neural networks [1] were proposed, to mention only two of the numerous examples. A detailed discussion of all of these attempts, however, is beyond the scope of this thesis.

3.3.5 Conclusion

Various image restoration methods have been proposed for computed tomography based on incomplete projection data such as demonstrated above. Several authors considered limited-angle CT to reduce the problem of inconsistent projection data due to the heart beat; see for example the annotated bibliography in [94]. Very little, however, has been published on the application of limited-angle algorithms to real data [7]. Clinical CT heart imaging still uses short-scan filtered backprojection or combination of data segments from various heart cycles [47, 50].

3.4 Geometric calibration

The importance of an accurate geometric calibration in CT imaging is emphasized in subsection 2.2.3. There it is demonstrated that even small flex effects can cause serious artefacts in the images if they are not adequately corrected for.

3.4.1 Classification of calibration methods

Several methods for geometric calibration of CT image acquisition devices have been proposed in past years. These techniques can be roughly classified in the following manner [96].

1. The principle behind the *alignment method* is to place the source and detector assembly in a known position and orientation. This method is used in diagnostic X-ray CT scanners and in many industrial CT applications.

2. In *global calibration methods*, an ideal scanning geometry with unknown parameters is assumed. This situation occurs, for instance, in microtomography in which the position of the centre of rotation often cannot be measured with the desired accuracy [3]. Simple phantoms like thin rods are scanned to estimate the geometric parameters using the coherence of the data in all of the projections.

3. In *local calibration methods*, the projection geometry is estimated for each view separately. The main advantage of these techniques is that they do not make any assumptions about the scan path and do not require fixed source-to-isocentre and source-to-detector distances [96]. The estimation is based on a calibration scan of a dedicated phantom which comprises a sufficiently large number of fiducial markers.

The alignment method is not well-suited for a calibration of systems that are under consideration here. A sufficiently accurate alignment of the components of a linear accelerator or an angiography device would require major changes to the hardware, since they were not originally intended for CT imaging. In most cases, not even the global method, but only the local approach is flexible enough to handle the calibration of such devices. However, the global as well as the local estimation techniques which have been published recently are reviewed in the following two subsections, since they involve similar mathematical methods.

3.4.2 Global calibration methods

Theoretically, the geometry of a CT scanner could be estimated in an iterative procedure. Each iteration step would involve image reconstruction and variation of the unknown parameters. The algorithm would stop if the desired image quality was achieved, i.e., the artefacts caused by the geometric uncertainties had disappeared. Although mentioned in [3], this method has probably never been practically used due to several disadvantages. Since a full image reconstruction is required in each step, the estimation would be quite time-consuming. The number of unknown scanner parameters had to be fairly small to be able to handle the optimization practically. Furthermore, the iterative process would probably involve the user because an automatic analysis of the artefacts might be impossible to implement.

Azevedo et. al. [3] proposed an elegant algorithm which enables the calculation of the centre of rotation (COR) from an arbitrary, two-dimensional, parallel projection data set. The method is based on the observation that the centre of gravity of an object always lies on a line passing through the projection centre of gravity and having a slope angle equal to the projection view angle. Therefore, the COR can be calculated directly from the sinogram provided that there is sufficient contrast in the projections, that all projections have the same COR, that the object is fully covered in all projections, and that non-linear effects like beam hardening, scatter and source intensity fluctuations are negligible. The derivation of a similar method for fan-beam sinograms is not possible for arbitrary objects.

To overcome this limitation, the imaging of a point object (such as a thin wire or pin phantom) was suggested by several authors. The location of the point object is measured in all projections. Analytical expressions are derived that relate the unknown scanner parameters (such as source-to-isocentre distance, position and orientation of the detector) and the unknown position of the calibration object to the respective location in the projections. The equations are solved in a least squares sense (e.g., using the Levenberg-Marquardt algorithm [92]), in order to obtain the scanner parameters that are sought. The formulae describing the standard filtered backprojection are adapted to incorporate these parameters. Algorithms of this type were proposed by Gullberg et al. [37, 39] for fan-beam geometries and by Gullberg et al. [38], Li et al. [62, 63, 64], Rizo et al. [96] and Wang et al. [129] for cone-beam geometries. An accurate estimation can be, however, difficult to obtain due to highly non-linear objective functions with multiple local minima and strong correlations between the desired parameters.

Rizo et al. [96] split the optimization into two steps. First the intrinsic parameters describing the detector are estimated using a grid phantom which is placed in several well-defined positions. The extrinsic parameters describing the projective geometry are then estimated in a non-linear least squares fit. Due to the reduced number of parameters in the second step, the minimization is more stable than in the previously mentioned techniques. Nevertheless, the remaining uncertainty of the source-to-detector distance is about 5 %. The correct scaling of the image is, therefore, determined by imaging and reconstructing another test phantom.

Noo et al. [81] proposed an analytical method for scanner calibration in cone-beam computed tomography, which completely avoids the non-linear optimization. It is based on a calibration scan involving two small point objects. The method requires the detector to be aligned parallel to the rotation axis of the scanner.

3.4.3 Local calibration methods

The estimation of geometric parameters using local methods is mathematically much more complex than using global techniques described before. For arbitrary cone-beam projections, there are 11 degrees of freedom for each view that need to be considered. Sometimes, the problem is reduced to 9 degrees of freedom, assuming that the detector axes are perfectly orthogonal and do not exhibit significant differences in scale.

An iterative optimization of these parameters involving repeated image reconstruction steps would not be feasible at all. Therefore, all local techniques are based on a calibration phantom which contains a sufficiently large number of appropriate fiducial markers. The relative position of these markers has to be accurately known; the corresponding uncertainties should be at least one magnitude smaller than those of measuring their position in projection images of the phantom. Using the known geometry of the phantom and its projections, the projection geometry of a CT scan can be estimated for each view independently.

On one hand, the projection geometry for each view can be estimated in terms of geometric parameters such as source-to-isocentre distance, source-to-detector distance, position and orientation of the detector. These parameters are obtained using a non-linear minimization procedure. The objective function usually calculates the mean square deviation between the marker positions measured in the calibration images and the corresponding values reprojected from the known three-dimensional coordinates in object space. Roguée et al. [99] proposed the use of such a parametric method for the calibration of X-ray imaging chains. Their approach seems to be very attractive because parameters that can be clearly interpreted in geometric sense are obtained. The concerns about highly non-linear objective functions mentioned in the previous subsection do, however, also hold for local techniques.

Wiesent et al. [134] suggested a non-parametric method to avoid the problems that can occur in the non-linear minimization. In this approach, a projection matrix is determined for each view that maps three-dimensional object coordinates onto two-dimensional detector coordinates. The matrices are calculated analytically based on the information that is provided by scanning a calibration phantom.

The coefficients of a projection matrix as provided by the non-parametric calibration method cannot be interpreted geometrically, which is sometimes referred as a major drawback of this approach [99]. Melen [70] proposed an analytical technique for the decomposition of projection matrices, but did not investigate its accuracy for estimated projection matrices.

3.4.4 Conclusion

In many current implementations of calibration methods, only few degrees of freedom are considered. Frequently, only a centre-of-rotation correction is performed for each view [14, 22, 72, 73, 101]. The accuracy of parametric and non-parametric methods considering arbitrary (linear) cone-beam projections has not yet been investigated comprehensively. Their applicability to geometric calibration of X-ray imaging systems is not judged consistently in the literature; compare, for example, the arguments given in [99] and [134].

Chapter 4

Material and methods

In this chapter, the hardware and the methods utilized for X-ray computed tomography (CT) are explained in detail. The descriptions do require some knowledge on the underlying mathematical theory. An introduction to the basics is therefore given in appendix A. This chapter is organized as follows.

Section 4.1 introduces a *geometric model* for CT data acquisition and the concept of *projection matrices*, each of them containing the geometric information for a particular view defined by position and orientation of X-ray source and detector.

Section 4.2 describes the *hardware* of a commercial fan-beam scanner and two experimental cone-beam systems that were utilized for projection data acquisition. Section 4.3 provides an overview of the *preprocessing methods* for estimating the line integrals through the spatial X-ray attenuation distribution from the signal captured by the detector.

Section 4.4 deals with the *geometric calibration* of CT scanners that exhibit significant deviations from an ideal set-up. The calibration procedure employed here yields an estimate of the projection matrix for each view.

Sections 4.5 and 4.6 describe the methods used for image reconstruction and restoration, respectively. *Reconstruction* denotes the computation of tomographic images from a complete set of projections, whereas *restoration* refers to the recovery of images from partial projection data and prior knowledge of an object. The algorithms are defined for continuous functions of continuous variables in order to enable a convenient notation. Appendix C, however, provides information on the implementation of the algorithms on a digital computer processing discrete projection and image data.

4.1 Divergent-beam geometry

Two-dimensional fan-beam as well as three-dimensional cone-beam computed tomography are considered in this thesis. The systems used for projection data acquisition operate in third-generation scanning mode, i.e., X-ray source and detector rotate together around the object. In this section, a mathematical notation to describe the geometry of such third-generation scanners is introduced, which is utilized throughout the whole thesis. All explanations are provided for three-dimensional cone-beam geometry, of which two-dimensional fan-beam geometry is a special case restricted to the plane of source rotation.

4.1.1 Geometric conventions

The mathematical notation introduced in this subsection is schematically shown in figure 4.1. It refers to ideal, third-generation scanners, i.e., geometric flex effects such as mentioned in subsection 2.2.3 are neglected for the moment.

X-ray source and detector move together in a plane parallel to $z = 0$ with respect to a Cartesian coordinate system fixed in three-dimensional space. The centre of rotation (isocentre) coincides normally with the origin of this coordinate system. R is the distance from the focus $\boldsymbol{r}_{\text{foc}} = (x_{\text{foc}}, y_{\text{foc}}, z_{\text{foc}})^{\mathrm{T}}$ to the isocentre $\boldsymbol{r}_{\text{iso}} = (x_{\text{iso}}, y_{\text{iso}}, z_{\text{iso}})^{\mathrm{T}}$, and D is the focus-to-detector distance. The view angle α of a particular projection is measured from the positive y axis to the central ray.

By convention, the rows and columns of the detector are assumed to be parallel to the u and v axis of the detector coordinate system, respectively. Due to the finite size of the detector, the coordinates u and v are restricted to the range $[-u_{\max}, u_{\max}]$ and $[-v_{\max}, v_{\max}]$, respectively. The central ray through the isocentre $\boldsymbol{r}_{\text{iso}}$ intersects the detector at the view reference point $\boldsymbol{s}_{\text{foc}} = (u_{\text{foc}}, v_{\text{foc}})^{\mathrm{T}}$. In an ideal divergent-beam geometry, the view reference point coincides normally with the origin of the detector coordinate system as depicted in figure 4.1.

The angles β and γ measured between the central ray and a particular ray of interest are defined as

$$\beta = \arctan \frac{u - u_{\text{foc}}}{D} \quad \text{and} \quad \gamma = \arctan \frac{v - v_{\text{foc}}}{D} \tag{4.1}$$

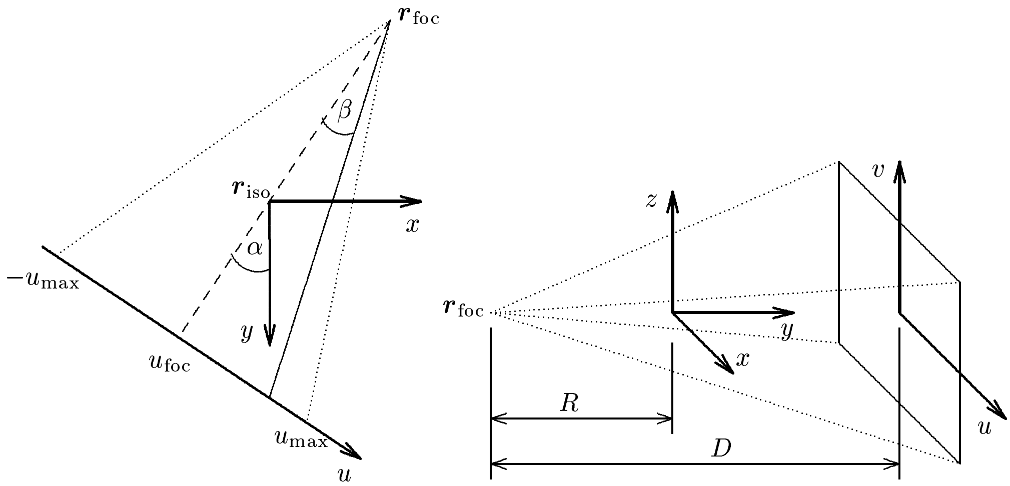

Figure 4.1: Mathematical notation for describing single-circular divergent-beam geometries. The figure shows a two-dimensional schema of a fan-beam geometry within the plane of source rotation (left panel) and a three-dimensional representation of a cone-beam geometry (right panel).

with respect to the coordinates u and v, respectively. The in-plane angle β is utilized for detectors that are curved along the u axis. Although detectors curved in v direction do not exist in practice, the definition of γ is useful to assess artefacts that worsen with increasing distance from the central plane independently from particular values for R and D. Even in three dimensions, β and γ are often referred to as fan angle and cone angle, respectively, in order to simplify geometric descriptions. The in-plane and axial aperture of the X-ray beam are denoted as $2\beta_{\max}$ and $2\gamma_{\max}$.

The size of the detector determines the field of view (FOV). Here, the FOV is defined as set of those points in three-dimensional space that are projected on the valid range of detector coordinates in all views. For a single-circular source trajectory as shown in the left panel of figure 3.1 on page 18, the radius of the field of view, R_{FOV}, is given by

$$R_{\mathrm{FOV}}(v) = \min\left(\frac{R\,u_{\max}}{\sqrt{D^2 + u_{\max}^2}}, R\left(1 - \frac{v}{v_{\max}}\right)\right) \tag{4.2}$$

in the axial plane $z = v$ or, using fan angle and cone angle, equivalently by

$$R_{\mathrm{FOV}}(\gamma) = \min\left(R\,\sin\beta_{\max}, R\left(1 - \frac{\tan\gamma}{\tan\gamma_{\max}}\right)\right) \tag{4.3}$$

in the axial plane $z = R\,\tan\gamma$.

4.1.2 Conic projections

Using homogeneous coordinates, the mapping from three-dimensional object space into two-dimensional detector space is written as

$$\lambda\ (u, v, 1)^{\mathrm{T}} = \boldsymbol{P}\ (x, y, z, 1)^{\mathrm{T}}\ , \tag{4.4}$$

where $\boldsymbol{P}$ is a 3×4 projection matrix for a particular view [134]. λ denotes a non-zero, overall scaling factor, which can be eliminated by taking the ratios

$$u = \frac{p_{11}\,x + p_{12}\,y + p_{13}\,z + p_{14}}{p_{31}\,x + p_{32}\,y + p_{33}\,z + p_{34}}\,, \tag{4.5}$$

$$v = \frac{p_{21}\,x + p_{22}\,y + p_{23}\,z + p_{24}}{p_{31}\,x + p_{32}\,y + p_{33}\,z + p_{34}}\,. \tag{4.6}$$

Due to the scaling factor λ, there are 11 degrees of freedom in this mathematical model of conic projections, which are interpreted in geometric sense in the subsequent subsection. The use of this model implies basically two assumptions.

- The finite size of the focus within the X-ray source is negligibly small and is well approximated by a single point in three-dimensional space.
- Projection data are captured on an ideally planar surface. The detector does not introduce any non-linear distortion.

The model is primarily intended for flat-panel detectors. For curved detectors, the planar coordinates need to be transformed using equation (4.1).

4.1.3 Composition of projection matrices

Based on a formula that was introduced previously [70], the projection matrix $\boldsymbol{P}$ is composed by

$$\boldsymbol{P} = \lambda\ \boldsymbol{V}\,\boldsymbol{A}^{-1}\,\boldsymbol{D}\,\boldsymbol{S}\,\boldsymbol{F}\,. \tag{4.7}$$

The above equation can be interpreted as successive transformations from the object into the detector coordinate system, where each step has a clear geometric meaning. Starting from the right,

$$\boldsymbol{F} = \begin{pmatrix} 1 & 0 & 0 & -x_{\mathrm{foc}} \\ 0 & 1 & 0 & -y_{\mathrm{foc}} \\ 0 & 0 & 1 & -z_{\mathrm{foc}} \end{pmatrix} \tag{4.8}$$

is a translation from the origin of the object coordinate system to the source position. In an ideal cone-beam geometry, the in-plane position of the focus is given by $x_{\text{foc}} = x_{\text{iso}} + R \sin\alpha$, $y_{\text{foc}} = y_{\text{iso}} - R \cos\alpha$, and $z_{\text{foc}} = z_{\text{iso}}$ determines the axial position of the plane the focus rotates in.

$$\boldsymbol{S} = \begin{pmatrix} \cos\psi & \sin\psi & 0 \\ -\sin\psi & \cos\psi & 0 \\ 0 & 0 & 1 \end{pmatrix} \begin{pmatrix} 1 & 0 & 0 \\ 0 & \cos\theta & \sin\theta \\ 0 & -\sin\theta & \cos\theta \end{pmatrix} \begin{pmatrix} \cos\phi & \sin\phi & 0 \\ -\sin\phi & \cos\phi & 0 \\ 0 & 0 & 1 \end{pmatrix} \tag{4.9}$$

is a rotation matrix comprised by the Euler angles ϕ, θ, ψ. It ensures that, in the rotated system, the central projection ray is perpendicular to the detector. In an ideal cone-beam geometry, the angles are $\phi = \alpha$, $\theta = \frac{1}{2}\pi$ and $\psi = 0$. In homogeneous coordinates, the projection from three-dimensional object space into two-dimensional detector space is given by

$$\boldsymbol{D} = \begin{pmatrix} -D & 0 & 0 \\ 0 & -D & 0 \\ 0 & 0 & 1 \end{pmatrix}, \tag{4.10}$$

where D is the focus-to-detector distance with $D > 0$. Furthermore, the definition of

$$\boldsymbol{A} = \begin{pmatrix} 1+a_1 & a_2 & 0 \\ a_2 & 1-a_1 & 0 \\ 0 & 0 & 1 \end{pmatrix}, \quad \boldsymbol{A}^{-1} = \begin{pmatrix} \dfrac{1-a_1}{1-(a_1^2+a_2^2)} & \dfrac{-a_2}{1-(a_1^2+a_2^2)} & 0 \\ \dfrac{-a_2}{1-(a_1^2+a_2^2)} & \dfrac{1+a_1}{1-(a_1^2+a_2^2)} & 0 \\ 0 & 0 & 1 \end{pmatrix} \tag{4.11}$$

introduces two coefficients a_1, a_2 in order to account for a difference in scale and a lack of orthogonality between the detector axes. These coefficients are usually close to zero. The matrix $\boldsymbol{A}$ is invertible if the constraint $a_1^2 + a_2^2 < 1$ is satisfied. This inequality implies $|a_1| < 1$ and $|a_2| < 1$, which is reasonable, since $|a_1| > 1$ would change the direction of one of the detector axes, and $|a_2| > 1$ would swap the axes. The matrices

$$\boldsymbol{V} = \begin{pmatrix} 1 & 0 & u_{\text{foc}} \\ 0 & 1 & v_{\text{foc}} \\ 0 & 0 & 1 \end{pmatrix}, \quad \boldsymbol{V}^{-1} = \begin{pmatrix} 1 & 0 & -u_{\text{foc}} \\ 0 & 1 & -v_{\text{foc}} \\ 0 & 0 & 1 \end{pmatrix} \tag{4.12}$$

represent a shift within the detector coordinate system to consider a potential offset between its origin and the view reference point $(u_{\text{foc}}, v_{\text{foc}})^{\mathrm{T}}$.

4.1.4 Decomposition of projection matrices

The algorithm for analytical decomposition of projection matrices described in this subsection is based on a method proposed previously [70]. It refers to the set of geometric parameters introduced above.

The left 3×3 sub-matrix of $\boldsymbol{P}$ is assumed to have full rank three in order to guarantee a successful execution of the following decomposition steps.

The coordinates x_{foc}, y_{foc}, z_{foc} of the focus are obtained by solving the linear system of equations

$$\begin{pmatrix} p_{11} & p_{12} & p_{13} \\ p_{21} & p_{22} & p_{23} \\ p_{31} & p_{32} & p_{33} \end{pmatrix} \begin{pmatrix} x_{\text{foc}} \\ y_{\text{foc}} \\ z_{\text{foc}} \end{pmatrix} = \begin{pmatrix} -p_{14} \\ -p_{24} \\ -p_{34} \end{pmatrix} . \tag{4.13}$$

There exists a unique solution of (4.13) because the left sub-matrix of $\boldsymbol{P}$ has full rank according to the above assumption.

The magnitude of the overall scaling factor λ is computed by

$$|\lambda| = \sqrt{p_{31}^2 + p_{32}^2 + p_{33}^2} \,, \tag{4.14}$$

where $|\lambda| \neq 0$ because of the above assumption. The left sub-matrix of $\boldsymbol{P}$ is then normalized, which yields

$$\boldsymbol{P'} = \frac{1}{|\lambda|} \begin{pmatrix} p_{11} & p_{12} & p_{13} \\ p_{21} & p_{22} & p_{23} \\ p_{31} & p_{32} & p_{33} \end{pmatrix} . \tag{4.15}$$

The RQ factorization of $\boldsymbol{P'}$ is computed using Schmidt's orthogonalization method [10] or, preferably, using (numerically more stable) successive Householder transformations [92],

$$\boldsymbol{P'} = \boldsymbol{R}\boldsymbol{Q} = \begin{pmatrix} r_{11} & r_{12} & r_{13} \\ 0 & r_{22} & r_{23} \\ 0 & 0 & r_{33} \end{pmatrix} \begin{pmatrix} q_{11} & q_{12} & q_{13} \\ q_{21} & q_{22} & q_{23} \\ q_{31} & q_{32} & q_{33} \end{pmatrix} , \tag{4.16}$$

where $\boldsymbol{R}$ is an upper triangular and $\boldsymbol{Q}$ is an orthogonal matrix. RQ factorization is not unique, but possible solutions differ only in signs. Here, the solution with $r_{11} < 0$, $r_{22} < 0$ and $r_{33} > 0$ is desired. These diagonal elements of $\boldsymbol{R}$ cannot be zero, since this would indicate a rank deficiency in $\boldsymbol{P'}$. r_{33} is unity due to the normalization of $\boldsymbol{P'}$ in equation (4.15).

The matrix $\boldsymbol{G}$ is now defined as

$$\boldsymbol{G} = \boldsymbol{V}\,\boldsymbol{A}^{-1}\,\boldsymbol{D} = \begin{pmatrix} g_{11} & g_{12} & g_{13} \\ g_{21} & g_{22} & g_{23} \\ 0 & 0 & 1 \end{pmatrix} = \begin{pmatrix} \dfrac{-D\,(1-a_1)}{1-(a_1^2+a_2^2)} & \dfrac{D\,a_2}{1-(a_1^2+a_2^2)} & u_{\mathrm{foc}} \\ \dfrac{D\,a_2}{1-(a_1^2+a_2^2)} & \dfrac{-D\,(1+a_1)}{1-(a_1^2+a_2^2)} & v_{\mathrm{foc}} \\ 0 & 0 & 1 \end{pmatrix}, \quad (4.17)$$

which implies $g_{12} = g_{21}$, $g_{11} < 0$ and $g_{22} < 0$ because of the constraints $|a_1| < 1$, $|a_2| < 1$ and $D > 0$ introduced in subsection 4.1.3.

An orthogonal matrix $\boldsymbol{K}$ is then sought such that $\boldsymbol{G} = \boldsymbol{R}\,\boldsymbol{K}$. The matrix $\boldsymbol{K}$ must be composed of the elementary rotation

$$\boldsymbol{K} = \begin{pmatrix} \cos\kappa & \sin\kappa & 0 \\ -\sin\kappa & \cos\kappa & 0 \\ 0 & 0 & 1 \end{pmatrix}, \quad (4.18)$$

where, because of $g_{12} = g_{21}$, the angle of rotation is determined by

$$\tan\kappa = -\frac{r_{12}}{r_{11} + r_{22}}\,. \quad (4.19)$$

The denominator in equation (4.19) cannot be zero due to the conditions $r_{11} < 0$ and $r_{22} < 0$ required in the RQ factorization above. The matrix elements of $\boldsymbol{K}$ can be computed directly by

$$\sin\kappa = \frac{\tan\kappa}{\sqrt{1+\tan^2\kappa}} \quad \text{and} \quad \cos\kappa = \frac{1}{\sqrt{1+\tan^2\kappa}}\,. \quad (4.20)$$

According to the definition in equation (4.17), the focus-to-detector distance D is obtained from $\boldsymbol{G}$ by

$$D = \frac{-2\,(g_{11}\,g_{22} - g_{12}^2)}{g_{11} + g_{22}}\,. \quad (4.21)$$

The coefficients a_1 and a_2, which compensate for a deviation in scale and a lack of orthogonality between the detector axes, are computed by

$$a_1 = \frac{g_{22} - g_{11}}{g_{11} + g_{22}} \quad \text{and} \quad a_2 = \frac{-2\,g_{12}}{g_{11} + g_{22}}\,. \quad (4.22)$$

The denominator of equations (4.21) and (4.22) cannot be zero because of $g_{11} < 0$ and $g_{22} < 0$. Finally, the coordinates of the view reference point are directly provided by $\boldsymbol{G}$,

$$u_{\text{foc}} = g_{13} \quad \text{and} \quad v_{\text{foc}} = g_{23} \,. \tag{4.23}$$

The decomposition of $\boldsymbol{P'} = \boldsymbol{G}\,\boldsymbol{S} = \pm\left(\boldsymbol{R}\,\boldsymbol{K}\right)\left(\boldsymbol{K}^{-1}\,\boldsymbol{Q}\right)$ is completed by considering the correct sign of the scaling factor λ by

$$\operatorname{sign}\lambda = \det\left(\boldsymbol{K}^{-1}\,\boldsymbol{Q}\right) \quad \text{and} \quad \boldsymbol{S} = \operatorname{sign}\lambda\,\left(\boldsymbol{K}^{-1}\,\boldsymbol{Q}\right)\,, \tag{4.24}$$

where $\boldsymbol{K}^{-1} = \boldsymbol{K}^{\mathrm{T}}$ because $\boldsymbol{K}$ is orthogonal. The Euler angles ϕ, θ, ψ are then obtained from the matrix $\boldsymbol{S}$ by

$$\phi = \arctan\left(\frac{s_{31}}{s_{33}}, \frac{-s_{32}}{s_{33}}\right)\,, \quad \psi = \arctan\left(\frac{s_{13}}{s_{33}}, \frac{s_{23}}{s_{33}}\right)\,, \quad \theta = \arccos s_{33}\,, \tag{4.25}$$

where the arctangent function with two arguments returns an angle between $-\pi$ and π, considering the signs of the numerator and denominator. Equation (4.25) cannot be applied if $s_{33} = \pm 1$. This situation, however, does not occur in practice for the given divergent-beam geometry.

Beside the above decomposition of a projection matrix $\boldsymbol{P}$ into 11 geometric parameters, the following information can be obtained from $\boldsymbol{P}$.

A vector $\boldsymbol{r}_{u,v}$ pointing from the focus to the point $(u,v)^{\mathrm{T}}$ on the detector can be calculated from $\boldsymbol{P}$ by the vector product

$$\boldsymbol{r}_{u,v} = \left(\boldsymbol{p}_1 - u\,\boldsymbol{p_3}\right) \times \left(\boldsymbol{p}_2 - v\,\boldsymbol{p_3}\right)\,, \tag{4.26}$$

where $\boldsymbol{p}_j = \left(p_{j1}, p_{j2}, p_{j3}\right)^{\mathrm{T}}$.

The scaling factor λ in the relation $\lambda\,(u,v,1)^{\mathrm{T}} = \boldsymbol{P}\,(x,y,z,1)^{\mathrm{T}}$ is proportional to the distance $L\left(\boldsymbol{r}\right)$ from the focus to the point $\boldsymbol{r} = (x,y,z)^{\mathrm{T}}$ projected onto the central ray. More specifically,

$$\lambda = L\left(\boldsymbol{r}\right)\,\left(p_{31}^2 + p_{32}^2 + p_{33}^2\right)\,. \tag{4.27}$$

If $\boldsymbol{P}$ is normalized such that $p_{34} = 1$ and R is the focus-to-isocentre distance as defined previously, the relation

$$\lambda = \frac{L\left(\boldsymbol{r}\right)}{R} \tag{4.28}$$

can be derived from equation (4.7). This is advantageous, since $R^2/L^2(\boldsymbol{r})$ needs to be calculated in divergent-beam filtered-backprojection algorithms for each voxel to be reconstructed.

Provided the object coordinates of the isocentre are known, the view angle α for a particular projection can be calculated using the result of equation (4.13) as

$$\alpha = \arctan\left(x_{\mathrm{foc}} - x_{\mathrm{iso}}, y_{\mathrm{iso}} - y_{\mathrm{foc}}\right) . \tag{4.29}$$

Furthermore, the projection of the isocentre yields the view reference point in each view without explicit decomposition of $\boldsymbol{P}$,

$$\lambda\ \left(u_{\mathrm{foc}}, v_{\mathrm{foc}}, 1\right)^{\mathrm{T}} = \boldsymbol{P}\ \left(x_{\mathrm{iso}}, y_{\mathrm{iso}}, z_{\mathrm{iso}}, 1\right)^{\mathrm{T}} , \tag{4.30}$$

since the isocentre is the intersection of all central rays. The above equation simplifies to

$$u_{\mathrm{foc}} = \frac{p_{14}}{p_{34}} \quad \text{and} \quad v_{\mathrm{foc}} = \frac{p_{24}}{p_{34}} \tag{4.31}$$

if the isocentre is located at the origin of the object coordinate system. A mechanically unstable system such as a C-arm angiography device, however, may not have a well-defined isocentre. The equations (4.29), (4.30) and (4.31) are then approximate assuming an average isocentre position that fits best to the source trajectory.

4.2 Projection data acquisition

For two-dimensional computed tomography, a diagnostic Siemens Somatom Plus 4 scanner, shown in the left panel of figure 4.2, was utilized to record fan-beam projections. Cone-beam projections were acquired at a Siemens Primus linear accelerator and a Siemens SimView therapy simulator. For this purpose, a PerkinElmer Optoelectronics RID 256-L flat-panel imager was attached to the gantry of these devices such as shown in the right panel of figure 4.2. In the following two subsections, the data acquisition hardware is described from the technical point of view, using the mathematical notation introduced previously. Furthermore, the scan parameters, that were constant for all experiments, are listed.

4.2.1 Fan-beam computed tomography

The *Siemens Somatom Plus 4* scanner provides sequential (slice-by-slice) and helical data acquisition schemes. The X-ray source is placed at a distance R of 57 cm from the axis of rotation. The distance from the focal spot to the curved single-row detector, D, equals 100.5 cm.

The maximum tube voltage is 150 kV. Using a 120 kVp beam such as for many diagnostic CT examinations, the tube current ranges from 50 to 320 mA. The size of the focal spot is either $0.6 \times 0.6\,\mathrm{mm}^2$ or $0.8 \times 1.1\,\mathrm{mm}^2$.

A Somatom Plus 4 scanner records 1056 projections equally spaced over the full circle. A complete gantry rotation takes 0.75 s or 1.5 s, depending on the mode which is chosen. Each projection comprises 768 bins at an angular pitch of $4.0625'$, resulting in a fan opening angle $2\beta_{\mathrm{max}}$ of 52°.

Two different technical tricks are implemented that allow fulfilment of the Nyquist condition for sufficient sampling of the fan-beam projections.

1. The first option is to displace the central ray by a quarter of the bin size. The effective sampling pitch equals then half of the bin size because each ray is measured twice during a full gantry rotation.

2. Alternatively, the position of the focal spot on the anode can be modulated electronically. Using this feature, each projection is sampled twice during continuous gantry rotation at an angular displacement of half of the bin size. The combined projection for a given view angle consists then of 1536 samples. Consequently, the Nyquist condition on sufficient sampling is fulfilled for each projection and not only for the complete 2π scan.

The second option is obviously preferable if short-scan approaches are used, i.e., images are to be reconstructed from a range of projection view angles less than 2π.

4.2.2 Cone-beam computed tomography

For the *Siemens Primus* linear accelerator and the *Siemens SimView* therapy simulator, the source-to-isocentre distance R equals 100 cm. The flat-panel imager was placed at a distance D of about 130 cm from the focal spot. Using the linear accelerator, an in-house built mechanical support frame was employed to attach the detector to the gantry, whereas the flat-panel was mounted on top of the built-in image intensifier of the therapy simulator.

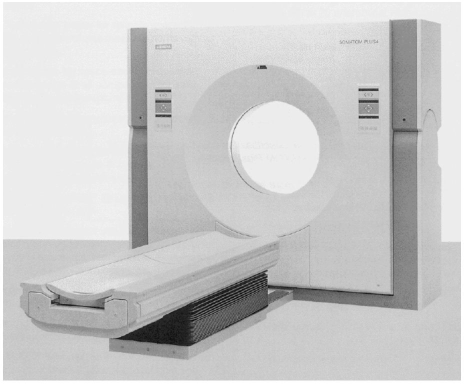

Figure 4.2: Equipment utilized for X-ray projection data acquisition. The left panel shows a Somatom Plus 4 scanner for diagnostic fan-beam CT. The right panel shows a Siemens SimView therapy simulator combined with a PerkinElmer Optoelectronics RID 256-L flat-panel imager for cone-beam CT.

For kilovoltage imaging at the SimView, a tube voltage of 150 kV and an exposure per view of 5 mAs were chosen to exploit the full dynamic range of the flat-panel imager. The megavoltage scans were taken with a 6 MV beam from the Primus linear accelerator. Each view was acquired using one monitor unit,[1] which is the smallest output deliverable for a single field.

The projections were normally recorded manually in step-and-shoot mode because a gating option for synchronizing the X-ray output and the detector integration window was not available. The control software of the linear accelerator and the therapy simulator allows to select the gantry angle in steps of 1°. This yields a maximum number of 360 projections per full revolution for the step-and-shoot mode.

The *PerkinElmer Optoelectronics RID 256-L* flat-panel imager comprises a phosphor layer ($133\,\mathrm{mg\,cm^{-2}}$ $Gd_2O_2S:Tb$) directly coupled to an array of 256×256 photodiodes made of amorphous silicon. The pixel pitch in each direction is 0.8 mm resulting in a sensitive area of $20.48 \times 20.48\,\mathrm{cm}^2$. Measured data are digitized into 12 bit per pixel. Possible integration times are 80 ms, 100 ms, 200 ms, 400 ms, 800 ms, 1600 ms, 3200 ms and 6400 ms. Here, the 3200 ms and 6400 ms integration times were chosen to allow manual synchronization in the step-and-shoot acquisitions. The 1 mm aluminium cover plate supplied was replaced by a 3 mm copper plate for some of the megavoltage experiments using the linear accelerator.

[1] One monitor unit is defined as the linear accelerator output needed to deliver a dose of 1 cGy under reference conditions (source-to-surface distance 100 cm, water depth 5 cm, field size $10 \times 10\,\mathrm{cm}^2$).

4.3 Projection data preprocessing

The object function $f(\boldsymbol{r})$ to be reconstructed in X-ray computed tomography is the distribution of the linear attenuation coefficients $\mu(E)$ at a particular energy E. The data measured by the detector, however, do not directly represent the line integrals $g(\alpha, u, v)$ through $f(\boldsymbol{r})$. They require therefore some preprocessing steps that consider several physical effects and technical properties of the detector to obtain an estimate of $g(\alpha, u, v)$.

The raw data captured by the diagnostic fan-beam CT scanner described subsection 4.2.1 are corrected automatically during the acquisition. The manual preprocessing steps utilized for the experimental cone-beam systems involving a flat-panel imager as introduced in subsection 4.2.2 are explained in the following.

4.3.1 Dark current correction

Flat-panel imagers exhibit a background signal that does not depend on the amount of X-ray exposure. The dark current is present even when there is no exposure at all. After a particular warm-up period of the detector, the dark signal is relatively stable with time, but it varies from pixel to pixel. This effect needs therefore to be considered carefully in order to avoid reconstruction artefacts.

Before an actual CT scan, a series of about 40 to 50 dark frames is acquired and averaged in order to minimize the introduction of (electronic and thermal) random noise. The averaged dark image is then subtracted from each captured projection prior to further processing. The dark and actual measurements have to be taken using the same integration times.

4.3.2 Bad pixel correction

In flat-panel imagers, not only the offset (dark current) varies between pixels, but also the gain factor. This is taken into account by means of the open field calibration described in the next subsection. A small percentage of pixels, however, cannot be calibrated successfully, and may even be completely defective. Using third-generation CT scanning mode, these pixels cause ring artefacts in the reconstructed images.

A flat-panel detector is therefore characterized by a bad pixel map, which is obtained once and stored permanently. The few bad pixels are normally randomly distributed across the field and do not occur in large clusters. It is therefore sufficient to calculate the value of all bad pixels from their neighbourhood by median filtering for each captured frame.

4.3.3 Open field calibration

As mentioned above, the gain factor varies from pixel to pixel because of technical limitations. Furthermore, the incident photon fluence and mean energy are not uniform across the whole field, and their spatial distributions are normally unknown.

To consider these effects, a calibration measurement is performed (normally in air), using the same integration time as for the acquisition of the actual projections of the object. The open frames should be captured immediately before or after the actual CT scan in order to decrease the influence of X-ray output fluctuations.

Multiple open frames are recorded in order to minimize the introduction of additional random noise that is caused by the Poisson photon statistics and by the read-out electronics of the detector. There are two approaches for the normalization to obtain an estimate of the line integrals. The open frames can be taken at a particular view angle α_0 and averaged,

$$g(\alpha, u, v) = -\ln\left(\frac{I_{\text{obj}}(\alpha, u, v)}{\bar{I}_{\text{air}}(\alpha_0, u, v)}\right). \tag{4.32}$$

Alternatively, the one or more open frames can be recorded for each view independently,

$$g(\alpha, u, v) = -\ln\left(\frac{I_{\text{obj}}(\alpha, u, v)}{\bar{I}_{\text{air}}(\alpha, u, v)}\right). \tag{4.33}$$

Provided the overall number of open frames is equal, both approaches yield the same signal-to-noise ratio in the reconstructed CT images. The second method, however, is preferable when the spatial distribution of the source fluence is non-uniform and flex effects need to be considered.

As a results of this open field calibration, the linear attenuation coefficient of air is represented by zero in the CT images, i.e., all reconstructed values are decreased by μ_{air}.

4.3.4 Beam-hardening and scatter correction

The estimation of the line integrals $g(\alpha, u, v)$ by an open field calibration is often not sufficient, especially, when quantitative information about the absorption is desired. This is mainly because of two physical effects.

1. The linear attenuation coefficients to be reconstructed as well as the efficiency of the detector depend on the photon energy. Since the output of an X-ray tube or a linear accelerator is not monoenergetic, the signal is averaged over the energy spectrum.

2. At the photon energies utilized for X-ray imaging, Compton scattering is a significant interaction process. Scattered photons do not travel along the integration lines from the focus to the detector pixels, but nevertheless they are potentially detected.

Both of these effects are non-linear, i.e., they violate the assumptions that are made in image reconstruction algorithms. The method utilized to correct the projection images for these effects, at least to certain extent, is outlined in the following.[2]

The intensity of the scatter component is estimated by means of a superposition method summing the scatter contribution from each pixel to every other pixel in the detector. Convolution kernels are pre-calculated for various object-to-detector air gaps, path lengths and object radii using a dedicated Monte Carlo code [118]. For each ray through the phantom, the most appropriate kernel is selected from this library.

A series of calibration measurements is performed occasionally to account for the energy spectrum of the primary beam and the response of the detector. For this purpose, transmission images of water-equivalent phantoms with different, accurately known thickness are acquired. The data are fitted to a linear-quadratic model, which describes the relation between water-equivalent thickness and measured intensity sufficiently accurate [117].

Combining the scatter estimation and the detector calibration method yields a quadratic equation, which needs to be solved for the water-equivalent thicknesses of each transmission image of an actual CT scan. Since the scatter component to be subtracted from the measured intensity is a function of the water thickness, this equation cannot be solved directly. An iterative procedure is therefore used, which, in practice, converges to an acceptably accurate solution within 3 or 4 steps [114].

[2] This correction was only applied to megavoltage scans.

4.4 Geometric calibration

The experimental cone-beam CT scanners introduced in subsection 4.2.2 are comprised of a flat-panel imager attached to a linear accelerator or a radiotherapy simulator. These devices exhibit significant mechanical instabilities, thus requiring the application of a sophisticated geometric calibration method. The diagnostic fan-beam CT scanner described in subsection 4.2.1 does not need to be calibrated geometrically, since its components are perfectly aligned.

Geometric calibration of the cone-beam scanners was achieved by scanning a dedicated phantom, which consists of an array of fiducial markers. Based on the accurately known positions of these markers and their estimated locations in the recorded images, the projection geometry was calculated for each view independently.

According to the classification of calibration methods introduced in subsection 3.4.1, this is a local technique. The following (mathematical) description is therefore provided for an arbitrary view without referring to a particular view angle α in order to simplify the formulae.

4.4.1 Calibration phantom

The in-house built phantom shown in figure 4.3, which was utilized for geometric calibration, is very similar to those introduced by Roguée et al. [99]. It consists of a hollow Perspex cylinder with 37 small ball bearings made of steel embedded in its wall. These markers are arranged along a helical trajectory of radius 67.5 mm. The axial spacing of the fiducial markers is 6 mm. The diameter of the ball bearings equals 3 mm, except for the central one, which has a diameter of 5 mm. In addition to the original design suggestions, lines are engraved on the surface of the Perspex cylinder that indicate its longitudinal axis and its centre.

The axis of rotation of the X-ray source is assumed to be nearly parallel to the longitudinal axis of the marker helix. Without loss of generality, the rows of the detector are required to be approximately parallel to the base of the cylinder. If this requirement is not fulfilled during the calibration scan, the original projections can be rotated, which then needs to be considered during the detection of the markers described in the following subsection. The larger ball bearing serves as a reference and has to appear in all projection images.

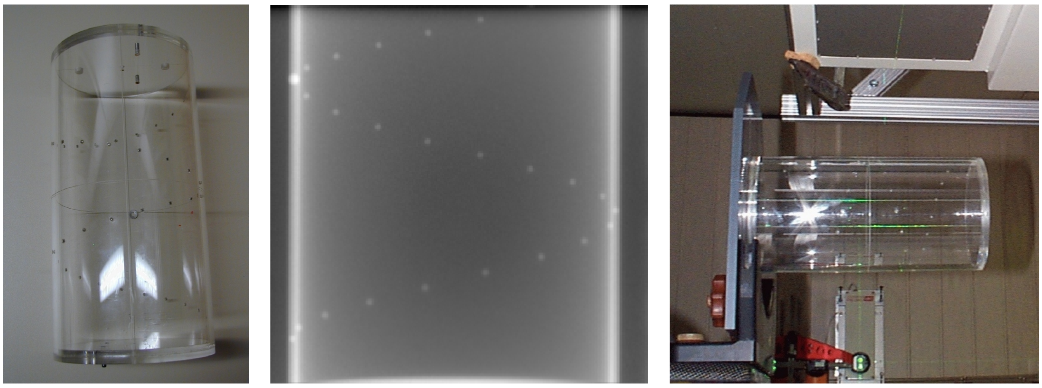

Figure 4.3: Phantom for geometric calibration comprising 37 ball bearings arranged along a helical trajectory; normalized X-ray projection of the phantom; alignment of the phantom at the isocentre of a linear accelerator using laser marks (from left to right).

Due to the phantom design and the assumptions mentioned above, the ball bearings show up along a sine-shaped path in each projection image as shown in figure 4.3.

In summary, the calibration phantom exhibits the following advantageous properties.

- The number of fiducial markers is sufficiently large, and they are well distributed in three-dimensional space, in order to obtain an accurate estimation of the projection geometry for each view.[3]

- In none of the views can the ball bearings hide each other, which simplifies their automatic detection in the X-ray projections.

- The order of the markers along the axis of the cylinder is in agreement with their order by column index in all projection images. In the case of axial truncation, absolute numbering can be achieved by using the larger ball bearing as reference.

- The phantom can be aligned with respect to a particular frame of reference using laser marks and the engraved lines. This is shown for the linear accelerator in figure 4.3.

The basic design of the calibration phantom is well-suited to be used with all source trajectories depicted in figure 3.1 on page 18.

[3]This statement is corroborated in subsection 5.1.3 via computer simulations.

4.4.2 Detection of fiducial markers

Based on the properties of the calibration phantom, an algorithm for the detection of the ball bearings in each projection image was designed. The algorithm works as follows.

1. In a preprocessing step, the background of the projection image is removed along the axis of the cylinder. This is done by low-pass filtering of each column vector of the detector and subtracting the result from the original one. The image then exhibits a uniform background (except for noise). In particular, the walls of the Perspex cylinder are eliminated by this procedure.

2. A threshold for the segmentation of the ball bearings is chosen as certain percentage of the maximum value, which is definitely above the background noise. Image regions that potentially represent a ball bearing because of high absorption are labelled by applying this threshold.

3. All labelled regions are checked for their size and their shape. Regions that are non-circular, too small or too large are excluded based on approximate, prior knowledge of the imaging geometry.

4. For all regions remaining after the previous step, the centre of gravity is calculated in order to estimate the location of the centre of each ball bearing in the X-ray projection. These positions are denoted as u_k, v_k ($k = 1, \ldots, K$).

5. All K detected ball bearings are finally sorted by their column coordinate v_k. The largest region is sought in order to obtain the desired absolute correspondence to the known three-dimensional coordinates x_k, y_k, z_k of the ball bearings within the phantom.

This algorithm works automatically in many cases. A manual definition of a particular region of interest can be necessary if structures other than the cylinder phantom are imaged.

4.4.3 Parametric calibration method

Based on the known positions x_k, y_k, z_k of the K markers and their locations u_k, v_k in the X-ray projection obtained in the previous step, a set of parameters describing the particular projection geometry can be estimated. The eleven geometric parameters $\boldsymbol{\omega} = (x_{\text{foc}}, y_{\text{foc}}, z_{\text{foc}}, \phi, \theta, \psi, D, a_1, a_2, u_{\text{foc}}, v_{\text{foc}})$ utilized here refer to equation (4.7) on page 36.

The geometric parameters are estimated by minimizing the mean quadratic deviation between the position of the markers in the X-ray image and their reprojected locations,

$$\Delta s^2(\boldsymbol{\omega}) = \frac{1}{K}\sum_{k=1}^{K}\left(\Delta u_k^2(\boldsymbol{\omega}; x_k, y_k, z_k, u_k) + \Delta v_k^2(\boldsymbol{\omega}; x_k, y_k, z_k, v_k)\right), \quad (4.34)$$

where

$$\Delta u_k = \frac{p_{11}(\boldsymbol{\omega})\ x_k + p_{12}(\boldsymbol{\omega})\ y_k + p_{13}(\boldsymbol{\omega})\ z_k + p_{14}(\boldsymbol{\omega})}{p_{31}(\boldsymbol{\omega})\ x_k + p_{32}(\boldsymbol{\omega})\ y_k + p_{33}(\boldsymbol{\omega})\ z_k + p_{34}(\boldsymbol{\omega})} - u_k\,, \quad (4.35)$$

$$\Delta v_i = \frac{p_{21}(\boldsymbol{\omega})\ x_k + p_{22}(\boldsymbol{\omega})\ y_k + p_{23}(\boldsymbol{\omega})\ z_k + p_{24}(\boldsymbol{\omega})}{p_{31}(\boldsymbol{\omega})\ x_k + p_{32}(\boldsymbol{\omega})\ y_k + p_{33}(\boldsymbol{\omega})\ z_k + p_{34}(\boldsymbol{\omega})} - v_k \quad (4.36)$$

and the projection matrix $\boldsymbol{P}$ is composed from $\boldsymbol{\omega}$ according to equation (4.7). The minimization of $\Delta s^2(\boldsymbol{\omega})$ is performed using Powell's method [92] in order to obtain the desired parameter vector $\boldsymbol{\omega}$.

4.4.4 Non-parametric calibration method

As an alternative to the parametric calibration approach described in the previous subsection, the elements $p_{31}, \ldots, p_{34}$ of the projection matrix $\boldsymbol{P}$ can be calculated analytically. Each of the K fiducial markers provides three equations of the form

$$\lambda \begin{pmatrix} u_k \\ v_k \\ 1 \end{pmatrix} = \begin{pmatrix} p_{11} & p_{12} & p_{13} & p_{14} \\ p_{21} & p_{22} & p_{23} & p_{24} \\ p_{31} & p_{32} & p_{33} & p_{34} \end{pmatrix} \begin{pmatrix} x_k \\ y_k \\ z_k \\ 1 \end{pmatrix}. \quad (4.37)$$

The unknown scaling factor λ is eliminated from the system of $3K$ equations, resulting in the equivalent system of $2K$ equations

$$\boldsymbol{L}\,\boldsymbol{p} = \boldsymbol{0}\,, \quad (4.38)$$

where the vector

$$\boldsymbol{p} = \begin{pmatrix} p_{11} \\ \vdots \\ p_{34} \end{pmatrix}$$

is comprised of the desired elements of the projection matrix, $\mathbf{0}$ denotes the zero vector and

$$\boldsymbol{L} = \begin{pmatrix} \vdots & \vdots & \vdots & \vdots & \vdots & \vdots & \vdots & \vdots & \vdots & \vdots & \vdots & \vdots \\ x_k & y_k & z_k & 1 & 0 & 0 & 0 & 0 & -x_k\,u_k & -y_k\,u_k & -z_k\,u_k & -u_k \\ 0 & 0 & 0 & 0 & x_k & y_k & z_k & 1 & -x_k\,v_k & -y_k\,v_k & -z_k\,v_k & -v_k \\ \vdots & \vdots & \vdots & \vdots & \vdots & \vdots & \vdots & \vdots & \vdots & \vdots & \vdots & \vdots \end{pmatrix} .$$

The matrix $\boldsymbol{L}$ is singular independent of the number K of markers, since an additional constraint is needed to determine the overall scaling. In other words, there are 12 variables, namely the elements of the projection matrix $\boldsymbol{P}$, but only 11 degrees of freedom in the mathematical model of a conic projection.

One approach is to choose an arbitrary, but non-zero, value for one of the elements of $\boldsymbol{P}$. The traditional choice is the constraint $p_{34} = 1$ that turns equation (4.38) into another system, which can be solved in linear least-squares sense by means of its normal equations [70].

At least $K = 6$ markers are necessary to ensure the full rank 11 of this system. In fact, seven or more markers should be used, since no geometric distribution of six points guarantees the full rank for arbitrary positions of the focal point [70]. The system of equations is singular independent of the number of points if they are badly distributed in three-dimensional space, e.g., if they all lie in the same plane.

Apart from the number and distribution of markers, the constraint $p_{34} = 1$ considered above introduces a singularity if the correct value of p_{34} is (close to) zero. The alternative constraint $p_{31}^2 + p_{32}^2 + p_{33}^2 = 1$, however, is free of singularities [70]. Furthermore, this condition follows directly from the composition of $\boldsymbol{P}$ in equation (4.7) for $|\lambda| = 1$. If the original system (4.38) is written as

$$\boldsymbol{L}_1\,\boldsymbol{p}_1 + \boldsymbol{L}_2\,\boldsymbol{p}_2 = \mathbf{0} \tag{4.39}$$

with

$$\boldsymbol{L}_1 = \begin{pmatrix} \vdots & \vdots & \vdots & \vdots & \vdots & \vdots & \vdots & \vdots & \vdots \\ x_k & y_k & z_k & 1 & 0 & 0 & 0 & 0 & -u_k \\ 0 & 0 & 0 & 0 & x_k & y_k & z_k & 1 & -v_k \\ \vdots & \vdots & \vdots & \vdots & \vdots & \vdots & \vdots & \vdots & \vdots \end{pmatrix} , \quad \boldsymbol{p}_1 = \begin{pmatrix} p_{11} \\ \vdots \\ p_{24} \\ p_{34} \end{pmatrix}$$

and

$$\boldsymbol{L}_2 = \begin{pmatrix} \vdots & \vdots & \vdots \\ -x_k\, u_k & -y_k\, u_k & -z_k\, u_k \\ -x_k\, v_k & -y_k\, v_k & -z_k\, v_k \\ \vdots & \vdots & \vdots \end{pmatrix} , \quad \boldsymbol{p}_2 = \begin{pmatrix} p_{31} \\ p_{32} \\ p_{33} \end{pmatrix} ,$$

the least-square solution for the desired coefficients in $\boldsymbol{p}_1$ and $\boldsymbol{p}_2$ is obtained as the eigenvector corresponding to the smallest eigenvalue of the matrix

$$\boldsymbol{L}_3 = \left(\boldsymbol{L}_2^{\mathrm{T}}\, \boldsymbol{L}_2\right) - \left(\boldsymbol{L}_1^{\mathrm{T}}\, \boldsymbol{L}_2\right)^{\mathrm{T}} \left(\boldsymbol{L}_1^{\mathrm{T}}\, \boldsymbol{L}_1\right)^{-1} \left(\boldsymbol{L}_1^{\mathrm{T}}\, \boldsymbol{L}_2\right) , \tag{4.40}$$

for $\boldsymbol{p}_2$ and then by

$$\boldsymbol{p}_1 = - \left(\boldsymbol{L}_1^{\mathrm{T}}\, \boldsymbol{L}_1\right)^{-1} \left(\boldsymbol{L}_1^{\mathrm{T}}\, \boldsymbol{L}_2\right) \boldsymbol{p}_2 \tag{4.41}$$

as proved previously [70].

4.5 Image reconstruction

The algorithm proposed by Feldkamp, Davis and Kress [24] was employed for approximate image reconstruction of cone-beam data recorded using a single-circular source trajectory. The original method was modified to account for flex effects. These modifications are based on the geometric calibration procedure explained in the previous section.

Two versions of the cone-beam reconstruction algorithm are explained in the following, one for planar detectors such as flat-panel imagers and one for cylindrical detectors such as utilized in diagnostic multi-row CT scanners. The modification of these algorithms that is necessary to process short-scan data sets is then described. Furthermore, some well-known properties of the Feldkamp algorithm [24] are listed.

Fan-beam reconstruction algorithms are not explicitly mentioned, since they can be easily derived as special case for $z = 0$ from the three-dimensional problem. In this section, the mathematical notation is based on continuous variables. In appendix C, however, the efficient practical implementation of the formulae on a digital computer using discrete data is addressed.

4.5.1 Algorithm for planar detectors

Step 1. The projection data $g(\alpha, u, v)$, preprocessed as explained in section 4.3, are weighted to account for the divergent beam,

$$g_1(\alpha, u, v) = g(\alpha, u, v)\ \frac{D(\alpha)}{\sqrt{D^2(\alpha) + (u - u_{\mathrm{foc}}(\alpha))^2 + (v - v_{\mathrm{foc}}(\alpha))^2}}\,. \tag{4.42}$$

The weighting term in the above equation is slightly modified compared to the original one to correct for flex effects. The offsets $u_{\mathrm{foc}}(\alpha)$ and $v_{\mathrm{foc}}(\alpha)$ account for a non-centred detector. These values as well as the source-to-detector distance, $D(\alpha)$, are considered for each view angle, α, independently.[4]

Step 2. The weighted projections $g_1(\alpha, u, v)$ are filtered one-dimensionally along lines parallel to the plane of source rotation,

$$g_2(\alpha, u, v) = \int_{u_{\min}}^{u_{\max}} g_1(\alpha, u', v)\ h(u - u')\ \mathrm{d}u'\,. \tag{4.43}$$

The kernel $h(u)$ is one of the well-known parallel-beam filters as introduced in appendix A. The convolution integral does not change if offsets along the detector axes, u and v, are introduced. Potential tilts of the detector with respect to the plane of source rotation are not considered in the above equation.[5]

Step 3. A cone-beam backprojection of the filtered projections $g_2(\alpha, u, v)$ into the reconstruction volume is finally performed to obtain the object function

$$f(\boldsymbol{r}) = \frac{1}{2} \int_{\alpha_{\min}}^{\alpha_{\max}} \frac{R^2(\alpha)}{L^2(\alpha, \boldsymbol{r})}\, g_2(\alpha, u(\alpha, \boldsymbol{r}), v(\alpha, \boldsymbol{r}))\ \mathrm{d}\alpha\,. \tag{4.44}$$

The functions $u(\alpha, \boldsymbol{r})$ and $v(\alpha, \boldsymbol{r})$ map the object coordinates $\boldsymbol{r} = (x, y, z,)^{\mathrm{T}}$ onto detector coordinates u, v for a particular view angle α. $L(\alpha, \boldsymbol{r})$ is the distance from the focus to the point $\boldsymbol{r}$ to be reconstructed, projected onto the central ray and $R(\alpha)$ is the source-to-isocentre distance. All these geometric parameters are conveniently obtained from the projection matrices $\boldsymbol{P}_\alpha$ using equations (4.5), (4.6) and (4.28).

[4] This mathematically rigorous treatment of geometric misalignments has minor impact on the reconstruction result. For the cone-beam geometry specified in subsection 4.2.2, the weighting term varies only by 1 %. The correction is therefore almost negligible, since the geometric uncertainties usually do not exceed a few detector pixels.

[5] Typical flex effects do not result in significant tilts. It is therefore fairly reasonable to keep this step unchanged.

4.5.2 Algorithm for cylindrical detectors

A cone-beam reconstruction algorithm for cylindrical detectors can be derived from those for planar projections by introducing the coordinate transform from u to β using equation (4.1). This subsection is intended to emphasize only the corresponding changes compared to the previous one.

Step 1. The projections $g(\alpha, \beta, v)$ are weighted to account for the cone-beam geometry,

$$g_1(\alpha, \beta, v) = g(\alpha, \beta, v) \, \frac{R(\alpha) \cos\beta}{\sqrt{R^2(\alpha) + (v - v_{\text{foc}}(\alpha))^2}} \,. \tag{4.45}$$

Step 2. The weighted projections $g_1(\alpha, \beta, v)$ are filtered one-dimensionally along lines parallel to the plane of source rotation,

$$g_2(\alpha, \beta, v) = \int_{\beta_{\min}}^{\beta_{\max}} g_1(\alpha, \beta', v) \; h(\beta - \beta') \; \mathrm{d}\beta' \,, \tag{4.46}$$

where $h(\beta)$ is a filter kernel known from fan-beam algorithms for curved detectors.

Step 3. The filtered projections $g_2(\alpha, \beta, v)$ are backprojected to yield the desired object function $f(\boldsymbol{r})$,

$$f(\boldsymbol{r}) = \frac{1}{2} \int_{\alpha_{\min}}^{\alpha_{\max}} \frac{R^2(\alpha)}{L'^2(\alpha, \boldsymbol{r})} \, g_2(\alpha, \beta(\alpha, \boldsymbol{r}), v(\alpha, \boldsymbol{r})) \; \mathrm{d}\alpha \,. \tag{4.47}$$

Whereas $v(\alpha, \boldsymbol{r})$ is provided by $\boldsymbol{M}_\alpha$ as explained previously, the fan angle $\beta(\alpha, \boldsymbol{r})$ cannot be directly obtained from the projection matrix, but needs to be calculated separately using equation (4.1). The distance $L'(\alpha, \boldsymbol{r})$ from the focus to the point $\boldsymbol{r}$ to be reconstructed projected onto the plane $z = 0$ is also not immediately delivered by $\boldsymbol{M}_\alpha$.

Step 2a. The latter problem concerning the distance $L'(\alpha, \boldsymbol{r})$ can be avoided if the post-filtering weighting

$$g_{2\text{a}}(\alpha, \beta, v) = g_2(\alpha, \beta, v) \, \cos^2\beta \tag{4.48}$$

is added. In the backprojection of $g_{2\text{a}}(\alpha, \beta, v)$ in step 3, the distance $L'(\alpha, \boldsymbol{r})$ is then replaced by $L(\alpha, \boldsymbol{r})$ introduced in the previous subsection.

4.5.3 Short-scan algorithms

For short-scan data sets with a view angle range of $\pi + 2\beta_{\max} \leq \alpha_{\max} - \alpha_{\min} < 2\pi$ and an over-scan $\alpha^* = \alpha_{\max} - \alpha_{\min} - \pi - 2\beta_{\max}$, the weighting term

$$w(\alpha, \beta) = S\left(\frac{\alpha}{2\beta_{\max} - 2\beta + \alpha^*} - \frac{1}{2}\right) - S\left(\frac{\alpha - \pi + 2\beta}{2\beta_{\max} + 2\beta + \alpha^*} - \frac{1}{2}\right) \quad (4.49)$$

proposed by Parker [85] is introduced additionally into equation (4.42) or equation (4.45), respectively. For cylindrical detectors, the fan angle β is given directly. For planar detectors, β is calculated using equation (4.1). The function S is defined by

$$S(q) = \begin{cases} 0 & \text{if} \quad q \leq -\frac{1}{2}\,, \\ 1 + \sin(\pi\, q) & \text{if} \quad |q| < \frac{1}{2}\,, \\ 2 & \text{if} \quad q \geq \frac{1}{2}\,. \end{cases} \quad (4.50)$$

An alternative weighting function and a general discussion on short-scan reconstruction was presented by Wesarg et al. [132].

4.5.4 Properties

Feldkamp, Davis and Kress [24] proved the following three properties of their approximate filtered-backprojection algorithm.

- The reconstruction is exact in the mid-plane, $z = 0$. This is obvious, since the above equations reduce to the well-known fan-beam reconstruction formulae for $z = 0$.
- The reconstruction is exact for objects that are homogeneous in z direction, i.e., when $f(x, y, z) = f(x, y)$. In this case, the divergent-beam geometry is completely compensated by the pre-weighting step such that $g_1(\alpha, u, v) = g_1(\alpha, u)$. The algorithm reduces therefore again to two-dimensional fan-beam reconstruction.
- The integral value of the object function along lines parallel to the z axis, $\int f(x, y, z)\, \mathrm{d}z$, is preserved, since the three-dimensional Radon transform can be computed for all planes perpendicular to $z = 0$ from the cone-beam projections of a single-circular scan.

The third property implies that the main degradation of image quality due to missing data is blurring in the axial direction. This blurring affects only those parts of the object that are not homogeneous in z direction, since the cone-beam transform is linear.

4.6 Image restoration

This section describes the method of *projections onto convex sets* (POCS) utilized for image restoration from incomplete projection data and prior information. A thorough introduction to the method of projections onto convex sets was presented by You-la and Webb [139]. Section A.4 provides a summary of the POCS theory.

The object function $f(\boldsymbol{r})$ is estimated in POCS from an initial image $f^{(0)}(\boldsymbol{r})$ (frequently the zero image) by means of the iterative procedure[6]

$$f^{(t+1)}(\boldsymbol{r}) = \mathcal{C}_K \, \mathcal{C}_{K-1} \ldots \mathcal{C}_1 \, f^{(t)}(\boldsymbol{r}) \; , \quad t = 0, 1, 2, \ldots \; , \tag{4.51}$$

where the $\mathcal{C}_k$ $(k = 1, \ldots, K)$ denote *constraint operators* that enforce consistency of the function $f(\boldsymbol{r})$ with its measured projections and prior information. The application of $\mathcal{C}_k$ to some function yields its nearest neighbour,[7] that is an element of a particular *constraint set* C_k. The purpose of the following subsections is to introduce various constraint sets C_k and associated operators $\mathcal{C}_k$ rigorously.

In particular, the set C_{g_m} of functions that are consistent with a measured line integral g_m is defined below. Using a discrete version of $m = 1, \ldots, M$ such constraints and no other conditions, the POCS procedure

$$f^{(t+1)}(\boldsymbol{r}) = \mathcal{C}_{g_M} \ldots \mathcal{C}_{g_2} \, \mathcal{C}_{g_1} \, f^{(t)}(\boldsymbol{r}) \; , \quad t = 0, 1, 2, \ldots \tag{4.52}$$

becomes equivalent to the well-known *additive algebraic reconstruction technique* (AART). Furthermore, the set C_Ω of functions that are zero outside the region Ω and the set C_F of functions that exhibit a particular Fourier spectrum within the range F in frequency space are defined in the following. Applying only these two constraints yields the *Gerchberg-Papoulis algorithm* for analytical continuation [27, 84] that reads as

$$f^{(t+1)}(\boldsymbol{r}) = \mathcal{C}_\mathsf{F} \, \mathcal{C}_\Omega \, f^{(t)}(\boldsymbol{r}) \tag{4.53}$$

in POCS notation. These two examples show that POCS is a quite general approach that covers a whole class of iterative image restoration methods, although not all possible techniques.

[6] This iterative scheme is a simplified version of equation (4.51) obtained by setting all relaxation parameters to unity. Relaxation is ignored for the moment.

[7] The nearest neighbour is meant in the sense of minimum norm, which is explained in section A.4 in detail.

4.6.1 Consistency with projection data

Each parallel-beam projection $g(\alpha, s)$ determines the Fourier transform along a line through the origin of frequency space as shown in theorem A.5. A potentially useful constraint is therefore the set

$$\mathsf{C}_{\mathsf{F}} = \left\{ f(\boldsymbol{r}) : F(\boldsymbol{\rho}) = \mathcal{F} f(\boldsymbol{r}) = G(\boldsymbol{\rho}) \quad \forall \boldsymbol{\rho} \in \mathsf{F} \right\} \tag{4.54}$$

of functions $f(\boldsymbol{r})$ that exhibit a particular Fourier spectrum $G(\boldsymbol{\rho})$ within a certain range F of frequency space. The corresponding constraint operator is defined by

$$\mathcal{C}_{\mathsf{F}} f(\boldsymbol{r}) = \mathcal{F}^{-1} F'(\boldsymbol{\rho}) \ , \quad F'(\boldsymbol{\rho}) = \begin{cases} G(\boldsymbol{\rho}) & \text{for } \boldsymbol{\rho} \in \mathsf{F} \, , \\ F(\boldsymbol{\rho}) & \text{for } \boldsymbol{\rho} \notin \mathsf{F} \, . \end{cases} \tag{4.55}$$

Although this operator is closely related to the method of direct Fourier reconstruction, it can be implemented by means of filtered backprojection and reprojection as well.

As an alternative to the Fourier constraint, the information from the projection data can be considered by introducing a separate constraint for each single measurement[8] $g_m = g(\alpha_m, u_m, v_m)$ that is defined by

$$g_m = \mathcal{D}_m f(\boldsymbol{r}) = \int\limits_{\mathsf{R}^N} f(\boldsymbol{r}) \, \chi_m(\boldsymbol{r}) \, \mathrm{d}^N r \, . \tag{4.56}$$

$\chi_m(\boldsymbol{r})$ is a characteristic function for the line or strip integration corresponding to measurement g_m. The set

$$\mathsf{C}_{g_m} = \left\{ f(\boldsymbol{r}) : \mathcal{D}_m f(\boldsymbol{r}) = g_m \right\} \tag{4.57}$$

contains all functions $f(\boldsymbol{r})$ that are consistent with this particular measurement g_m. The constraint operator is then given by

$$\mathcal{C}_{g_m} f(\boldsymbol{r}) = f(\boldsymbol{r}) + \frac{g_m - \mathcal{D}_m f(\boldsymbol{r})}{\|\chi_m(\boldsymbol{r})\|} \chi_m(\boldsymbol{r}) \ . \tag{4.58}$$

This means that the difference between the measurement g_m and the value $\mathcal{D}_m f(\boldsymbol{r})$ reprojected from the actual image $f(\boldsymbol{r})$ is scaled by $\|\chi_m(\boldsymbol{r})\|$, backprojected and added to the previous image. If $\chi_m(\boldsymbol{r})$ describes the integration along an infinitely thin line, then $\|\chi_m(\boldsymbol{r})\|$ is the length of the corresponding line segment.

[8] The following constraint is demonstrated for the functionals D_m of the N-dimensional divergent-beam transform $\mathcal{D}$. The formulae can be easily adapted for the parallel-beam transform $\mathcal{P}$.

4.6.2 Consistency with general prior information

The image $f(\boldsymbol{r})$ is known a priori to be zero outside a particular region Ω, since every object to be considered is of finite spatial extent. $f(\boldsymbol{r})$ is therefore contained in the set

$$\mathrm{C}_\Omega = \left\{ f(\boldsymbol{r}) : f(\boldsymbol{r}) = 0 \quad \forall\, \boldsymbol{r} \notin \Omega \right\} \tag{4.59}$$

of all functions that are compactly supported in Ω. The operator restricting a function to this set is

$$\mathcal{C}_\Omega\, f(\boldsymbol{r}) = \begin{cases} f(\boldsymbol{r}) & \text{if } \boldsymbol{r} \in \Omega\,, \\ 0 & \text{if } \boldsymbol{r} \notin \Omega\,. \end{cases} \tag{4.60}$$

In X-ray transmission computed tomography, the desired image $f(\boldsymbol{r})$ is the distribution of the linear attenuation coefficients of the object. It belongs therefore clearly to the set

$$\mathrm{C}_{\geq 0} = \left\{ f(\boldsymbol{r}) : f(\boldsymbol{r}) \geq 0 \right\}. \tag{4.61}$$

of all non-negative functions. The constraint operator for this set is given by

$$\mathcal{C}_{\geq 0}\, f(\boldsymbol{r}) = \begin{cases} f(\boldsymbol{r}) & \text{if } f(\boldsymbol{r}) \geq 0\,, \\ 0 & \text{if } f(\boldsymbol{r}) < 0\,. \end{cases} \tag{4.62}$$

The range of possible solutions can be further restricted if the values of $f(\boldsymbol{r})$ are known to lie in a particular interval $\mathrm{I} = [f_{\min}, f_{\max}]$, i.e., if it is contained in the set

$$\mathrm{C}_\mathrm{I} = \left\{ f(\boldsymbol{r}) : f_{\min} \leq f(\boldsymbol{r}) \leq f_{\max} \right\}. \tag{4.63}$$

This constraint generalizes the non-negativity condition introduced above by adding an upper limit. In X-ray CT, the attenuation coefficient of compact bone or metal (to account for implants) would be a reasonable assumption for an upper limit.

$$\mathcal{C}_\mathrm{I}\, f(\boldsymbol{r}) = \begin{cases} f_{\min} & \text{if } f(\boldsymbol{r}) < f_{\min}\,, \\ f(\boldsymbol{r}) & \text{if } f_{\min} \leq f(\boldsymbol{r}) \leq f_{\max}\,, \\ f_{\max} & \text{if } f(\boldsymbol{r}) > f_{\max} \end{cases} \tag{4.64}$$

is the constraint operator for the set C_I.

4.6.3 Consistency with reference images

One of the most powerful constraints restricting the space of possible solutions in image restoration is to enforce consistency of the desired function $f(\boldsymbol{r})$ with a reference image $\check{f}(\boldsymbol{r})$. The set

$$\mathsf{C}_{\check{f}} = \left\{ f(\boldsymbol{r}) : \left| f(\boldsymbol{r}) - \check{f}(\boldsymbol{r}) \right| \leq \varepsilon(\boldsymbol{r}), \varepsilon(\boldsymbol{r}) > 0 \right\} \tag{4.65}$$

contains all functions that are within distance $\varepsilon(\boldsymbol{r})$ from the reference image. The corresponding constraint operator is defined by

$$\mathcal{C}_{\check{f}} f(\boldsymbol{r}) = \begin{cases} \check{f}(\boldsymbol{r}) - \varepsilon(\boldsymbol{r}) & \text{if } f(\boldsymbol{r}) - \check{f}(\boldsymbol{r}) < -\varepsilon(\boldsymbol{r}) , \\ f(\boldsymbol{r}) & \text{if } \left| f(\boldsymbol{r}) - \check{f}(\boldsymbol{r}) \right| \leq \varepsilon(\boldsymbol{r}) , \\ \check{f}(\boldsymbol{r}) + \varepsilon(\boldsymbol{r}) & \text{if } f(\boldsymbol{r}) - \check{f}(\boldsymbol{r}) > \varepsilon(\boldsymbol{r}) . \end{cases} \tag{4.66}$$

The reference image constraint $\mathsf{C}_{\check{f}}$ can be considered to be a generalization of C_{I} introduced previously for a minimum value $f_{\min}(\boldsymbol{r}) = \check{f}(\boldsymbol{r}) - \varepsilon(\boldsymbol{r})$ and a maximum value $f_{\max}(\boldsymbol{r}) = \check{f}(\boldsymbol{r}) + \varepsilon(\boldsymbol{r})$ that vary spatially.

The appropriate choice of $\varepsilon(\boldsymbol{r})$ is crucial for the successful application of reference images. If $\varepsilon(\boldsymbol{r})$ is too large, the space of possible solutions is not very much restricted. On the other hand, if $\varepsilon(\boldsymbol{r})$ is too small, the intersection of $\mathsf{C}_{\check{f}}$ with the other constraint sets may be empty, i.e., there may be no solution consistent with all constraints.

Chapter 5

Results

In this chapter, the results from various computer simulations and experiments on X-ray computed tomography (CT) using non-ideal projection data are presented. It is organized as follows.

Section 5.1 deals with the geometric calibration of cone-beam X-ray devices. It comprises comparisons of the parametric and non-parametric technique for estimating the projection geometry for each view introduced in subsection 4.4.3 and 4.4.4, respectively. Results of computer simulations concerning the efficacy of the decomposition algorithm described in subsection 4.1.4 are also presented. Furthermore, the evaluation of the reproducibility of flex effects is demonstrated for a linear accelerator.

In section 5.2, the image quality obtained with the approximate reconstruction algorithm from section 4.5 and the experimental cone-beam CT scanners introduced in subsection 4.2.2 is assessed. The performance of the flex correction, spatial resolution and various types of artefacts are considered.

Image restoration results from limited-angle projection data and prior knowledge about the object are presented in section 5.3. Various constraints are compared by means of computer simulations. The influence of noisy transmission data on the iterative restoration procedure is demonstrated. A clinical example of imaging a beating heart is also shown.

Section 5.4 comprises results of a phantom study on rigid-body registration of three-dimensional image data sets. These results indicate whether approximate cone-beam reconstruction can be considered a feasible basis for further image processing. Section 5.4, however, does not provide a comprehensive investigation of matching tools.

5.1 Geometric calibration

The geometric calibration methods and the decomposition algorithm introduced in subsections 4.4.3, 4.4.4 and 4.1.4, respectively, were investigated by means of computer simulations. The assessment of their efficacy given here refers only to geometric accuracy. The impact of the calibration on image quality is addressed in the following section. In addition to the computer simulations, the performance of the calibration technique was studied for cone-beam imaging using a linear accelerator.

5.1.1 Simulation and evaluation design

The computer simulations were carried out for the cone-beam geometry described in subsection 4.2.2. In this geometry, the distance from the source to the isocentre and the detector are 100 cm and 130 cm, respectively. The flat detector exhibits a sensitive area of $20.48 \times 20.48\,\mathrm{cm}^2$, and the pixel pitch equals 0.8 mm along its rows and columns.

A virtual calibration phantom similar to the real one introduced in subsection 4.4.1 was represented analytically. The virtual phantom comprises 30 ball bearings arranged along a helical trajectory with a radius of 6.75 cm. The length of the helix segment was chosen to be 14 cm to fit onto the virtual flat-panel detector in all views. The diameter of the ball bearings equals 3 mm, except for the central reference marker, which has a diameter of 4 mm.

A specific tolerance for the positions of the ball bearings within the calibration phantom was considered, as it is inevitable when a real calibration phantom is built. For this purpose, the positions were varied randomly according to a Gaussian distribution with zero mean and standard deviation $\sigma = 0.05$ mm. The distribution was truncated at $\pm 3\sigma$, since a particular level is not exceeded in reality.

The projections of the virtual calibration phantom were calculated using the formulae in section B.1, where 15×15 line integrals were averaged for each detector pixel. Photon statistics and beam hardening were not simulated. Dose considerations that might limit the signal-to-noise ratio in the projections do not play a role at all when the calibration is performed off-line. However, these effects are negligible even for dose-limited (online) calibration scans. Due to the high absorption of the steel ball bearings, their positions in the projections can be obtained with similar accuracy in all practical situations.

The *geometric accuracy* of the calibration procedure was assessed by comparing, for each view at angle α, the actual projection matrix $\boldsymbol{P}_{\alpha,\text{act}}$ obtained from a calibration scan with the reference matrix $\boldsymbol{P}_{\alpha,\text{ref}}$ utilized to simulate the corresponding projection. For this purpose, points $\boldsymbol{r} = (x, y, z)^{\mathrm{T}}$ in three-dimensional object space were reprojected onto the detector using equations (4.5), (4.6), and the corresponding deviations

$$\Delta s\left(\alpha, \boldsymbol{r}\right) = \sqrt{\left(u_{\text{act}}\left(\alpha, \boldsymbol{r}\right) - u_{\text{ref}}\left(\alpha, \boldsymbol{r}\right)\right)^2 + \left(v_{\text{act}}\left(\alpha, \boldsymbol{r}\right) - v_{\text{ref}}\left(\alpha, \boldsymbol{r}\right)\right)^2} \quad (5.1)$$

between actual and the reference values were calculated. To calculate the mean reprojection deviation, the results for 10,000 object points randomly distributed with the field of view were averaged for each projection, because a closed-form analytical integration is cumbersome to handle.

The *accuracy of attenuation coefficients* reconstructed by filtered backprojection depends strongly on the accuracy of the distance weighting factor $\lambda^{-2}\left(\alpha, \boldsymbol{r}\right) = R^2\left(\boldsymbol{r}\right)/L^2\left(\alpha, \boldsymbol{r}\right)$ in equation (4.44). This factor is also conveniently obtained from the projection matrix as shown in equation (4.28). The actual weighting factors calculated from an estimated projection matrix were compared to the corresponding reference values using the definition

$$\delta\lambda^{-2}\left(\alpha, \boldsymbol{r}\right) = \frac{\lambda_{\text{act}}^{-2}\left(\alpha, \boldsymbol{r}\right) - \lambda_{\text{ref}}^{-2}\left(\alpha, \boldsymbol{r}\right)}{\lambda_{\text{ref}}^{-2}\left(\alpha, \boldsymbol{r}\right)}\,. \quad (5.2)$$

The mean deviation was computed for 10,000 random object points per view as above.

5.1.2 Parametric versus non-parametric method

The parametric and non-parametric calibration methods were compared in terms of the reprojection deviation Δs using the simulation design explained in the previous subsection.

The parametric technique was found to rely strongly on sufficiently accurate, initial estimates of the geometric parameters. Otherwise, the iterative procedure frequently converged on a local minimum of the objective function that does not reflect the true projection geometry at all. For the simulation, the a priori known, geometric parameters were randomly varied according to a Gaussian distribution to serve as initial estimate. The corresponding standard deviation was 0.25 cm for the length parameters (x_{foc}, y_{foc}, z_{foc}, D, u_{foc}, v_{foc}), 0.5° for the angular parameters (ϕ, θ, ψ) and 10^{-4} for the scale coefficients (a_1, a_2) as defined in subsection 4.1.3. These values are reasonable assumptions of the accuracy that could be obtained in practical applications. The Gaussian distribution was truncated at two standard deviations because the initial estimates would not exceed a particular threshold in reality. The (analytical) non-parametric method, in contrast, does not require any initial estimates.

Figure 5.1 and figure 5.2 show the spatial distribution of the reprojection deviation Δs in terms of one-dimensional and two-dimensional cross-sections for the parametric and non-parametric calibration methods. This spatial distribution is, in general, highly non-uniform as can be seen in the two-dimensional contour plots in both figures. Its shape depends on the configuration of markers comprising the calibration phantom.

Using the parametric method, the reprojection deviation increases almost linearly with increasing distance from the isocentre along the x, y and z axes, as shown in the one-dimensional cross-sections. In contrast, using the non-parametric calibration technique, the deviation is less than 0.1 mm almost everywhere within the volume that is covered by the marker helix (indicated by the dashed-dotted lines in the plots), but increases dramatically outside this volume. A maximum deviation of 0.1 mm is sufficiently small compared to the detector pixel pitch of 0.8 mm. Altogether, the non-parametric method exhibits desirable features if the projections of the marker helix cover the sensitive area of the detector almost completely.

The parametric and non-parametric methods were compared rigorously by means of a statistical test. For both methods, the radial reprojection deviation Δs was computed in 120 views equally spaced over the full revolution. In each view, 10,000 test points randomly distributed within the field of view (FOV) were evaluated. The FOV is the volume covered by the (virtual) CT scan using equation (4.2), which is slightly larger than the volume covered by the marker helix. The number of points that exhibit a reprojection deviation less than a particular threshold was then determined. Using this measure, a χ^2 test at significance level 0.01 was performed for thresholds between 0.08 mm and 0.8 mm, i.e., between a tenth and one detector pixel pitch. In all of these cases, the number of points within the specified threshold was significantly larger for the non-parametric method than for the parametric method.

The results of the χ^2 test confirm the assessment of both calibration methods obtained by visual inspection of the reprojection maps in figure 5.1 and figure 5.2. They demonstrate clearly that the non-parametric calibration method is preferable in terms of geometric accuracy.

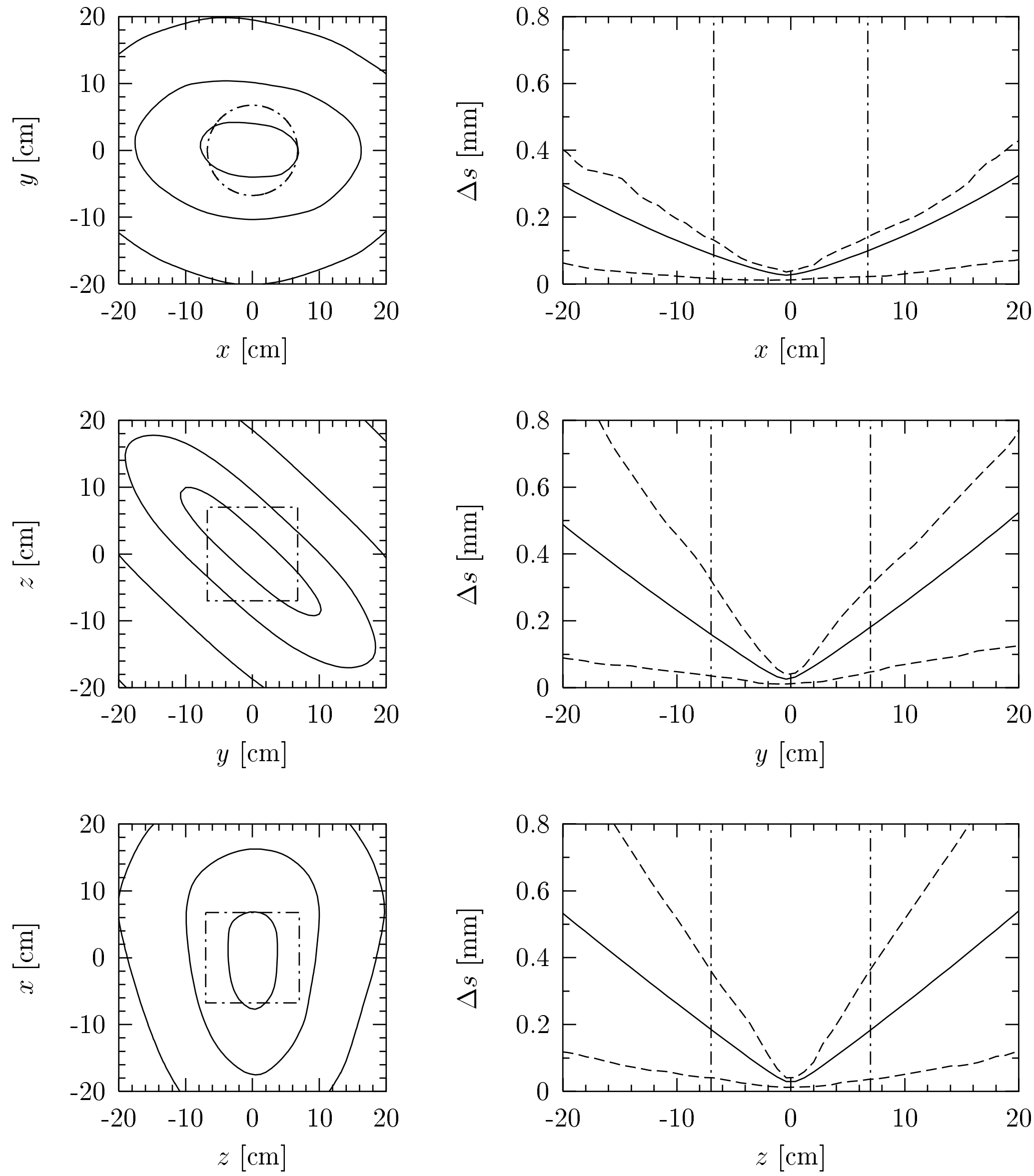

Figure 5.1: Accuracy of the parametric calibration method in terms of the spatial distribution of the radial reprojection deviation Δs [mm] averaged over 120 equiangular views. The diagrams are plotted for a calibration phantom with $N = 30$ markers and a tolerance level of $\sigma = 0.05\,\text{mm}$. The detector pixel pitch along both axes is $u_{\text{pitch}} = v_{\text{pitch}} = 0.8\,\text{mm}$. The dashed-dotted lines indicate the outline of the helix phantom. The contour lines in the two-dimensional plot visualize the levels $\Delta s = 0.1\,\text{mm}, 0.25\,\text{mm}, 0.5\,\text{mm}$, from centre to periphery. The dashed lines in the one-dimensional cross-sections along the coordinate axes refer to the single standard deviation of Δs with respect to all view angles of a full scan.

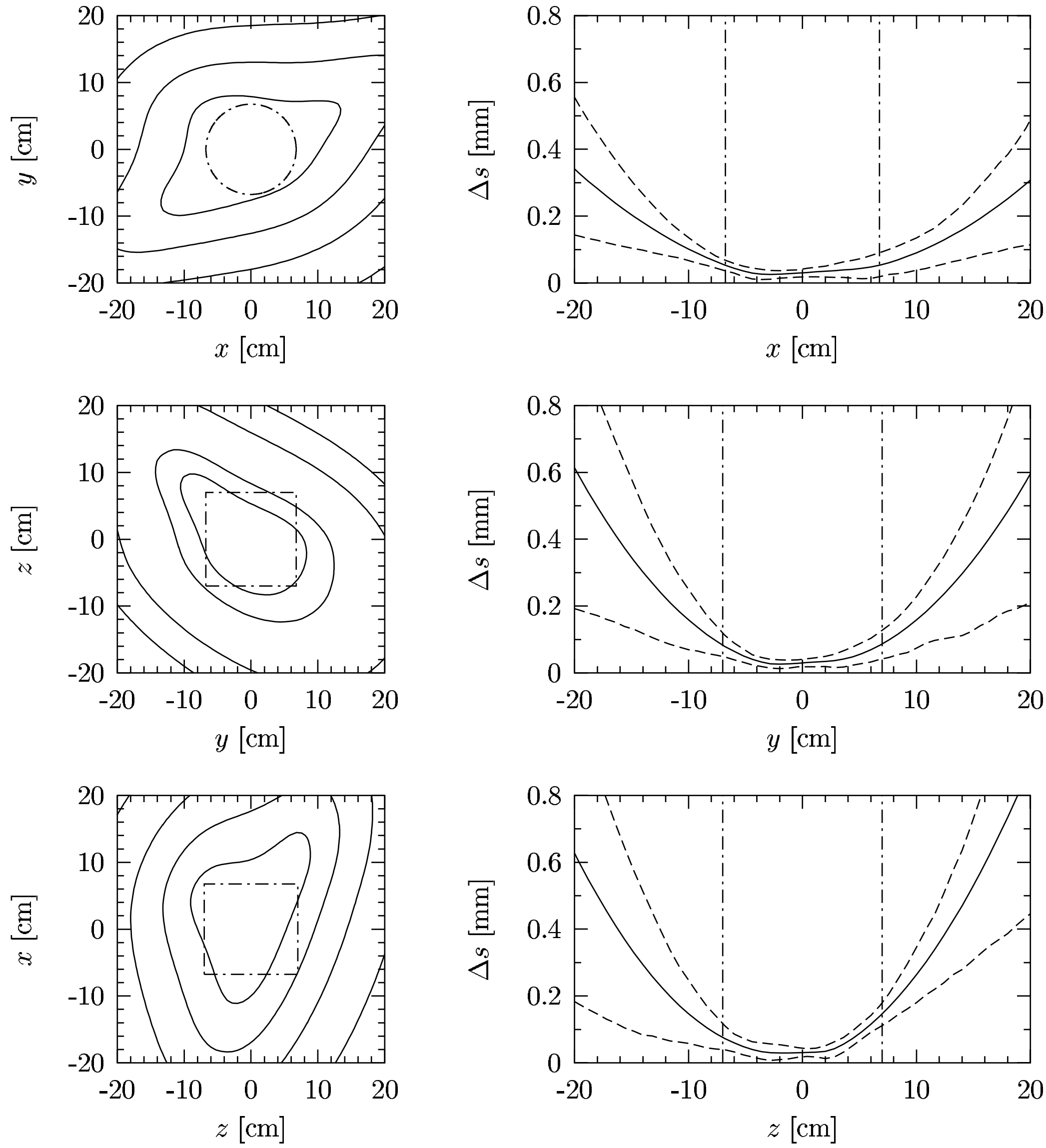

Figure 5.2: Accuracy of the non-parametric calibration method in terms of the spatial distribution of the radial reprojection deviation Δs [mm] averaged over 120 equiangular views. The diagrams are plotted for a calibration phantom with $N = 30$ markers and a tolerance level of $\sigma = 0.05\,\text{mm}$. The detector pixel pitch along both axes is $u_{\text{pitch}} = v_{\text{pitch}} = 0.8\,\text{mm}$. The dashed-dotted lines indicate the outline of the helix phantom. The contour lines in the two-dimensional plot visualize the levels $\Delta s = 0.1\,\text{mm}, 0.25\,\text{mm}, 0.5\,\text{mm}, 1.0\,\text{mm}$, from centre to periphery. The dashed lines in the one-dimensional cross-sections along the coordinate axes refer to the single standard deviation of Δs with respect to all view angles of a full scan.

5.1.3 Sensitivity analysis

The sensitivity of the calibration methods were investigated with respect to the number N of markers comprising the calibration phantom, the tolerance level σ and the detector pixel pitch $u_{\text{pitch}}, v_{\text{pitch}}$. These parameters can be expected to have an influence on the uncertainties remaining after geometric calibration. The default values introduced in subsection 5.1.1 were varied independently from each other in successive simulations.

The results of this analysis are presented in detail for the non-parametric technique, since this is preferable in terms of geometric accuracy as known from the previous subsection. At the end of this subsection, however, the results for the parametric calibration method are mentioned briefly.

Figure 5.3 shows the mean reprojection deviation for randomly distributed test points remaining after non-parametric calibration as function of the number of markers. These values were calculated for an ideal calibration phantom, i.e., for the tolerance level $\sigma = 0\,\text{mm}$. The detector pixel pitch was $u_{\text{pitch}} = v_{\text{pitch}} = 0.8\,\text{mm}$ as before. The mean value and the standard deviation of the Δs drops significantly between 6 (the theoretical minimum) and 18 markers. No further improvement is observed for $N > 18$. The mean reprojection deviation oscillates then slightly with an increasing number of markers.

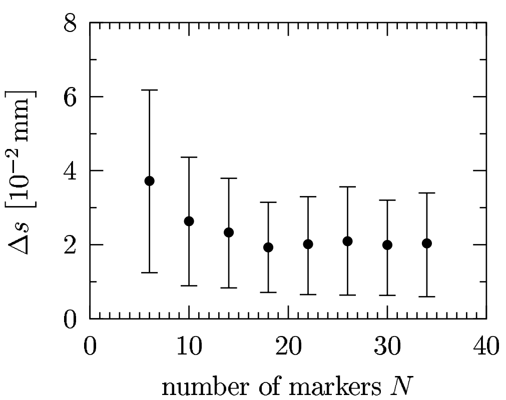

Figure 5.3: Mean reprojection deviation Δs of randomly distributed test points remaining after non-parametric calibration as function of the number N of markers for $\sigma = 0\,\text{mm}$ and $u_{\text{pitch}} = v_{\text{pitch}} = 0.8\,\text{mm}$.

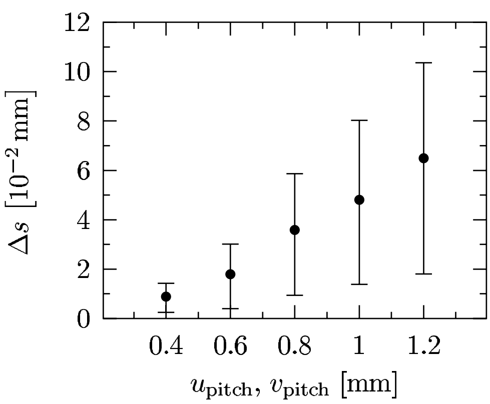

Figure 5.4: Mean reprojection deviation Δs of randomly distributed test points remaining after non-parametric calibration as function of the detector pixel pitch u_{pitch}, v_{pitch} for $N = 30$ markers and $\sigma = 0\,\text{mm}$.

Figure 5.4 shows the mean reprojection deviation of random test points for the non-parametric calibration method and data sets simulated at various detector pixel pitch values u_{pitch}, v_{pitch}. For this simulation, a phantom with $N = 30$ markers and $\sigma = 0\,\text{mm}$ was employed. For pitches between 0.6 mm and 1.2 mm, the geometric accuracy decreases almost linearly with increasing pitch. The pixel pitch is relevant for the first step of the calibration algorithm, in which the positions of the ball bearings in the projections are estimated by calculating their centre of gravity. It is obvious that the accuracy of this step is determined by the ratio between the size of the markers (which was kept constant in the simulation) and the size of the detector pixels. In practice, the size of the ball bearings could be increased (as far as possible) in order to improve the accuracy for a given detector.

The reprojection deviations remaining after non-parametric calibration are plotted for different tolerance levels σ in figure 5.5. These values were calculated for a phantom with $N = 30$ markers and a detector pixel pith of $u_{\text{pitch}} = v_{\text{pitch}} = 0.8\,\text{mm}$. The diagram shows that there is no significant difference in geometric accuracy up to a tolerance level of 0.01 mm. The accuracy for $\sigma = 0.05\,\text{mm}$ can still be considered acceptable. This simulation result suggests therefore a maximum tolerance of $3\sigma = 0.15\,\text{mm}$ (or preferably a little bit less than that) when a real calibration phantom is to be built. Of course, this consideration is strictly true only for the particular cone-beam geometry employed in this simulation.

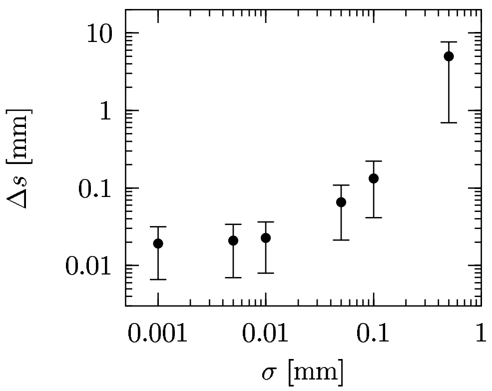

Figure 5.5: Mean reprojection deviation Δs of randomly distributed test points remaining after non-parametric calibration as function of the tolerance level σ for $N = 30$ markers and $u_{\text{pitch}} = v_{\text{pitch}} = 0.8\,\text{mm}$.

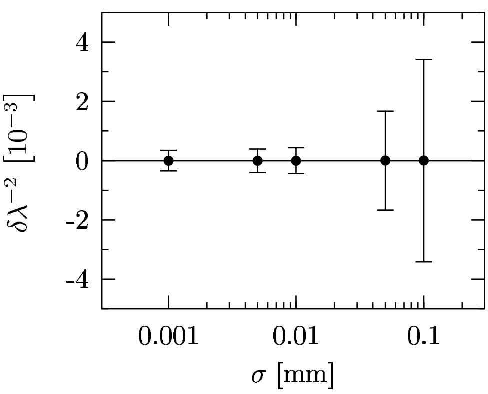

Figure 5.6: Mean relative deviation $\delta\lambda^{-2}$ of the backprojection weighting factor remaining after non-parametric calibration as function of the tolerance level σ for $N = 30$ markers and $u_{\text{pitch}} = v_{\text{pitch}} = 0.8\,\text{mm}$.

For the parametric calibration method, the mean radial reprojection deviation Δs remains larger than 0.1 mm for $N \leq 30$ markers, $\sigma = 0$ mm and $u_{\text{pitch}} = v_{\text{pitch}} = 0.8$ mm. This is about a factor of 5 worse than corresponding values for the non-parametric calibration method. For the parametric method, the reprojection uncertainty drops only for a large number of markers. The parametric calibration method is, in relative terms, less sensitive to changes in the tolerance level σ and the detector pixel pitch u_{pitch}, v_{pitch} than the non-parametric technique. For all parameter combinations that were investigated, however, the mean radial reprojection deviation Δs is significantly larger for the parametric technique than for the non-parametric technique.

The uncertainty of the weighting factor $\lambda^{-2}(\alpha, \boldsymbol{r}) = R^2(\alpha)/L^2(\alpha, \boldsymbol{r})$ was studied only for the parametric method. Its sensitivity was investigated for the same sets of parameters as utilized above. Varying the number N of markers and the detector pixel pitch u_{pitch}, v_{pitch} within the ranges shown in figure 5.3 and figure 5.4, the mean relative deviation $\delta\lambda^{-2}$ remains in the interval $\pm 10^{-3}$. It depends, however, significantly on the tolerance level σ as shown in figure 5.6. Although the correct mean value averaged over all random object points is maintained for a large range of σ, the corresponding standard deviation increases dramatically for $\sigma > 0.01$ mm. From this point of view, the tolerance level should be definitely less than $3\sigma = 0.1$ mm for a real calibration phantom.

5.1.4 Accuracy of geometric parameters

In the previous subsections, the calibration methods were compared based on the projection matrices delivered. Geometric parameters describing arbitrary linear cone-beam projections can be estimated from a calibration scan either by using the parametric method or by using the non-parametric method with successive decomposition of the projection matrices. These approaches were investigated for different tolerance levels σ, a calibration phantom with $N = 30$ markers and a detector pixel pitch of $u_{\text{pitch}} = v_{\text{pitch}} = 0.8$ mm.

The results for the parametric method are presented in table 5.1. They indicate that the accuracy does not significantly depend on the phantom tolerance σ, provided σ is kept in a reasonable (realistic) range. The accuracy with which the parameters can be obtained, however, is generally limited. This is particularly true for the source-to-detector distance D and the coordinates of the view reference point u_{foc}, v_{foc}.

Parameter		$\Delta\,(\sigma = 0\,\text{mm})$	$\Delta\,(\sigma = 0.05\,\text{mm})$	$\Delta\,(\sigma = 0.1\,\text{mm})$
x_{foc}	[cm]	-0.1398 ± 0.9751	-0.0851 ± 0.7269	-0.2341 ± 0.9207
y_{foc}	[cm]	-0.0121 ± 0.2740	-0.0113 ± 0.5587	0.0163 ± 0.4597
z_{foc}	[cm]	-0.0202 ± 0.3321	0.0164 ± 0.2117	0.0063 ± 0.2308
ϕ	[deg]	0.0289 ± 0.1782	-0.0071 ± 0.1601	-0.0246 ± 0.1726
θ	[deg]	0.0229 ± 0.1200	0.0038 ± 0.1486	0.0149 ± 0.1465
ψ	[deg]	-0.0002 ± 0.0768	0.0012 ± 0.0476	-0.0051 ± 0.0594
D	[cm]	0.0944 ± 1.3522	0.0573 ± 1.2051	-0.0917 ± 1.3719
a_1	$[10^{-3}]$	-0.0362 ± 1.6703	-0.2618 ± 1.0120	-0.4574 ± 1.1574
a_2	$[10^{-3}]$	0.0128 ± 1.3889	-0.0123 ± 1.0298	0.1318 ± 1.1758
u_{foc}	[cm]	-0.0194 ± 0.2559	-0.0398 ± 0.3001	-0.0363 ± 0.3177
v_{foc}	[cm]	0.0263 ± 0.2685	0.0304 ± 0.2662	0.0429 ± 0.2540

Table 5.1: Accuracy of the parametric calibration method. The geometric parameters listed in the left column are defined in subsection 4.1.3. The deviation Δ of these parameters from the a priori known values are given in terms of mean and single standard deviation for a full scan comprising 120 views. The simulation results are provided for a calibration phantom with $N = 30$ markers and different tolerance levels σ. The detector pixel pitch is $u_{\text{pitch}} = v_{\text{pitch}} = 0.8\,\text{mm}$.

Parameter		$\Delta\,(\sigma = 0\,\text{mm})$	$\Delta\,(\sigma = 0.05\,\text{mm})$	$\Delta\,(\sigma = 0.1\,\text{mm})$
x_{foc}	[cm]	0.0047 ± 0.1302	-0.2891 ± 0.7798	-0.5545 ± 1.5930
y_{foc}	[cm]	-0.0077 ± 0.1128	0.8127 ± 0.5886	1.6130 ± 1.1827
z_{foc}	[cm]	0.0033 ± 0.0160	0.0028 ± 0.0433	0.0032 ± 0.0837
ϕ	[deg]	0.0099 ± 0.0972	0.0083 ± 0.7323	-0.0029 ± 1.4451
θ	[deg]	-0.0350 ± 0.3109	0.8028 ± 0.4887	1.6931 ± 0.9429
ψ	[deg]	-0.0009 ± 0.0069	0.0015 ± 0.0121	0.0083 ± 0.0261
D	[cm]	-0.0123 ± 0.2235	-0.3125 ± 1.6852	-1.1279 ± 3.3078
a_1	$[10^{-3}]$	-0.0127 ± 0.1136	-0.3578 ± 0.1450	-0.7943 ± 0.3522
a_2	$[10^{-3}]$	0.0419 ± 0.2146	0.0037 ± 0.4889	-0.0337 ± 1.2160
u_{foc}	[cm]	-0.0242 ± 0.2257	-0.0148 ± 1.6572	0.0260 ± 3.2454
v_{foc}	[cm]	-0.0751 ± 0.7094	1.8196 ± 1.1120	3.7996 ± 2.1274

Table 5.2: Accuracy of the algorithm for the decomposition of projection matrices. The geometric parameters listed in the left column are defined in subsection 4.1.3. The deviation Δ of these parameters from the a priori known values are given in terms of mean and single standard deviation for a full scan comprising 120 views. The simulation results are provided for a calibration phantom with $N = 30$ markers and different tolerance levels σ. The detector pixel pitch is $u_{\text{pitch}} = v_{\text{pitch}} = 0.8\,\text{mm}$.

Table 5.2 summarizes the results for the analytical decomposition algorithm. This method works well for $\sigma = 0\,\mathrm{mm}$, i.e., for an ideal calibration phantom. In this case, the discretization of the projections is considered to be the only source of uncertainties. For non-zero tolerance levels σ, however, the accuracy of the method decreases significantly with increasing σ. The source-to-detector distance D, the Euler angle θ and the coordinates u_{foc}, v_{foc} of the view reference point are most affected by these numerical problems.

A comparison of table 5.1 and table 5.2 shows that the non-parametric method with successive decomposition of the projection matrix performs better than the parametric technique for $\sigma = 0\,\mathrm{mm}$. For realistic tolerance levels, however, the parametric method performs better, especially for u_{foc} and v_{foc}, although it delivers generally less accurate projection matrices as shown before.

The source-to-isocentre distance R and the view angle α can be obtained from the above set of parameters, provided the coordinates of the isocentre are known a priori. This can be achieved by aligning the calibration phantom using laser marks, for example. Figure 5.7 shows the mean deviation of the source-to-isocentre distance ΔR and the mean deviation of the view angle $\Delta\alpha$ as function of the phantom tolerance level σ. These values were calculated by means of the non-parametric calibration with successive decomposition. The results indicate that the view angle can be accurately determined from the corresponding projection matrix, even for large tolerance levels. This is of particular interest for continuous gantry rotations with varying velocity if no angle sensor is available (provided the variations are reproducible).

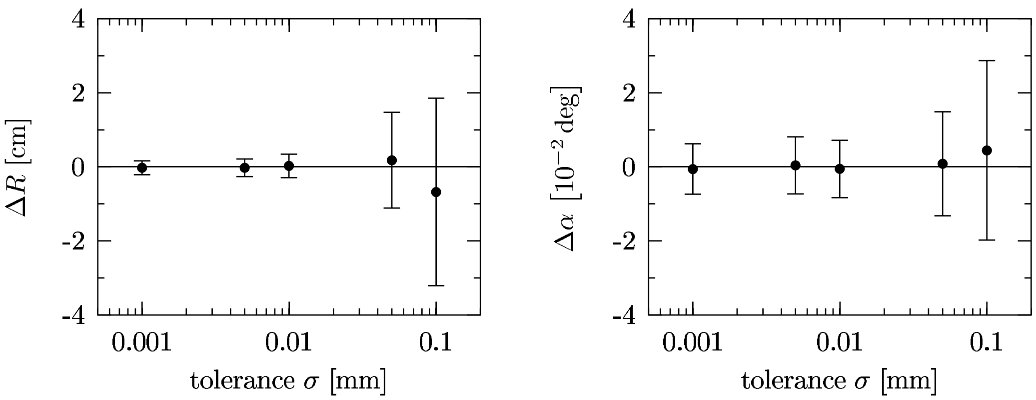

Figure 5.7: Mean deviation of the source-to-isocentre distance ΔR (left diagram) and mean deviation of the view angle $\Delta\alpha$ (right diagram) as function of the tolerance σ for $N = 30$ markers and $u_{\mathrm{pitch}} = v_{\mathrm{pitch}} = 0.8\,\mathrm{mm}$.

5.1.5 Reproducibility measurements

The reproducibility of mechanical flex effects was investigated for the cone-beam system employing a linear accelerator as described in subsection 4.2.2. A careful analysis of repeatability is important in order to decide if an off-line calibration is sufficient or whether an online calibration is required.

Various scans were compared in terms of the reprojection deviation Δs for test points randomly distributed within the field of view such as introduced in subsection 5.1.1. This allows an appropriate evaluation of the impact the flex effects have on backprojection and reprojection algorithms. The difference between these measurements and the computer simulation described previously is simply that two (or more) actual scans are compared rather than an actual scan with a (theoretical) reference scan.

Ten full scans of the helix phantom were acquired in step-and-shoot fashion in view angle steps of 45°. The rotation direction of the gantry was reversed after each scan, i.e., the first scan was taken from $-180°$ to $+180°$, the second one from $+180°$ to $-180°$, the third one again from $-180°$ to $+180°$ and so forth. The reprojection deviations of 10,000 test points randomly distributed within the field of view were compared for each view independently.

Figure 5.8 shows the results of this investigation. In the axial direction along the detector columns, the reprojection deviation is always smaller than a tenth of the detector pixel pitch, even when the rotation direction of the gantry is changed. In the lateral direction along the detector rows, however, the deviation reaches up to half the detector pixel pitch in some views. This effect is probably mainly due to the uncertainty in selecting the gantry angle. Changing the rotation direction, lateral reprojection differences up to 3 mm are observed. These large deviations are clearly not caused by the gantry itself. This can be concluded from the geometric set-up and from the fact that the uncertainty of gantry angle selection[1] is definitely less than 1°.

The above considerations were confirmed by another experiment. The flat-panel imager was kept fixed at 0°, where the largest deviation occurred, instead of attaching it to the gantry. The gantry was rotated using the same steps as before in order to be able to compare the result to the previous ones. The projection images of the calibration phantom, however, were only acquired at $\alpha = 0°$.

[1]The control software allows the choose the gantry angle in steps of 1°and displays the actual gantry angle with an accuracy of 0.1°. The exact tolerance due to the technical specification is unfortunately unknown.

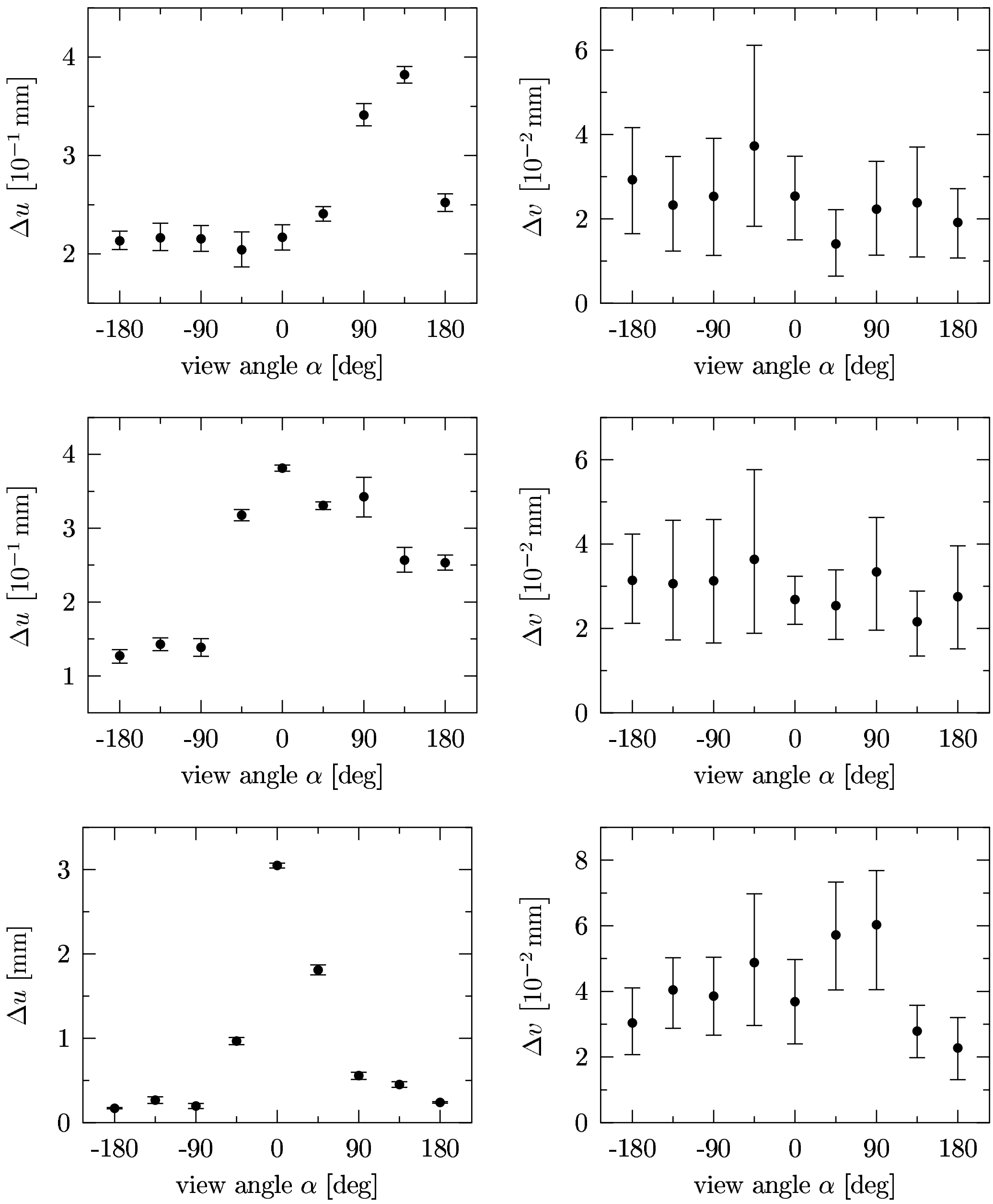

Figure 5.8: Reproducibility of flex effects of a linear accelerator. The reprojection deviation along the detector rows (left diagrams) and along the detector columns (right diagrams) is plotted as a function of the view angle. The values are plotted in terms of the standard deviation between 5 scans taken in clockwise direction (top), 5 scans taken in anticlockwise direction (middle) and between all of these scans (bottom). The error bars refer to the standard deviation of 10,000 random test points per view.

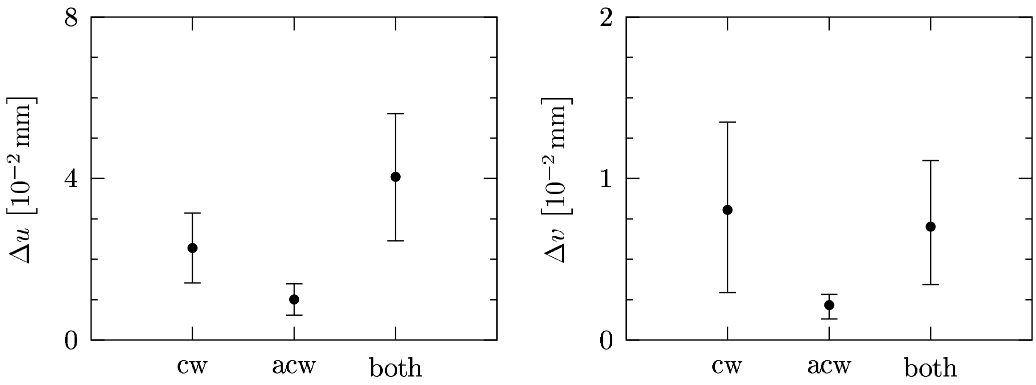

Figure 5.9: Gantry positioning uncertainty of a linear accelerator measured at a view angle of $\alpha = 0°$ with fixed detector. The reprojection deviation along the detector rows (left diagram) and along the detector columns (right diagram) is plotted for a series of clockwise (cw) scans, a series of anticlockwise (acw) scans and the combination of these (both).

The results of this experiment are depicted in figure 5.9. In lateral direction, the reprojection deviation is less than 0.08 mm for all acquisition modes (clockwise, anticlockwise and both). In axial direction, the differences are even less than 0.02 mm. The smallest uncertainties occur when the gantry is rotated anticlockwise. There is, however, no significant difference between rotating the gantry in only one or in both directions as observed in the previous experiment. In summary, the results show clearly that the positioning tolerance of the gantry is about one order of magnitude smaller than the uncertainties caused by the mechanical detector support frame.

In continuous gantry rotation mode, five full scans were acquired in clockwise direction, each of them comprising about 316 views. The mean angular spacing of the views was consequently about 1.14°. 200 MU were delivered per scan at an output rate of 167 MU min^{-1}. The detector integration time was 100 ms. The reprojection deviation of 10,000 test points randomly distributed within the field of view was compared between these scans such as in the step-and-shoot mode. The scans could not be started synchronously because a gating option was not available. The view angles were therefore calculated from the projection matrices using equation (4.29). To compare the results for a specific view angle, the nearest one was chosen.

Figure 5.10 shows the results of this experiment. The mean reprojection deviation along the detector rows is comparable to the values obtained in step-and-shoot mode. For view angles above +60°, however, the repeatability drops significantly. The reprojection deviation along the detector columns

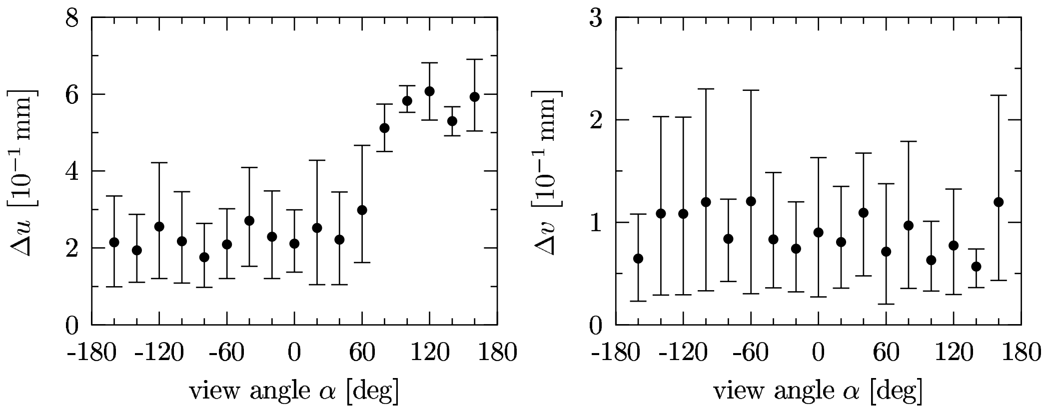

Figure 5.10: Reproducibility of flex effects of a linear accelerator in continuous gantry rotation mode. The reprojection deviation along the detector rows (left diagram) and along the detector columns (right diagram) is plotted as a function of the view angle. The values are plotted in terms of the standard deviation between 5 scans taken in clockwise direction. The error bars refer to the standard deviation for 10,000 random test points per view.

does not depend on the view angle, but is about a factor of 3 larger than for the step-and-shoot acquisition. This is a preliminary result due to the limitation that projections with maximum difference in view angle of almost 0.6° had to be compared. The experiment should be repeated when a gating option is available. The reproducibility is expected to be much better if the scans are started synchronously.

5.2 Image reconstruction

In this section, the performance of cone-beam reconstruction using the modified Feldkamp algorithm [24] introduced in section 4.5 is assessed. The X-ray transmission data were recorded by the experimental scanners described in subsection 4.2.2 and preprocessed such as explained in section 4.3.

The results obtained with these systems and algorithms in terms of flex correction, spatial resolution and artefacts are presented in the following subsections. After CT reconstruction, none of the images present here is processed further, except for the application of an appropriate grey-scale window for maximizing visual contrast. Although some postprocessing might improve image quality for specific applications, the aim of this section this to demonstrate the efficiency of pure cone-beam reconstruction.

5.2.1 Correction of flex effects

The effect of geometric flex effects occurring during projection data acquisition was assessed qualitatively for various data sets. The cone-beam data sets were recorded using a flat-panel imager attached to a linear accelerator and a therapy simulator, respectively, as explained in subsection 4.2.2. In this subsection, the results for non-calibrated and calibrated reconstructions are compared.

Figure 5.11 shows reconstructions of the helix phantom employed for geometric calibration. The non-calibrated reconstruction assuming an ideal single-circular source trajectory yields blurred images, which is particularly obvious looking at the ball bearings. The blurring is completely eliminated by the geometric calibration procedure.

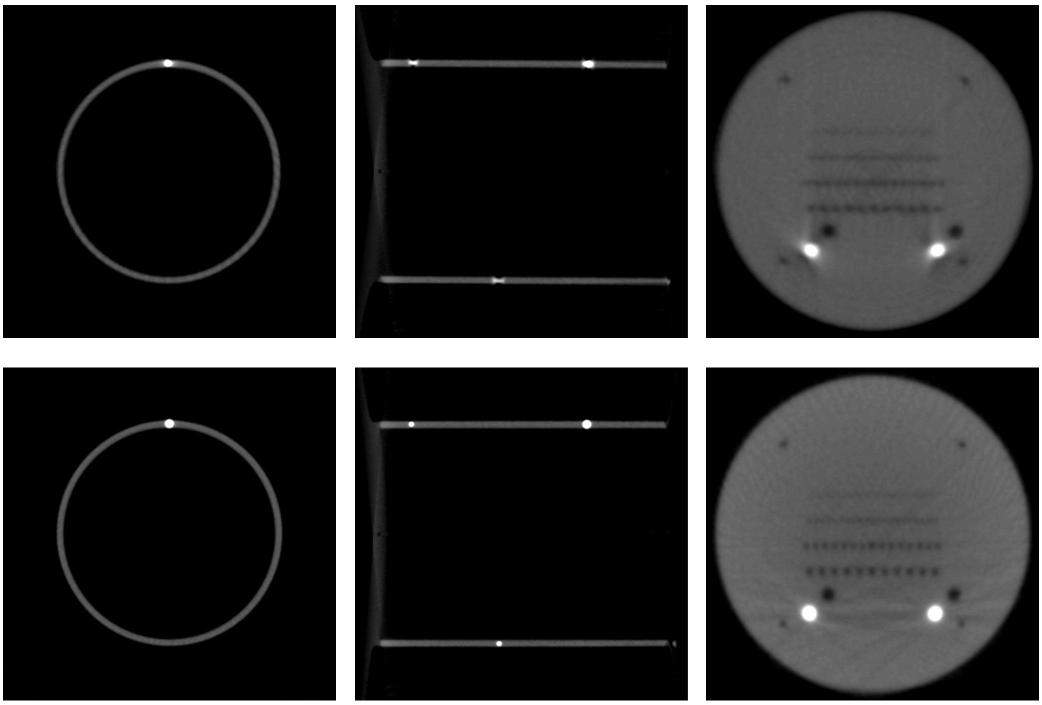

Figure 5.11: Performance of online geometric calibration. The figure shows transverse (left column) and sagittal (middle column) slices of the helix phantom used for geometric calibration and transverse slices of a disc directly attached to the top of the phantom (right column). The cone-beam projections were acquired using a linear accelerator. The non-calibrated reconstruction assuming an ideal single-circular source trajectory yields blurred images (top row), which is completely eliminated by the calibration procedure (bottom row).

This experiment demonstrates the best possible performance of the method for real data using an online calibration, since the calibration phantom itself is reconstructed. Figure 5.11 shows also transverse slices of a disc directly attached to the end of the phantom. Although the image quality is generally limited in this case due to the relatively large cone angle γ of about 5.7° (at the centre of the slice), the effect of the calibration is clearly visible.

CT images of a Rando Alderson head phantom are shown in figure 5.12 in order to demonstrate the performance of an off-line calibration. The projections were acquired using a radiotherapy simulator at an angular sampling pitch of 1°. The blurring caused by mechanical instabilities of the gantry is greatly reduced by applying the calibration procedure off-line. This observation suggests that the therapy simulator behaves quite reproducibly. A rigorous analysis of the reproducibility, however, is not presented here.

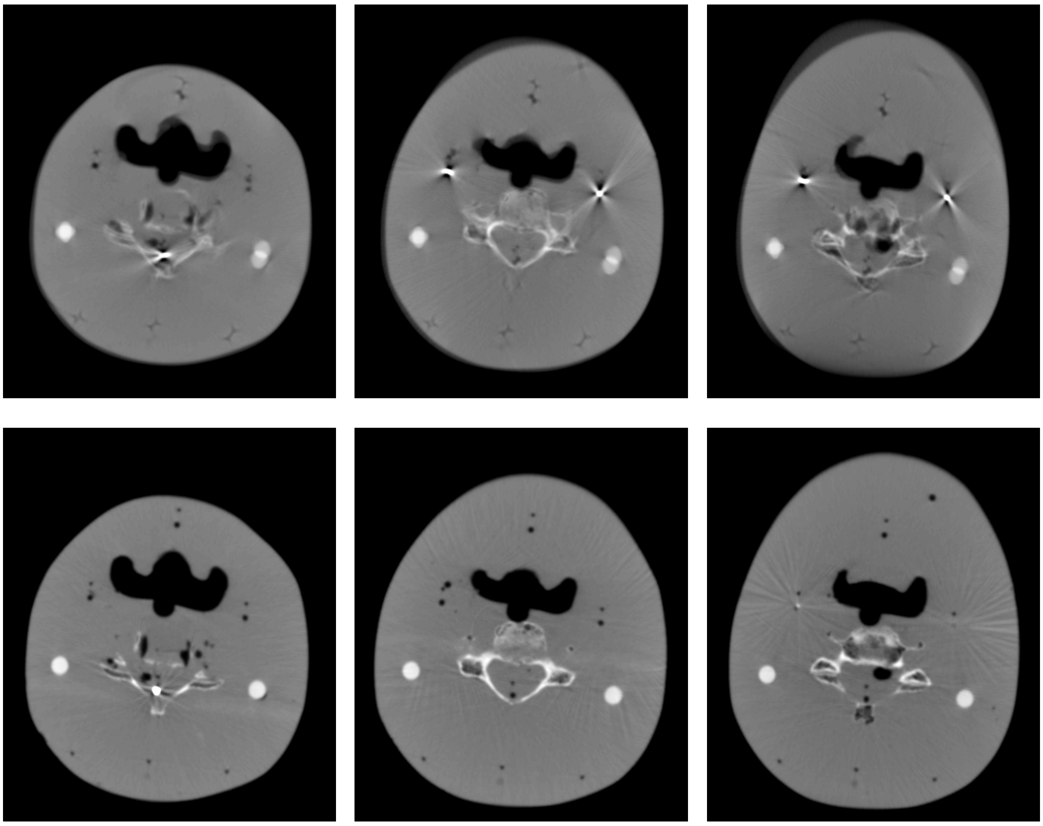

Figure 5.12: Performance of off-line geometric calibration. The figure shows transverse images of a Rando Alderson head phantom reconstructed without (top row) and with geometric calibration (bottom row). The projections were acquired using a therapy simulator.

5.2.2 Spatial resolution

The spatial resolution of the kilovoltage and megavoltage cone-beam CT systems described in subsection 4.2.2 was measured using a Perspex disc containing rows of holes of various diameters. For each row, the spacing of the holes is twice their diameter. The disc was placed at an axial distance of 7 cm from the mid-plane, which corresponds to a cone angle γ of about 4° (at the centre of the disc).

Reconstructions of the phantom were carried out using the modified Feldkamp algorithm [24] described in subsection 4.5.1 and the Shepp-Logan filter kernel [109]. The pixel size of the transverse slices was $0.3 \times 0.3\,\mathrm{mm}^2$, which is clearly below the resolution limit that can be expected for the cone-beam scanners investigated here. The slice thickness was 1.5 mm.

The results of the measurements are shown in figure 5.13. Visual inspection of the images suggests that the spatial resolution for high-contrast objects is between 1.3 mm and 1.6 mm for the megavoltage scanner and between 1.0 mm and 1.3 mm for the kilovoltage scanner. Using these experimental cone-beam scanners, the size of the focal spot is the most important factor limiting spatial resolution. For the linear accelerator, the full width at half maximum (FWHM) is about 1.2 mm. The focus of the therapy simulator is also significantly larger than in diagnostic CT scanners.

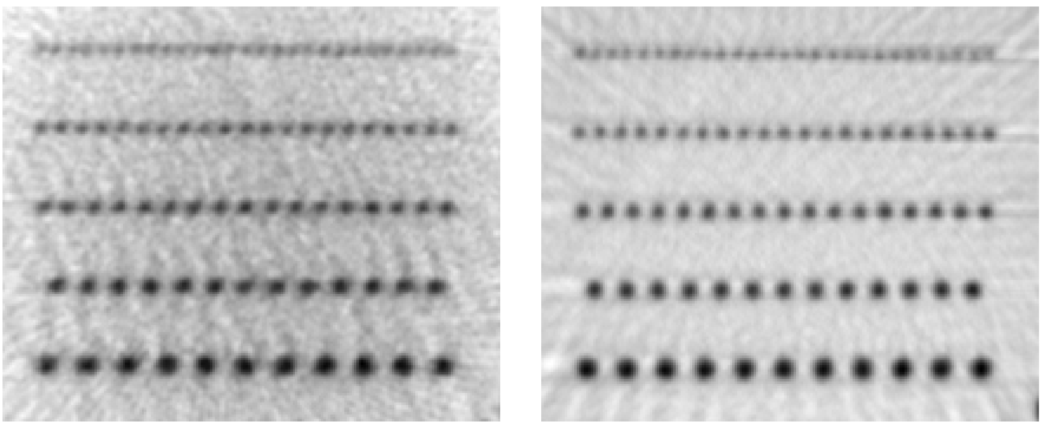

Figure 5.13: Reconstruction of a Perspex disc to measure spatial resolution for high-contrast objects. The diameters of the drill holes in each row are 1.0 mm, 1.3 mm, 1.6 mm, 2.0 mm and 2.5 mm (from top to bottom). The spacing of the holes is twice their diameter. The projections were recorded using a linear accelerator (left) and a therapy simulator (right image).

5.2.3 Assessment of artefacts

Figure 5.14 shows a transverse, a frontal and a sagittal CT image of a Rando Alderson head phantom. The voxel size for the reconstruction volume was $1.0 \times 1.0 \times 1.0\,\mathrm{mm}^3$. The X-ray transmission data were recorded using a linear accelerator and a video-based detector comprising 512×512 pixels at a pitch of 0.6 mm in each direction. The detector was placed at a distance of 117.8 cm from the focus. The CT scan did not require a geometric calibration because the phantom was rotated on a turn-table instead of the gantry. This experimental set-up was chosen because the flat-panel imager employed for the other investigations is too small to capture projections of the whole head phantom without lateral truncation.

The CT images depicted in figure 5.14 suffer from streak-shaped artefacts caused by the angular under-sampling. The same type of artefact can be observed in figure 5.13 for kilovoltage and megavoltage tomograms at about three times higher resolution. Comparing these images reconstructed from only 120 projections to those in the bottom row of figure 5.12 reconstructed from 360 projections, the benefit of using more projections is obvious. Using 120 projections, the peak-to-peak artefact level reaches up to 10 % from the local mean, whereas it is about 4 % for 360 projections.

The streak artefacts that show up particularly in the right column of figure 5.12 are caused by beam hardening due to small metal pieces embedded in the phantom. The assessment of beam-hardening effects, however, is beyond the scope of this thesis.

The frontal and sagittal slices in figure 5.11 and figure 5.14 exhibit typical artefacts due to axial truncation of the projections. These artefacts can be

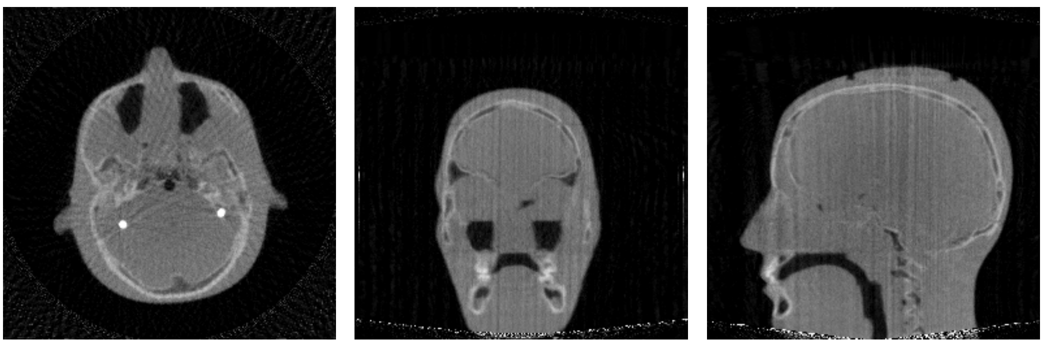

Figure 5.14: Transverse, frontal and sagittal megavoltage CT image of a Rando Alderson head phantom (from left to right).

considered relatively mild. They do not require any correction attempts if the region of interest is close to the centre of the field of view.

The distortions due to the incompleteness of cone-beam projections acquired in a single-circular scan are not directly visible in figure 5.14. They are obvious in the transverse image of the resolution disc depicted in figure 5.11, which corresponds to a cone angle γ of about $5.7°$. At moderate cone angles up to $\pm 4°$, single-circular scans yield images that are sufficient for most medical applications. In this range, the well-known intensity drop in axial direction is less than $1.5\,\%$ for the cone-beam geometry considered here.

5.3 Image restoration

This section deals with image restoration from limited-angle projections using the method of *projections onto convex sets* (POCS) introduced in section 4.6 and section A.4. Various constraints modelling prior knowledge about the object are compared using computer simulations of the Shepp-Logan phantom [49]. The performance of iterative image restoration on noisy data is characterized for a simple phantom comprising realistic attenuation values. The methods are also applied to a clinical example of ECG-correlated imaging of a beating heart. No postprocessing was applied to the images shown below in order to demonstrate the efficiency of the pure algorithms.

5.3.1 Comparison of constraints

Images of the two-dimensional Shepp-Logan phantom such as defined in section B.3 were restored by various iterative schemes in order to assess the performance of the corresponding constraints. Fan-beam projections were calculated analytically as described in section B.1. The views were sampled in increments of $0.5°$, each of them comprising 512 bins at a pitch of 0.0085 (lengths and attenuation coefficients are given in arbitrary units according to the definition of the phantom). The focus-to-isocentre distance was 6.0, and the virtual flat detector was placed at a distance of 9.0 from the focus.

The images were restored on a grid of 512×512 pixels at a spacing of 0.0038 in each direction. The grey-scale window is $[0.95, 1.05]$ in all figures shown below, i.e., the attenuation coefficients between 0.95 and 1.05 are scaled linearly to the grey levels available between black and white.

Figure 5.15 depicts images of the Shepp-Logan phantom obtained by standard filtered backprojection from limited ranges of view angles between 60° and 120°. These images are included for comparison with the results from restoration algorithms considered below.

The left image shown in figure 5.16 was obtained after 10 iterations of the *Gerchberg-Papoulis algorithm* [27, 84], which reads as

$$f^{(t+1)}(\boldsymbol{r}) = \mathcal{C}_\Omega\, \mathcal{C}_\mathsf{F}\, f^{(t)}(\boldsymbol{r}) \tag{5.3}$$

in the notation of section 4.6. In the above equation, $\mathcal{C}_\mathsf{F}$ enforces consistency of the image $f(\boldsymbol{r})$ with the part F of its Fourier spectrum that is known from the measured projections at view angles between 0° and 120°. This constraint operator was implemented by reprojection of the missing line integrals and filtered backprojection of the short-scan data set. The constraint operator $\mathcal{C}_\Omega$ restricting the image to finite spatial extent was considered implicitly, i.e., the region Ω was assumed to be the entire rectangular reconstruction area. The first iteration of this scheme is therefore equivalent to standard filtered backprojection.

The middle image in figure 5.16 shows the result from restricting the attenuation coefficients to the interval $\mathrm{I} = [0.0, 3.0]$ in addition to the above constraints,

$$f^{(t+1)}(\boldsymbol{r}) = \mathcal{C}_\mathrm{I}\, \mathcal{C}_\Omega\, \mathcal{C}_\mathsf{F}\, f^{(t)}(\boldsymbol{r}) \; . \tag{5.4}$$

A reference image $\check{f}(\boldsymbol{r})$ comprising only the two outer ellipsoids of the Shepp-Logan phantom was then introduced into the iterative procedure. The allowed distance from this reference image was chosen spatially constant as $\varepsilon(\boldsymbol{r}) = 0.3$. In this particular case, the constraint C_I is completely contained

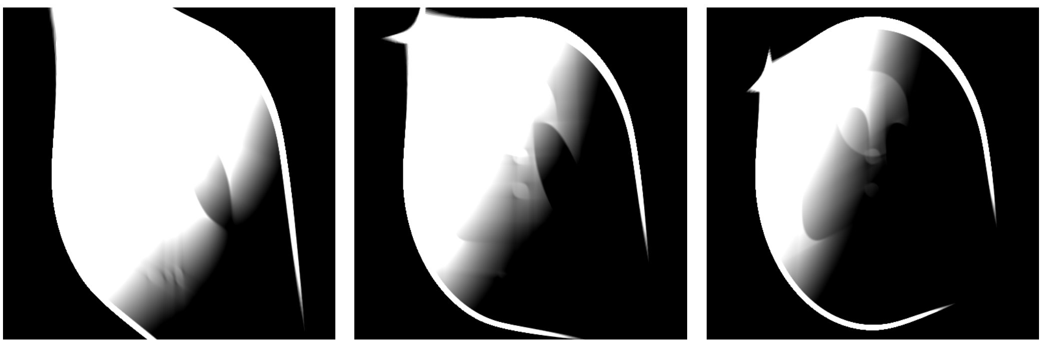

Figure 5.15: Images of the Shepp-Logan phantom reconstructed from fan-beam projections for view angle ranges of 60°, 90° and 120° (from left to right).

in $\mathrm{C}_{\check{f}}$. The image restored by this iterative algorithm

$$f^{(t+1)}(\boldsymbol{r}) = \mathcal{C}_{\check{f}}\,\mathcal{C}_{\mathrm{I}}\,\mathcal{C}_{\Omega}\,\mathcal{C}_{\mathsf{F}}\,f^{(t)}(\boldsymbol{r}) \tag{5.5}$$

is depicted in the right panel of figure 5.16.

The images restored by the iterative schemes explained above suffer from severe streak artefacts that are introduced in the very first iterations because of the discretization. A 'smooth' combination of measured and reprojected line integrals comparable to short-scan sinogram weighting (such as explained in subsection 4.5.3) does not eliminate these artefacts. There is a preferred direction of the streaks that depends on the particular range of view angles. An adaptive smoothing filter that operates orthogonally to the streak direction was therefore introduced between filtered backprojection and reprojection. The modified operator (that is not necessarily convex according to the POCS theory) is denoted as $\mathcal{C}_{\mathsf{F,as}}$ in the following. Adaptive smoothing, however, does not significantly improve the visual image quality such as shown in figure 5.17 for various view angle ranges.

The reconstruction-reprojection algorithms exhibit a semi-convergence behaviour that is typical for ill-posed inverse problems. The image quality improves within the first few iterations, but is more and more degraded in further steps. Early termination of the iteration is therefore essential to regularize the solution [67]. The optimum number of iterations was found to be about 10 for the simulations described above. After 10 steps, however, the densities within the phantom were not properly restored.

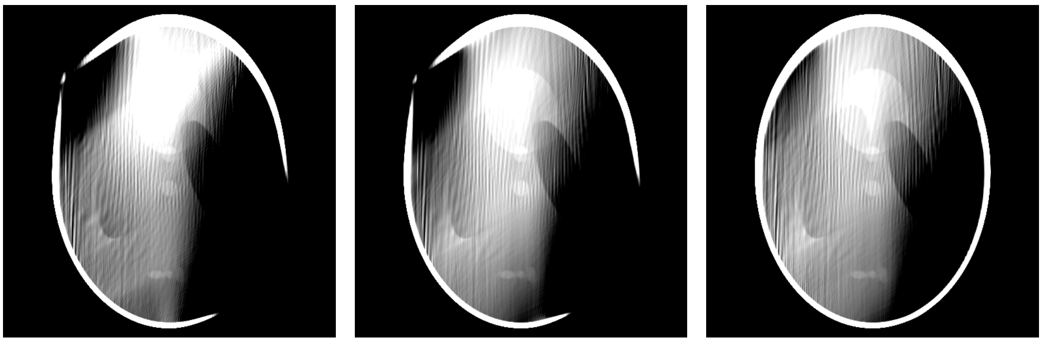

Figure 5.16: Images of the Shepp-Logan phantom restored by 10 iterations of the Gerchberg-Papoulis algorithm [27, 84] (left), with additional restriction of the attenuation coefficients to the interval $[0.0, 3.0]$ (middle) and using the two big ellipses of the phantom as a priori known reference image with a spatially constant tolerance of ± 0.3 additionally (right image).

As an alternative to the Fourier constraint C_{F}, the transmission measurements were utilized separately to enforce consistency of the image with the projections of the object. The operator $\mathcal{C}_{\mathsf{F}}$ was consequently replaced by the sequence $\mathcal{C}_{g_{M'}} \ldots \mathcal{C}_{g_2} \mathcal{C}_{g_1}$, which is equivalent to one step of the *additive algebraic reconstruction technique* (AART). Considering all of the previous constraints, this yields

$$f^{(t+1)}(\boldsymbol{r}) = \mathcal{C}_{\check{f}} \, \mathcal{C}_{\mathrm{I}} \, \mathcal{C}_{\Omega} \, \mathcal{C}_{g_{M'}} \ldots \mathcal{C}_{g_2} \, \mathcal{C}_{g_1} \, f^{(t)}(\boldsymbol{r}) \; , \tag{5.6}$$

where $g_1, g_2, \ldots, g_{M'}$ denote M' line (or strip) integrals estimated from the measurements. The support constraint C_{Ω} was accounted for implicitly by restoration on a finite rectangular grid as explained before.

Figure 5.18 shows the results obtained with this algorithm. The overall image quality is much better compared to the scheme based on successive reprojection and filtered backprojection. All details of the Shepp-Logan phantom, even the small ones at the bottom, are clearly distinguishable from the background. The images suffer from mild streak artefacts, which are introduced because of numerical errors. Another disadvantage of the method is the slow convergence. As shown in figure 5.18, it takes almost 100 iterations to restore an image of acceptable quality. A discussion of the inevitable tradeoff between accuracy of the restored image and convergence speed is presented in the subsequent subsection.

Beside visual inspection, the actual results $f_{\mathrm{act}}(\boldsymbol{r})$ obtained by the algorithms described above were compared with the definition $f_{\mathrm{def}}(\boldsymbol{r})$ of the Shepp-Logan phantom in terms of four common measures [41, 65]. These measures emphasize different aspects of image quality. They are defined for functions

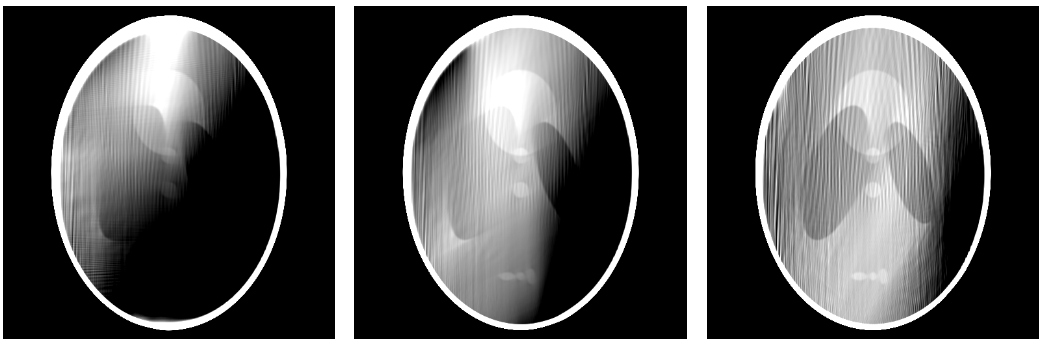

Figure 5.17: Images of the Shepp-Logan phantom restored by 10 iterations of the Gerchberg-Papoulis algorithm [27, 84] with attenuation range and reference images constraint such as in figure 5.16 and additional adaptive smoothing for view angle ranges of 90°, 120° and 150° (from left to right).

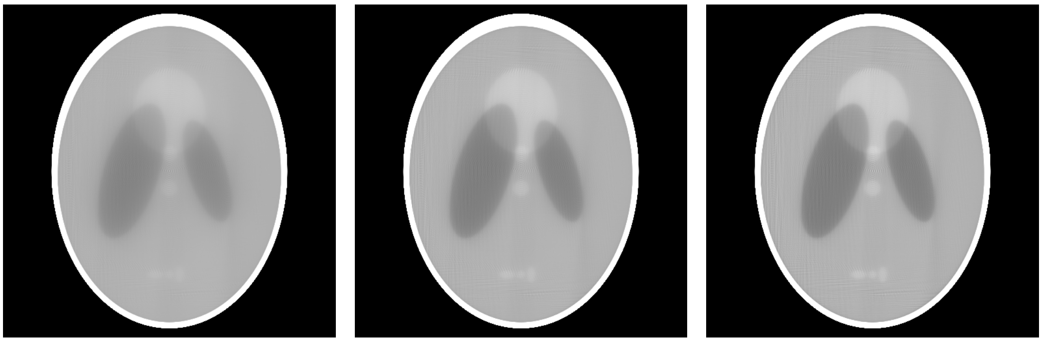

Figure 5.18: Images of the Shepp-Logan phantom restored by an ART-like procedure after 30, 60 and 90 iterations (from left to right) using the two big ellipses of the phantom as reference image with a tolerance of ± 0.3.

of continuous variables in the following notation for convenience. In practice, the measures were calculated on a discrete reconstruction grid.

$$c = \frac{\displaystyle\int \left(f_{\mathrm{act}}(\boldsymbol{r}) - \overline{f}_{\mathrm{act}}\right)\left(f_{\mathrm{def}}(\boldsymbol{r}) - \overline{f}_{\mathrm{def}}\right) \mathrm{d}^N r}{\sqrt{\displaystyle\int \left(f_{\mathrm{act}}(\boldsymbol{r}) - \overline{f}_{\mathrm{act}}\right)^2 \mathrm{d}^N r \int \left(f_{\mathrm{def}}(\boldsymbol{r}) - \overline{f}_{\mathrm{def}}\right)^2 \mathrm{d}^N r}} \tag{5.7}$$

is the correlation coefficient between $f_{\mathrm{act}}(\boldsymbol{r})$ and $f_{\mathrm{def}}(\boldsymbol{r})$, where $\overline{f}_{\mathrm{act}}$ and $\overline{f}_{\mathrm{def}}$ denote the mean intensity of the original phantom and the actual image.

$$\delta f_{\mathrm{rms}} = \sqrt{\frac{\displaystyle\int \left(f_{\mathrm{act}}(\boldsymbol{r}) - f_{\mathrm{def}}(\boldsymbol{r})\right)^2 \mathrm{d}^N r}{\displaystyle\int \left(f_{\mathrm{def}}(\boldsymbol{r}) - \overline{f}_{\mathrm{def}}\right)^2 \mathrm{d}^N r}} \tag{5.8}$$

is a *normalized root mean square distance*. The value of δf_{rms} is equal to unity if $f_{\mathrm{act}}(\boldsymbol{r})$ is a uniformly dense image with the correct average density. A large difference in few small regions causes δf_{rms} to be large.

$$\delta f_{\mathrm{abs}} = \frac{\displaystyle\int \left|f_{\mathrm{act}}(\boldsymbol{r}) - f_{\mathrm{def}}(\boldsymbol{r})\right| \mathrm{d}^N r}{\displaystyle\int \left|f_{\mathrm{def}}(\boldsymbol{r})\right| \mathrm{d}^N r} \tag{5.9}$$

is a *normalized mean absolute distance*, which emphasizes a lot of small deviations rather than a few large deviations between $f_{\mathrm{act}}(\boldsymbol{r})$ and $f_{\mathrm{def}}(\boldsymbol{r})$. δf_{abs} is equal to unity if the actual image has a value of zero everywhere.

$$\Delta f_{\max} = \max\left|f_{\mathrm{act}}(\boldsymbol{r}) - f_{\mathrm{def}}(\boldsymbol{r})\right| \tag{5.10}$$

is the *absolute maximum deviation* between $f_{\mathrm{act}}(\boldsymbol{r})$ and $f_{\mathrm{def}}(\boldsymbol{r})$. This measure assesses the worst case.

All measures are defined within the field of view determined by the geometry of the (virtual) CT scan.[2] The results of these computations are summarized in table 5.3 for various algorithms and ranges of view angles. It is, of course, not feasible to provide the results for all possible combinations of basic algorithms and additional constraints. Table 5.3 is therefore restricted to some combinations that were found to be representative. The support constraint C_Ω was implicitly accounted for in all algorithms because of the finite grid.

The first section of table 5.3 shows the values obtained by standard filtered backprojection (FBP) using the Shepp-Logan filter kernel [109] for various view angle ranges. These values correspond to the first iteration of the plain Gerchberg-Papoulis (GP) algorithm [27, 84]. The correlation coefficient c increases and the normalized distances δf_{rms}, δf_{abs} decrease when the projection data set approaches the minimal complete one. Although the maximum error $\Delta f_{\max}$ decreases, it is still quite large for a data set covering 180° (which lacks the aperture of the fan beam of about 27° compared to the minimal complete set of projections).

The measures for the Gerchberg-Papoulis algorithm [27, 84] are listed in the second section of table 5.3. After 10 iterations, all values are significantly better compared to straight-forward FBP, even for the scheme without additional constraints. Restricting the interval of 'valid' attenuation coefficients by C_I yields only slightly better results. The introduction of the reference image constraint $\mathsf{C}_{\check{f}}$ improves the correlation coefficient and the root mean squared error significantly, which indicates that the main features of the image are properly restored. The normalized mean absolute distance, however, does not drop below 0.1, which is quite large compared to other iterative schemes addressed below. This emphasizes the occurrence of a lot of small errors. This is in agreement with the observations from figure 5.16, which shows the basic shape of the phantom, but with a lot of streak artefacts.

The third section of table 5.3 shows that the performance of the constrained GP method improves with a growing range of view angles as expected. The maximum absolute deviation $\Delta f_{\max}$ keeps constant at a level of 0.3, since this is the maximum distance from the reference image that was allowed in the simulation.

The fourth section of table 5.3 deals with the algebraic technique and additional constraints. The restriction of the range of attenuation coefficients

[2] The corresponding limits are omitted in the above formulae for the sake of simplicity.

improves the performance only slightly such as also observed for the GP algorithm. Using the constraints C_{Ω} and C_{I}, the root mean squared deviation and the mean absolute deviation are only slightly better compared to the GP algorithm, and the maximum deviation is even larger in this case. The reference image constraint, however, turns out to be very useful in the AART scheme. This is demonstrated by the correlation coefficient close to unity and the small mean deviations δf_{rms} and δf_{abs}. The value of the maximum deviation is significantly smaller than $\varepsilon(\boldsymbol{r}) = 0.3$, whereas this maximum

Algorithm		t	$\alpha_{\max}$	c	δf_{rms}	δf_{abs}	$\Delta f_{\max}$
FBP	$\mathcal{C}_{\Omega}$		60°	0.7003	1.6957	0.8879	2.8402
			90°	0.7246	0.9290	0.6752	1.9372
			120°	0.8162	0.4151	0.4626	1.7937
			150°	0.9229	0.1508	0.2796	1.7672
			180°	0.9751	0.0523	0.1657	1.1611
GP	$\mathcal{C}_{\Omega}\ \mathcal{C}_{\mathsf{F}}$	10	120°	0.9245	0.1477	0.2217	1.3817
	$\mathcal{C}_{\mathrm{I}}\ \mathcal{C}_{\Omega}\ \mathcal{C}_{\mathsf{F}}$	10	120°	0.9402	0.1218	0.1660	1.3673
	$\mathcal{C}_{\check{f}}\ \mathcal{C}_{\mathrm{I}}\ \mathcal{C}_{\Omega}\ \mathcal{C}_{\mathsf{F}}$	10	120°	0.9894	0.0272	0.1005	0.3000
	$\mathcal{C}_{\check{f}}\ \mathcal{C}_{\mathrm{I}}\ \mathcal{C}_{\Omega}\ \mathcal{C}_{\mathsf{F},\mathrm{as}}$	10	120°	0.9894	0.0272	0.1003	0.3000
GP	$\mathcal{C}_{\check{f}}\ \mathcal{C}_{\mathrm{I}}\ \mathcal{C}_{\Omega}\ \mathcal{C}_{\mathsf{F}}$	10	60°	0.9767	0.0562	0.1676	0.3000
		10	90°	0.9825	0.0466	0.1458	0.3000
		10	120°	0.9894	0.0272	0.1005	0.3000
		10	150°	0.9954	0.0121	0.0552	0.3000
		10	180°	0.9989	0.0018	0.0131	0.3000
AART	$\mathcal{C}_{\Omega}\ \mathcal{C}_{g_{M'}} \ldots \mathcal{C}_{g_1}$	100	120°	0.9248	0.1451	0.2187	1.5673
	$\mathcal{C}_{\mathrm{I}}\ \mathcal{C}_{\Omega}\ \mathcal{C}_{g_{M'}} \ldots \mathcal{C}_{g_1}$	100	120°	0.9408	0.1164	0.1527	1.5823
	$\mathcal{C}_{\check{f}}\ \mathcal{C}_{\mathrm{I}}\ \mathcal{C}_{\Omega}\ \mathcal{C}_{g_{M'}} \ldots \mathcal{C}_{g_1}$	100	120°	0.9998	0.0001	0.0071	0.0890
AART	$\mathcal{C}_{\check{f}}\ \mathcal{C}_{\mathrm{I}}\ \mathcal{C}_{\Omega}\ \mathcal{C}_{g_{M'}} \ldots \mathcal{C}_{g_1}$	100	60°	0.9999	0.0001	0.0062	0.0370
		100	90°	0.9998	0.0001	0.0045	0.0369
		100	120°	0.9998	0.0001	0.0071	0.0890
		100	150°	0.9998	0.0001	0.0046	0.0369
		100	180°	0.9999	0.0001	0.0046	0.0370

Table 5.3: Quantitative assessment of various iterative image restoration schemes and standard image reconstruction algorithms regarding limited-angle data sets. Correlation coefficient c, normalized root mean square distance δf_{rms}, normalized mean absolute distance δf_{abs} and absolute maximum deviation $\Delta f_{\max}$ such as defined in equations (5.7)–(5.10) are listed for the standard Shepp-Logan phantom and various view angle ranges $[0°, \alpha_{\max}]$. t denotes the number of iterations.

allowed distance from the reference image is reached by the GP algorithm. The maximum deviation, however, is almost a factor of nine larger than the minimum attenuation variation within the Shepp-Logan phantom. This indicates some severe artefacts in the images. The root mean square error of 10^{-4}, on the other hand, demonstrates that these large deviations occur only in very few places. These interpretations of the image quality measures confirm the conclusion obtained by visual inspection of the final image in figure 5.18.

The performance of the algebraic restoration scheme using a reference image is assessed in the last section of table 5.3 for various view angle ranges. The values of c and δf_{rms} indicate a good restoration, even for a data set covering only 60°. The other two measures do not constantly worsen with decreasing range of view angles.

5.3.2 Optimization of convergence

The convergence speed of AART depends significantly on the order in which the constraints $\mathcal{C}_{g_{M'}} \dots \mathcal{C}_{g_2} \mathcal{C}_{g_1}$ are applied in each iteration [36]. An appropriate choice of the relaxation parameter λ (such as introduced in theorem A.8) is also important for the properties of the algorithm [78].

Two different projection access schemes were utilized, namely the *sequential access scheme* (SAS) and the *random permutation scheme* (RPS). Various simulation studies were performed in order to investigate the influence of the relaxation parameter for these schemes. The results showed that the choice of a relatively small parameter of the order of 0.05 is essential for obtaining sufficiently accurate results. The application of RPS enables the use of relaxation parameters about ten times higher, but does not significantly ac-

Algorithm	λ	c	δf_{rms}	δf_{abs}	Δf_{max}
AART/SAS	0.05	0.9999	0.0001	0.0062	0.0370
AART/RPS	0.50	0.9996	0.0003	0.0154	0.0343
MART		0.9995	0.0007	0.0083	0.5171

Table 5.4: Performance of the additive algebraic reconstruction technique (AART) with sequential access scheme (SAS) and random permutation scheme (RPS) and of the multiplicative algebraic reconstruction technique (MART). The values are listed for an image of the Shepp-Logan phantom restored from projections within 60° using a reference image constraint.

celerate convergence, particularly if the range of view angles is very narrow. Table 5.4 shows the performance measures defined in the previous subsection for a view angle range of 60°. The data demonstrate that there is no great difference in image quality after a specific number of iterations using SAS or RPS with optimized relaxation parameters.

The *multiplicative algebraic reconstruction technique* (MART) was also tested on limited-angle data, although this kind of iterative correction is not a valid POCS constraint operator. The correlation coefficient and the root mean squared error are of the same order as for AART as shown in table 5.4. The maximum error is significantly larger than in the images restored by AART.

5.3.3 Noise characteristics

The iterative procedure in equation (5.6) was also applied to a water disc phantom as shown in figure B.2. This phantom comprises seven circular inserts that represent typical attenuation coefficients of various tissue types. The seven inserts refer (relative to water) to lung (0.25), fat (0.91), pancreas (1.04), heart (1.05), liver (1.06), spongy bone (1.13) and compact bone (1.80). The water disc phantom is formally defined in table B.2.

The geometry of the diagnostic CT scanner specified in subsection 4.2.1 was utilized for the simulations, except the single-row detector was modelled as flat instead of curved. Line integrals through the phantom were calculated analytically using the formulae in section B.1. For each sample, 15 line integrals were averaged in order to approximate the integration over the finite detector bin size.

The photon statistics were considered as explained in section B.2 in order to investigate the influence of noisy projection data on the convergence. Other potential sources of noise (e.g., the read-out electronics) were neglected because modern CT scanners are well designed to be almost quantum-noise limited [36]. A slice thickness of 3 mm, an effective source fluence of 10^6 photons per detector bin and a linear attenuation of $0.19\,\mathrm{cm}^{-1}$ for water were assumed. These are typical values for diagnostic CT examinations [36, 50].

An image of the disc phantom was restored by means of the algebraic reconstruction technique from projections covering a view angle range of 120°. This image comprises 512×512 pixels at a pitch of 0.8 mm along its columns and rows. A uniform water disc was utilized as reference image $\check{f}(\boldsymbol{r})$, allowing a maximum distance $\varepsilon(\boldsymbol{r}) = 1$ inside the disc and $\varepsilon(\boldsymbol{r}) = 0$ outside the disc. No further constraints were applied, since the known spatial support of the object and the interval $[0.0, 2.0]$ of relative attenuation coefficients are implicitly considered by the definition of the reference image constraint.

Table 5.5 lists the mean attenuation coefficients and the corresponding signal-to-noise ratios (SNR) determined from the restored image. The values for the image obtained by full-scan filtered backprojection using the Shepp-Logan filter kernel [109] are included for comparison. The SNR for the limited-angle image was normalized with respect to the full-scan in order to enable a direct comparison of the data. This normalization yields a factor of $\sqrt{3}$ because the SNR is inversely proportional to the square root of the exposure [50].

The ART procedure yields mean attenuation coefficients that are not as accurate as those reconstructed by full-scan filtered backprojection. The deviations are relatively small for soft tissues (pancreas, heart, liver), but more substantial at the bottom (fat) and top (compact bone) end of the scale. The overall correlation coefficient between true and ART-restored values is quite high (0.9985). The offset of the regression line (0.0591) is close to zero, but its slope (0.9368) deviates significantly from unity.

The signal-to-noise ratio generally increases for filtered backprojection with increasing attenuation coefficient, except the value for water, which was measured at the centre of the slice. The SNR values for ART are substantially lower and do not show this strict tendency. A main contribution to these SNR values comes from structured (typically streak-shaped) artefacts that are introduced in the limited-angle image restoration.

Tissue type	True value	FBP		ART	
		Mean	SNR	Mean	SNR
lung	0.25	0.2499	21.9	0.2835	8.6
fat	0.91	0.9100	61.5	0.8983	28.7
water	1.00	1.0002	52.5	0.9871	30.1
pancreas	1.04	1.0399	64.6	1.0306	38.4
heart	1.05	1.0501	64.0	1.0372	49.2
liver	1.06	1.0600	65.5	1.0630	45.8
spongy bone	1.13	1.1302	66.6	1.1554	42.4
compact bone	1.80	1.8000	84.9	1.7226	48.8

Table 5.5: Accuracy of full-scan filtered backprojection (FBP) and image restoration from 120° limited-angle data (ART) using noisy projection data. The table lists the mean attenuation coefficients and signal-to-noise ratios (SNR) determined from images of the water-disc phantom.

5.3.4 Reduction of motion artefacts

The ART-like image restoration procedure was also applied to clinical data of a beating heart. The projections were acquired using a diagnostic CT scanner as described in subsection 4.2.1. The helical scan mode was applied in order to enable fast volume coverage.

The electrocardiogram (ECG) of the patient was recorded simultaneously during the thorax scan using a sampling frequency of 250 Hz. This sampling does not preserve all information content contained in the ECG signal [71], but is sufficient for the analysis required here. The algorithm developed by Sennst [106] was employed for detecting the R-peaks of the ECG with respect to the start of the CT scan. An example of such an ECG signal with its correlation to the view angle is depicted in figure 5.19.

An initial estimate was reconstructed by means of standard filtered backprojection (FBP) using the contangent filter kernel. This is the equivalent of the Shepp-Logan filter [109] for a curved detector. No axial interpolation of the helical into planar data was performed in order to reduce the combination of data from different heart phases to a minimum. The image was reconstructed on a grid comprising 512×512 pixels at a pitch of 1.0 mm in each direction.

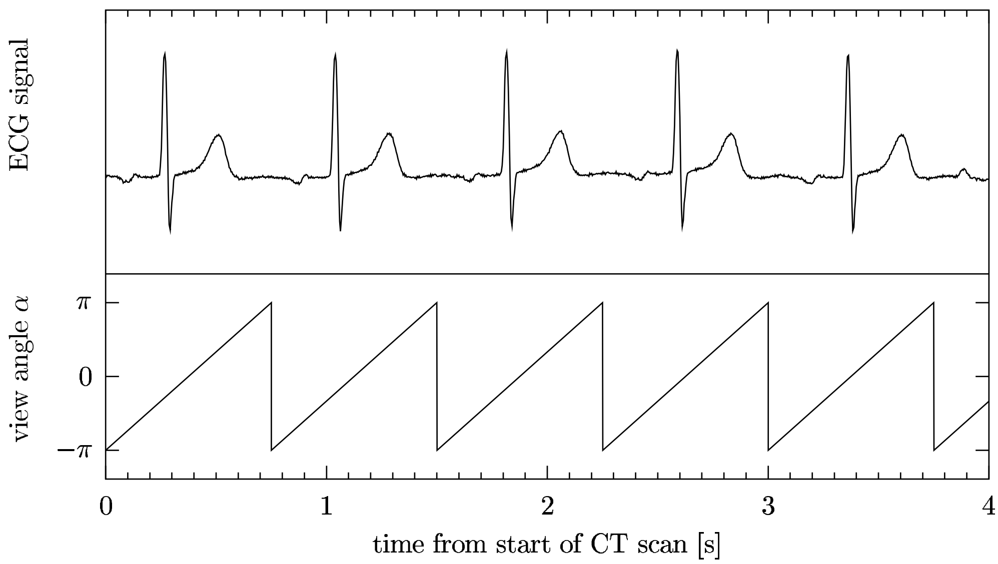

Figure 5.19: Electrocardiogram of a patient recorded synchronously with the projection view angle during a thorax CT scan for identifying raw data segments with few heart motion. The ECG signal is plotted in arbitrary unit because the absolute range is not relevant for detecting the R-peaks.

Based on this initial image, an ART-like restoration was performed using a view angle range of 90°. The data segment ending directly before the corresponding R-peak in the ECG was chosen for the restoration. This heart phase is nearly iso-volumetric [105] and provides therefore the most consistent data. The initial image was also used as reference image allowing a maximum distance of $0.3\,\mathrm{cm}^{-1}$. In each iteration step, all pixels outside the field of view were set to zero to consider the a priori known support constraint.

The results of this procedure are presented in figure 5.20. A comparison of the initial estimate and the image after 100 iterations shows that the heart motion artefacts are removed to some extent, altough the differences between the two images are not very large. However, the small calcification shows up more clearly in the ART than in the initial FBP image. On the other hand, some mild streak artefacts are introduced due to numerical errors occurring during the iterative procedure.

In various experiments, it was found important to consider all objects within the field of view (including the patient support table) in the image restoration algorithm. The parts outside a particular region of interest (ROI) could, in theory, be initially reprojected and subtracted from the measured data. This would allow for performing the iterative procedure only within the ROI, thus saving computation time. In practice, however, this yields often undesired artefacts at the edges of the ROI.

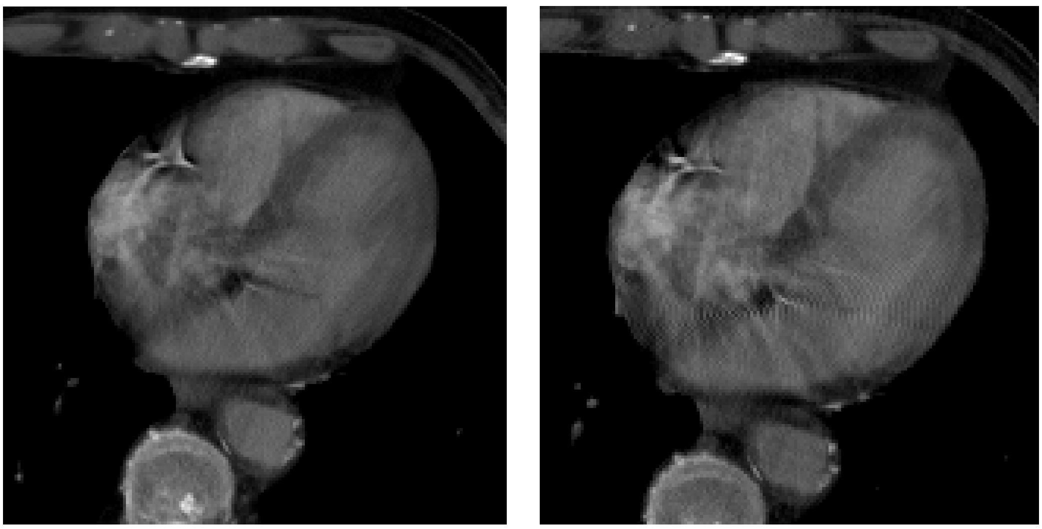

Figure 5.20: CT images of a beating heart. Initial estimate obtained from standard filtered backprojection (left) and result after 100 ART iterations (right). After image restoration, the small calcification shows up a little bit more clearly.

5.4 Image registration

A phantom study was performed in order to assess the feasibility of employing C-arm X-ray devices such as considered above in image-guided procedures. More specifically, the potential of cone-beam CT to detect and quantify patient set-up uncertainties was investigated. Such set-up uncertainties can occur between therapy planning and treatment or between several treatment phases.

5.4.1 Experimental set-up

For the feasibility study, three slices from the neck region of a Rando Alderson head phantom were mounted to a dedicated mechanical support system. This system allows to deliberately introduce well-defined translations and rotations in order to simulate patient set-up errors.

Several kilovoltage and megavoltage cone-beam CT scans of the humanoid phantom were recorded using the hardware and the acquisition protocol described in subsection 4.2.2. The non-parametric technique for geometric calibration was applied by scanning the helix phantom off-line. All projections were preprocessed as explained in section 4.3. The actual, transverse images of the phantom were reconstructed employing the modified Feldkamp algorithm [24] such as described in subsection 4.5.1 and the standard filter kernel proposed by Shepp and Logan [109]. The in-plane pixel pitch in each direction as well as the spacing of the transverse images was 0.7 mm, resulting in an isotropic reconstruction volume.

The outline of the phantom was delineated in each transverse image automatically by applying an appropriate threshold. The attenuation coefficients outside the phantom were then set to zero in order to minimize the impact of streak-shaped view aliasing artefacts due to the low number of projections. No further postprocessing was performed on the image data sets.

5.4.2 Registration accuracy

A mutual information (MI) matching algorithm was utilized for the rigid-body registration of the three-dimensional image data sets. The concept of this algorithm was described by Maes et al. [68] originally. Powell's method [92] was employed to maximize the mutual information as function of three translational and three rotational parameters, in order two align two image data sets geometrically.

In the implementation of the matching algorithm, a certain number of randomly distributed samples is taken from the floating image instead of involving all pixels in the MI calculation in order to decrease computation time. Changing the number of samples, the registration result varies therefore slightly. For a reasonable number between $4 \cdot 10^4$ and $5 \cdot 10^5$, however, these random variations were found to be less than 0.2 mm for translations and less than 0.3° for rotations. All data sets were therefore registered using $5 \cdot 10^4$ samples in order to ensure stable results and as well as short computation time.

The uncertainties remaining after mutual information matching of two data sets were compared to the reference values known from the design of the mechanical support system. For translations, the mean and maximum difference between reference and calculated values were −0.24 mm and 1.13 mm, respectively. The corresponding, single standard deviation was 0.58 mm. The mean and maximum angular difference for the three rotational parameters were 0.19° and 1.25°, respectively. The standard deviation of the angular difference was 0.46°.

Chapter 6

Discussion

X-ray transmission computed tomography (CT) is a well-established technique, which is crucial for modern clinical diagnosis. CT is furthermore a valuable tool in individual (radiotherapy or surgical) treatment planning in order to locate pathologic lesions and particularly sensitive structures, since it provides a reliable anatomical model. For treatment, however, the images have to be registered with the actual anatomy of the patient.

For neurosurgery [95] or radiotherapy [60] of the brain, this registration can be performed very accurately by means of stereotaxy. This method relies on rigid immobilization of a patient for defining a frame of reference that is firmly related to the anatomy. Stereotactic accuracy is limited when a region of interest is difficult to immobilize or substantial organ motion occurs between planning and treatment.

This limitation is currently being tackled by the the implementation of appropriate *imaging facilities at treatment site* that enable the acquisition of images of the actual anatomy in the treatment position. X-ray computed tomography is quite a promising imaging modality concerning this aim, since it provides images with high spatial resolution and does not introduce geometric distortions. Cone-beam CT enables the scanning of large volumes of interest in reasonably short time. The patient does not need to be moved for imaging when (mobile) open C-arm devices are utilized for the acquisition of X-ray projections.

The implementation of cone-beam CT at the treatment site introduces, on the other hand, new problems compared to the well-established diagnostic CT. Some of the current challenges that were investigated in this thesis will be discussed in the following.

6.1 Geometric calibration

Conventional C-arm gantries such as employed in angiography devices and linear accelerators exhibit significant *geometric uncertainties*, i.e., the projection geometry at each particular view (from the X-ray source to the detector) is not known exactly [21, 34, 134]. The example in subsection 2.2.3 demonstrates that tomographic reconstruction yields images of very poor quality when the data acquisition geometry is not accurately taken into account.

A *geometric calibration procedure* was implemented in order to correct for these uncertainties. The method utilizes a dedicated phantom containing an array of fiducial markers [99]. The phantom defines a coordinate system for image reconstruction. This coordinate system can be related to another frame of reference (fixed in three-dimensional space) by aligning it properly, for example, using laser marks. For each view, an X-ray image of the calibration phantom is taken in order to estimate the particular projection geometry.

The relative arrangement of the markers within the phantom needs to be very exact. This has been referred to as major drawback of such a calibration procedure previously [96]. A simulation study showed that, for a typical cone-beam geometry in medical imaging, the maximum tolerance of the marker positions should be less 0.1 mm in each direction. This can be guaranteed when a real calibration phantom is built in a sophisticated workshop. Even considering the use of such an accurate phantom, the calibration method is much less demanding (and expensive) than exact tracking of position and orientation of X-ray source and detector.

The information obtained in the calibration procedure covers all degrees of freedom of an arbitrary, linear cone-beam projection. In numerous previous applications of C-arm devices, only a centre-of-rotation correction was performed [14, 22, 72, 73, 101]. Although this correction may be sufficient in many practical cases, the additional geometric information that is easily available from a calibration scan should not be discarded.

The X-ray detector itself is assumed to be free of any non-linear geometric distortion. This assumption is perfectly adequate for flat-panel imagers. Image intensifiers, which introduce significant in-plane distortions, are expected to be replaced by this new generation of detectors in near future. Various techniques for correcting in-plane distortions, however, are available elsewhere [23, 35]. They could be applied prior to the geometric calibration procedure proposed here.

Two different methods were implemented for estimating the projection geometry from the calibration images. The *parametric* method provides a set of eleven geometric parameters for each view. In the *non-parametric* technique, a 3×4 projection matrix mapping three-dimensional object into two-dimensional detector coordinates is calculated for each view. Both approaches were carefully compared by means of computer simulations. The reprojection error of test points randomly distributed within the field of view was chosen as criterion for the comparison because this is an adequate measure for geometric accuracy. Using the non-parametric method, the mean radial reprojection error is about a tenth of the detector pixel size. The parametric method yielded substantially larger (statistically significant) deviations. This finding supports the argumentation of Wiesent et al. [134] who prefer a non-parametric method.

Roguée et al. [98] obtained the opposite result, although they employed the same measure. Comparing some one-dimensional cross-sections through the field of view, they observed slightly larger reprojection errors for the non-parametric technique than for the parametric one, especially for a low number of fiducial markers. The key for understanding this contradiction is the difference in simulation design. In this thesis, X-ray projections of the (virtual) calibration phantom were computed analytically in order to simulate the discretization due to the finite detector pixel size properly. Roguée et al. [98] calculated the centre positions of the markers analytically and varied them by samples drawn from a non-truncated Gaussian distribution of zero mean and specific standard deviation. This results (even for a small standard deviation) in some very inaccurate estimates for the marker positions. It is well known that a linear least-squares fit (such as utilized in the non-parametric method) is extremely sensitive to (even a few) large errors in the input data [92]. Uncertainties larger than the detector pixel size, however, do not occur in practice, except when the algorithm determining the marker positions fails (for example, because of artefacts). The occurrence of few large errors in detecting the markers translates, in this sense, to a very inaccurate set-up of few markers within the calibration phantom. This is in agreement with the observation that the parametric method is, in relative terms, less sensitive to increasing marker tolerance than the non-parametric one. However, the simulation design utilized in this thesis resembles reality better than the design employed by Roguée et al. [98].

The above considerations emphasize another the desirable feature of the non-parametric technique. The goodness of the fit (the χ^2 value) can be used for uncovering errors in the detection step reliably, since a particular χ^2 threshold is not exceeded when all markers have been detected correctly.

The estimation of geometric parameters is related to the minimization of a highly non-linear objective function. This function is not necessarily convex, i.e., it can exhibit multiple local minima. Some of the desired parameters can be significantly correlated. Because of these problems observed previously [38, 39, 64, 96], there is no guarantee of finding the global minimum of the objective function [81]. The parametric method can deliver completely unrealistic results when it is trapped in a local minimum of the objective function. Various heuristic approaches such as successive variation of different parameters [38] or distinction of intrinsic and extrinsic parameters [96] have been proposed to stabilize the minimization, but none of the authors present a rigorous mathematical analysis of the objective function.

The non-parametric method, on the other hand, lacks an intuitive geometric interpretation of the results, i.e., the projection matrices cannot be easily checked for plausibility. Their *decomposition into geometric parameters* by means of non-linear (least-squares) fitting would introduce the same problems as considered above. An analytical decomposition procedure proposed previously [70] was therfore implemented and analysed by computer simulations. The most critical parameters, namely the source-to-detector distance and the coordinates of the view reference point, are generally estimated even less accurately than for the parametric calibration method. The decomposition of projection matrices is therefore of limited use, but might be at least employed to check the correct orientation of particular views.

The estimation of geometric parameters, however, is not essential for successfully accounting for the calibration information within backprojection and reprojection. The projection matrices can be processed without explicit decomposition using the algorithm described in appendix C in detail. This algorithm is computationally slightly more efficient than the one presented by Wiesent et al. [134] previously. Its implementation does not require the interpolation of the acquired projections to an ideal data set as it has been proposed by Fahrig et al. [22]. This is quite advantageous, since each additional interpolation step potentially degrades spatial resolution.

The reproducibility of the flex effects was carefully investigated for a linear accelerator combined with a flat-panel imager. The experiments were performed in step-and-shoot as well as in continuous gantry rotation mode. The results indicate that the flex effects are very reproducible. As a consequence, the geometric calibration procedure discussed above can be applied off-line. This is desired because an online calibration by placing fiducial markers around the patient such as demonstrated by Navab et al. [79] may not be feasible in all cases. This is particularly true for imaging at the treatment site when easy access to the patient is required. The results on flex reproducibility are valid only for the one experimental cone-beam system that was investigated. Similar behaviour, however, may be expected for most C-arm shaped gantries. Nevertheless, a careful investigation, for example by using the protocols described in subsection 5.1.5, should be performed for every device separately.

6.2 Image reconstruction

The cone-beam projections were always recorded using a *single-circular scan*. Although this data acquisition scheme does not yield complete projection data [25, 32, 112, 124], it is often the only feasible one at treatment site. Exact reconstruction is then possible only in the mid-plane. Increasing the distance from this plane, the image quality is more and more degraded, mainly by blurring in the axial direction. In medical applications, the projections are furthermore truncated in the axial direction, which introduces additional artefacts at the inferior and superior edges of the field of view.

The images presented in this thesis indicate that the artefacts are normally acceptable if a region of interest is close to the mid-plane. This can be guaranteed in most applications. The investigations of the experimental cone-beam systems described in subsection 4.2.2 suggest that a spatial resolution of about 1.3 mm can be achieved for high-contrast objects, if only 120 projections per full revolution are used. Wiesent et al. [134] obtained a resolution between 0.1 and 0.3 mm using 50–100 cone-beam projections recorded by an angiography device. It is not clear whether the values refer to pure spatial resolution or to the accuracy with which the centre of an object (e.g., a vessel filled with contrast agent) can be determined. Such a high resolution, however, could not not be obtained using a linear accelerator and a therapy simulator because of the relatively large focal spots.

In current C-arm cone-beam CT systems such as mentioned above, only about 100 projections are recorded per full rotation, compared to about 1000 views taken by a diagnostic scanner comprising a ring gantry. The low number of projections causes a significant level of streak-shaped background artefacts [21, 134] because the condition for optimum raw data sampling [46] is severely violated. Future technical improvements may help to overcome this limitation. For kilovoltage imaging, the main reason for using few projections is, in many cases, a reduction of the data acquisition time rather than concerns about the dose delivered to the patient.

The *filtered-backprojection* method proposed by Feldkamp et al. [24] was employed for approximate image reconstruction from single-circular cone-beam projections. The original algorithm was modified in order to account for flex effects. Information obtained from a calibration scan is considered exactly within the backprojection step, which is the most crucial part of the algorithm concerning geometric accuracy. The filtering step was not corrected. This approximation is perfectly adequate considering typical flex effects of C-arm devices [21, 34]. The modified Feldkamp algorithm yields good image quality; the level of blurring and streak artefacts due to flex effects is significantly reduced.

In theory, a mathematically exact reconstruction without introducing additional interpolations could be obtained by the *filtered-layergram method* [113]. In this method, the order of backprojection and deconvolution is swapped compared to filtered backprojection. Applying exact backprojection (accounting for all geometric uncertainties) into a regular grid before deconvolution would not require any changes to the filter kernel, provided the irregular sampling due to geometric instabilities is still dense enough. However, the filtered-layergram is computationally very demanding as explained in detail in subsection 3.2.1.

The Feldkamp algorithm [24] is currently the method of choice for most single-circular cone-beam computed tomography applications because it is very efficient [21, 34, 134]. The algorithm exploits the projection data that are available in a mathematically rigorous manner. This is obvious from the fact that the exact cone-beam reconstruction formula suggested by Defrise and Clack [17] reduces to the Feldkamp formula for a single-circular source trajectory. For discrete data, Feldkamp reconstruction of single-circular projections is, close to the mid-plane, even more accurate than potentially exact shift-variant filtered backprojection of complete cone-beam data because it involves fewer interpolations [18]. This is also true for potentially exact Radon rebinning methods.

The Feldkamp algorithm [24] does not necessarily yield the optimum reconstruction result. Various modifications have been applied in order to improve the image quality. Grass [33], for example, showed that the well-known intensity drop in axial direction can be reduced by partial parallel rebinning of the cone-beam projections. Unfortunately, a method that accounts for geometric calibration information within the rebinning (without introducing additional interpolations) is not yet available. For this reason, modified Feldkamp algorithms were not considered here. The development of a corresponding concept would be interesting for future research.

6.3 Image restoration

There are various reasons for only measuring *partial projection data*, particularly in medical imaging at treatment site. The incompleteness of cone-beam projections recorded in a single-circular scan is discussed in the previous section and not considered here. This section deals with situations in which mathematically exact image reconstruction without analytical continuation of the projection data is not even possible in the mid-plane.

Subsection 2.2.1 introduces the *interior problem* (lateral truncation), the *exterior problem* ('total' absorption within a part of the object) and the *limited-angle problem* (restricted range of view angles). In this thesis, the limited-angle problem was investigated explicitly in order to account for internal organ motion that is significant compared to the data acquisition time, thus not allowing to record a complete set of consistent projections. The concepts employed here, however, are quite general. Much of the discussion following applies also to the interior and the exterior problem.

Although limited-angle projection data sets of spatially finite objects can be, in theory, completed by means of analytical continuation [66, 77], these attempts suffer from intense noise amplification in practice [27]. This is not surprising, since it has been proved previously that limited-angle computed tomography is a severely ill-posed inverse problem [77].

The theory of *projections onto convex sets* (POCS) [103, 138, 139] was applied in this thesis for restoring images from incomplete projection data. This mathematical framework covers numerous iterative schemes that enforce consistency of the image with measured data and prior knowledge by successive application of constraint operators.

Various iterative procedures were investigated regarding their capability for image restoration from limited-angle projection data sets. Noise-free as well as noisy, analytically generated phantom data were utilized in these studies. The results were visually assessed and mathematically compared with the phantom definition by means of four standard measures. Correlation coefficient, root mean square error, mean absolute error and maximum error emphasize different aspects of image quality such as structured artefacts versus small large-area deviations [41, 65].

Iterative reconstruction-reprojection procedures that are based on the original *Gerchberg-Papoulis algorithm* [27, 84] did not deliver satisfactory results. The correct local mean values were not restored in all parts of the image. The images suffer furthermore from severe streak artefacts. Neither adaptive filtering nor ‘smooth combination’ of measured and reprojected line integrals comparable to ‘smooth sinogram weighting’ for short-scan CT reconstruction [85] reduced these streaks significantly. Restricting the attenuation coefficients to a reasonable (non-negative) range improved the results only slightly. Introducing a reference image constraint increased the correlation coefficient and decreased the root mean square error substantially, but did not avoid the problem of structured artefacts. The latter observation is confirmed by the fact that the maximum error remained at the maximum allowed distance from the reference image.

The reconstruction-reprojection algorithms exhibited a a semi-convergent behaviour. This means that the image quality improves within the first iterations, but is more and more deteriorated in further steps. This typical for (severely) ill-posed inverse problems and requires the determination of the optimum number of iterations for regularizing the solution [67]. The performance measures and visual inspection of the images showed that the algorithm should be terminated after about 10 steps. However, this did not yield sufficiently accurate results.

Iterative image restoration algorithms based on the *algebraic reconstruction technique* (ART) [48] yielded much more accurate results. In almost all cases, the performance measures exhibited better values than obtained by reconstruction-reprojection methods. Adding only an attenuation-range constraint to plain ART did not increase its performance considerably. The introduction of reference images is very promising for improving the convergence of ART. In the simulations, the maximum deviation from the phantom definition dropped by a about factor of ten below the maximum allowed distance from the reference image.

The simulations demonstrated that it usually takes about 100 iterations to restore a reasonable image by means of an ART-like procedure. The speed of convergence depends significantly on the relaxation parameter and on the order in which the projections are processed. A rigorous mathematical analysis of the full-scan case suggests quite a small relaxation parameter (of the order of 0.05) for the *sequential access scheme* (SAS) because consecutive projections are highly correlated [41, 78]. Convergence can be accelerated using the *random permutation scheme* (RPS) when choosing a relaxation parameter close to unity [78]. Various simulation studies indicated that the latter statement does not hold for limited-angle data sets. A general advantage of one of these schemes was not found. More sophisticated orderings such as the *multi-level scheme* (MLS) [36] have been developed for specific full-scan geometries and are not applicable to limited-angle computed tomography.

The POCS theory yields an *additive* ART algorithm for enforcing consistency of an image with the measured projection data [89]. The implementation of a *multiplicative* correction in each iteration step was also tested, although this is not covered by the POCS convergence theorem. The performance measures discussed above showed that the multiplicative version results in comparable values for the correlation coefficient and the root mean square error, but tends to produce more structured artefacts.

Quadratic optimization methods form another class of image restoration algorithms, which includes the well-known *simultaneous iterative reconstruction technique* (SIRT) [28]. These methods allow any type of convex constraint to be applied in a similar way to the POCS algorithm. Because of two disadvantages they were not subject to a detailed investigation regarding the limited-angle problem in this thesis. Quadratic optimization techniques are known to converge very slowly and require additional storage for an intermediate image or projection data set [41].

Constraint operators connecting object and projection space were realized by (filtered) backprojection and reprojection techniques [76, 69]. For this reason, all iterative schemes considered here are capable of accounting for geometric information obtained from the calibration procedure discussed previously. The application of Fourier methods [88, 89] would not provide advantages compared to backprojection-reprojection methods. An extension of the calibration procedure enabling an implementation of the Gerchberg-Papoulis algorithm [27, 84] iteration step in Radon space [54] might avoid some of the numerical problems observed in the simulation. Successive backprojection and reprojection, however, cannot be avoided if constraints are to be applied to the image in order to enforce its consistency with prior knowledge of the object.

Studies on the computational complexity of the iterative schemes are not presented in this thesis. Backprojection and reprojection, which turned out to be the most time-consuming parts of the algorithms, have been analysed in detail previously. The computation time required for the application of additional constraint operators is negligible compared to backprojection and reprojection.

Based on the above considerations, a new iterative restoration scheme was proposed for improving images that suffer from organ motion artefacts. In particular, imaging of a beating heart was considered in this context. The procedure starts with a standard (short-scan) filtered backprojection providing accurate attenuation coefficients in regions that are not affected by the heart beat. This can be easily concluded from the properties of the

Radon transform [77]. This initial estimate serves as reference image for an ART-like iterative procedure considering only the most consistent part of the projection data set. An appropriate range of view angles is selected from evaluating electrocardiogram (ECG) data, which need to be recorded synchronously with the CT scan. The algorithm is capable of restoring details that are otherwise blurred by organ motion. The images, however, suffer from mild (streak) artefacts introduced by the iterative procedure.

Although further research (on additional constraints) is necessary to improve the image quality, the iterative scheme should be considered as an interesting alternative compared to current methods of ECG-correlated heart imaging [47]. Short-scan data sets often do not provide consistent measurements. The *combination of data segments* from various heart cycles, on the other hand, reduces motion artefacts, but introduces new errors [47]. Data combination does not work perfectly because even successive heart cycles exhibit slight variations. This is particularly true for patients suffering from heart disease. These patients are most likely to be subject to a dedicated CT examination.

The problem of organ motion during CT imaging will probably remain a challenge for the next years. Although scanning times have been continuously decreased, they are not expected to drop by an order of magnitude in near future. Alternative concepts have been proposed for decreasing scanning time. Using *electron beam scanners*, the raw data for one slice can be acquired within 50–100 ms, which is about a tenth of the rotation time of modern CT gantries. The *dynamic spatial reconstructor* comprises 14 X-ray tubes thus allowing fast volume coverage. Both concepts could not be clinically established because of technical problems and the immense costs [50]. It seems therefore worthwhile to continue research on image restoration algorithms in order to tackle the problem of organ motion.

6.4 Image registration

A phantom study was performed in order to assess the potential of cone-beam computed tomography using a C-arm device for image-guided procedures. The results of this investigation indicate that mutual information matching could be a useful tool for patient set-up verification at the treatment site. Even data sets containing streak artefacts due to angular under-sampling as well as beam-hardening artefacts were registered fairly well.

Mutual information matching as proposed by Maes et al. [68] does not require any user interaction except of defining a reasonable number of samples in the floating image. This is an important criterion for real-time applications. The registration of two data sets took between 2 and 5 minutes on a DEC Alpha workstation at 500 MHz. The current implementation could be optimized for speed and parallelized in order to reach a clinically acceptable computation time.

Although the performance of the mutual information matching was good for the cases investigated, there is no (theoretical) guarantee of success. In principle, the algorithm can be trapped in a local minimum of the objective function due to the non-linear nature of the optimization problem. A visual inspection of any registration result obtained automatically is therefore essential in medical applications. Using a sophisticated image fusion tool that displays both data sets, such an inspection can be easily performed. Moreover, the tool should allow efficient, manual corrections.

Applying a registration algorithm in three-dimensional object space has some advantages compared to the approaches based on transmission images as reviewed in subsection 2.1.3. A small number of transmission images (typically an orthogonal pair) do not contain complete information on the three-dimensional anatomy of the patient. Ambiguities can therefore occur in clinical routine, which cause two-dimensional registration algorithms, like those proposed by Gilhuijs et al. [29], to fail. Moreover, a visual inspection of the registration result is much easier in object than in projection space.

Considering images reconstructed from a low number of projections, a successful registration relies on sufficient high-contrast information such as from the outline, bones and/or air cavities. A rigid-body registration based on high-contrast structures can be useful to determine the overall patient set-up at the treatment site. The preliminary results on the accuracy obtained in this thesis look quite promising. Nevertheless, the methods need to be investigated more in detail in order to enable their clinical implementation.

The issue of organ motion and deformation has not been addressed. Using a larger number of (kilovoltage) X-ray projections than in this phantom study, however, would offer the opportunity to detect such changes in the patient's anatomy. Furthermore, mutual information matching can be extended to include elastic deformations, see, for example, [11] and references therein. The evaluation of elastic registration tools for their use in image-guided procedures still remains as a challenge for the future.

6.5 Conclusion

Cone-beam computed tomography using open C-arm devices is a promising technique for supporting therapeutic interventions. Three-dimensional image data sets taken directly at the treatment site would be very helpful if considerable organ motion occurs between treatment planning and the actual therapy.

The methods for geometric calibration of X-ray devices and approximate image reconstruction from single-circular cone-beam data sets investigated in this thesis are sufficient for most applications. Further research and careful clinical evaluation, however, is necessary in order to enable image restoration from partial projections in practice. The application of an existing rigid-body registration algorithm to images reconstructed from a relatively low number of cone-beam projections can be considered an encouraging example. Of course, elastic registration needs to be implemented in order to tackle the problem of organ motion mentioned above. For this purpose, more projections and therefore improvement of current C-arm devices is required to enable the reconstruction of images with sufficient soft-tissue contrast.

Chapter 7

Summary

This thesis deals with X-ray transmission computed tomography (CT) from non-ideal projection data sets that do not allow the application of standard image reconstruction methods, such as filtered backprojection. Various specific problems with non-ideal projections were investigated, namely geometric uncertainties due flex effects of the X-ray device, incomplete projections due to technical limitations within the scanning process and inconsistent measurements due to internal organ motion occurring during data acquisition.

The problem of geometric uncertainties was solved by the implementation of a calibration procedure. The technique proposed here is based on the off-line or online scan of a dedicated calibration phantom. In order to achieve high flexibility, the projection geometry is estimated for each view separately considering all degrees of freedom of an arbitrary, linear cone-beam projection. Two different algorithms for the actual estimation were compared using computer simulations. This study shows that the direct calculation of a projection matrix that maps object onto detector coordinates is very accurate. The estimation of geometric parameters (such as the orientation of the detector) does not yield sufficiently accurate results, neither using non-linear optimization nor analytical decomposition of the projection matrix. It was demonstrated, however, that the projection matrix provides all information needed in (filtered) backprojection and reprojection algorithms without explicit decomposition into a set of geometric parameters. The repeatability of flex effects was investigated for a linear accelerator combined with a flat-panel imager. The system was found to behave very reproducibly, thus allowing an off-line calibration, as desired for most applications. This result is specific for the particular system studied. The protocol suggested here, however, can be applied to any cone-beam scanner.

A well-known filtered backprojection algorithm was utilized for approximate image reconstruction from cone-beam projections acquired in a single-circular scan. The algorithm was slightly extended in order to account for geometric calibration information in a computationally efficient way. The feasibility of this approach was demonstrated for two experimental cone-beam scanners employing a linear accelerator and a radiotherapy simulator, respectively, in combination with a flat-panel imager. The spatial resolution achieved with these scanners is about 1.3 mm for high-contrast objects. This value is close to the limit determined by the size of the focal spot in these devices. Artefacts and blurring arising in the images because of geometric flex effects are excellently removed by the method presented in this thesis. The experiments suggest furthermore that artefacts due to incompleteness of the single-circular cone-beam projections and artefacts due to their axial truncation are tolerable for a wide range of medical applications, provided the cone angle does not exceed about $\pm 4°$.

The problem of inconsistent X-ray projections was tackled by the application the method of projections onto convex sets (POCS), which has previously been utilized for image restoration from partial projection data sets and prior knowledge. Computer simulations were carried out in order to evaluate various constraints on the image to be restored. The results of this study show that, in particular, the combination of the additive algebraic reconstruction technique (AART) with an adequate reference image constraint is promising. It was furthermore demonstrated that, in case of spatially limited, internal organ motion, an appropriate reference image can be obtained by standard filtered backprojection of the (minimal) complete set of projections. This approach was applied to diagnostic fan-beam CT data of a human heart. The most consistent subset of the measured projections was determined from the electrocardiogram (ECG) that was recorded synchronously with the CT scan. This example of ECG-correlated heart imaging indicates that the restoration method proposed here is, in principle, capable of reducing artefacts caused by internal organ motion. Further investigation, however, would be required before clinical implementation of this technique.

A phantom study was carried out in order to assess the potential of cone-beam computed tomography using a C-arm device for image-guided procedures. A rigid-body registration of various three-dimensional data sets obtained from the experimental cone-beam scanners performed very well. The uncertainties remaining after matching were about 0.6 mm for translations and $0.5°$ for rotations (single standard deviations).

Appendix A

Mathematical background

The basic mathematical theory of computed tomography is presented more rigorously in the following than in chapter 3 and chapter 4 for the convenience of the reader. Derivations or proofs of the theorems utilized in this thesis, however, are beyond the scope of this brief summary. The reader is referred to standard literature such as [6, 41, 67, 77] for more detailed information on image reconstruction and image restoration from projections.

The theoretical framework is presented for continuous functions of continuous variables for the sake of simplicity. Some important aspects of the implementation of the techniques for discrete image and projection data, however, are discussed in appendix C. As far as possible, the mathematical definitions and theorems are provided for the N-dimensional case, i.e., they apply to two-dimensional as well as three-dimensional computed tomography.

Section A.1 introduces some *assumptions* that apply to the entire appendix. Most of the mathematical theory presented here can be derived for much weaker restrictions. The assumptions utilized here, however, are perfectly adequate for the purpose of this appendix.

Section A.2 defines several *integral transforms* that are important mathematical models in the context of computed tomography. This is quite important, since the definition of even basic operators such as the Fourier transform is not unique in the literature.

Based on these definitions, section A.3 and section A.4 describe methods of *image reconstruction* from complete projection data and *image restoration* from partial projection data using prior information, respectively.

A.1 Basic assumptions

The function $f(\boldsymbol{r})$ denotes the desired spatial distribution of the linear attenuation coefficients (or any other object property). Let $f(\boldsymbol{r})$ be an element of the Hilbert space H (with inner product and norm defined below) consisting of real-valued, square-integrable functions that have compact support within a particular, finite subset Ω of the N-dimensional Euclidian space R^N ($\Omega \subset \mathsf{R}^N$).

A rigorous definition of the Hilbert space H, the N-dimensional Euclidian space R^N and any other mathematical terminology that is not explained here (such as inner product and norm) can be obtained from Bronstein and Semendjajew [10]. Some specific definitions, however, are provided in the following.

Definition A.1. A function $f(\boldsymbol{r})$ is *square-integrable* over R^N if the integral over its squared absolute values exists,

$$\int_{\mathsf{R}^N} |f(\boldsymbol{r})|^2 \, \mathrm{d}^N r < \infty \,. \tag{A.1}$$

Definition A.2. A function $f(\boldsymbol{r})$ is said to exhibit *compact support* within the set Ω if $f(\boldsymbol{r}) = 0 \;\forall\, \boldsymbol{r} \notin \Omega$.

Definition A.3. The *inner product* of two functions $f_1(\boldsymbol{r}), f_2(\boldsymbol{r}) \in \mathsf{H}$ denoted as $\langle f_1(\boldsymbol{r}), f_2(\boldsymbol{r})\rangle$ is defined as the integral over their product,

$$\langle f_1(\boldsymbol{r}), f_2(\boldsymbol{r})\rangle = \int_{\mathsf{R}^N} f_1(\boldsymbol{r})\; f_2(\boldsymbol{r}) \; \mathrm{d}^N r \,. \tag{A.2}$$

The above integral always exists, since the elements of the Hilbert space H are square-integrable and compactly supported in Ω.

Definition A.4. The *norm* of a function $f(\boldsymbol{r})$ in the Hilbert space H is defined as the square-root of the inner product with itself,

$$\|f(\boldsymbol{r})\| = \sqrt{\langle f(\boldsymbol{r}), f(\boldsymbol{r})\rangle} \,. \tag{A.3}$$

The support constraint for $f(\boldsymbol{r})$ introduced above is quite reasonable, since all real objects to be imaged by means of computed tomography are of finite spatial extent. In the literature, the set Ω is often defined as the N-dimensional unit ball $\Omega^N = \{\boldsymbol{r} : \|\boldsymbol{r}\| \leq 1\}$ in order to achieve a convenient notation of some of the derivations and proofs. This does not imply a loss of generality, since each problem can be scaled accordingly.

A.2 Integral transforms

The principle of X-ray computed tomography is to reconstruct an object function $f(\boldsymbol{r})$ from a set of its projections. In the following, three integral transforms modelling the acquisition of projection data are defined. The Fourier transform and its inverse, that play an important role in the theory of computed tomography, are also introduced.

Definition A.5. The *Radon transform* $\mathcal{R}$ maps a function $f(\boldsymbol{r})$ into the set of its integrals over the hyperplanes of the Euclidean space R^N. This can be written as

$$g_{\mathcal{R}}(\hat{\boldsymbol{n}}, s) = \mathcal{R}\, f(\boldsymbol{r}) = \int\limits_{\boldsymbol{r}\cdot\hat{\boldsymbol{n}}=s} f(\boldsymbol{r})\, \mathrm{d}^N r\,, \tag{A.4}$$

where $\hat{\boldsymbol{n}}$ is an element of the unit sphere $\mathsf{S}^{N-1} = \left\{\boldsymbol{r} \in \mathsf{R}^N : \|\boldsymbol{r}\| = 1\right\}$ in R^N, and $s \in \mathsf{R}^1$ is the signed distance of the hyperplane perpendicular to $\hat{\boldsymbol{n}}$ from the origin.[1]

Definition A.6. The *parallel-beam transform* $\mathcal{P}$ maps $f(\boldsymbol{r})$ into the set of its line integrals. More specifically, if $\hat{\boldsymbol{n}} \in \mathsf{S}^{N-1}$ and $\boldsymbol{r} \in \mathsf{R}^N$, then

$$g_{\mathcal{P}}(\hat{\boldsymbol{n}}, \boldsymbol{r}) = \mathcal{P}\, f(\boldsymbol{r}) = \int\limits_{-\infty}^{+\infty} f(\boldsymbol{r} + t\,\hat{\boldsymbol{n}})\, \mathrm{d}t \tag{A.5}$$

is the integral of $f(\boldsymbol{r})$ over the line through $\boldsymbol{r}$ with direction $\hat{\boldsymbol{n}}$. The vector $\boldsymbol{r}$ is normally restricted to the subspace perpendicular to $\hat{\boldsymbol{n}}$, since $g_{\mathcal{P}}(\hat{\boldsymbol{n}}, \boldsymbol{r})$ does not change if $\boldsymbol{r}$ is moved in the direction of $\hat{\boldsymbol{n}}$.

Theorem A.1. The Radon transform $\mathcal{R}$ can be expressed as an integral over the parallel-beam X-ray transform $\mathcal{P}$,

$$\mathcal{R}\, f(\boldsymbol{r}) = g_{\mathcal{R}}(\hat{\boldsymbol{n}}, s) = \int\limits_{\boldsymbol{r}\cdot\hat{\boldsymbol{n}}=s} g_{\mathcal{P}}(\hat{\boldsymbol{n}}, \boldsymbol{r})\, \mathrm{d}^N r\,. \tag{A.6}$$

Radon transform and X-ray transform coincide for $N = 2$, except for the notation of the arguments. In this case, they both model the data acquisition scheme of a first-generation CT scanner.

[1] $f(\boldsymbol{r})$ and $g_{\mathcal{R}}(\hat{\boldsymbol{n}}, s)$ are both of the same dimension N because the direction vector $\hat{\boldsymbol{n}}$, which is an element of the unit sphere, is uniquely determined by $N - 1$ parameters.

Definition A.7. The *divergent-beam transform* $\mathcal{D}$ maps $f(\boldsymbol{r})$ into a set of integrals along the half-line with endpoint $\boldsymbol{a}(\lambda)$ and direction $\hat{\boldsymbol{n}} \in \mathsf{S}^{N-1}$. The parameter $\lambda \in \mathsf{R}^1$ describes the trajectory of the focus $\boldsymbol{a} \in \mathsf{R}^N$. This can be written as

$$g_{\mathcal{D}}(\hat{\boldsymbol{n}}, \lambda) = \mathcal{D} f(\boldsymbol{r}) = \int_0^\infty f(\boldsymbol{a}(\lambda) + t\,\hat{\boldsymbol{n}})\,\mathrm{d}t\,. \tag{A.7}$$

$\mathcal{D}$ is referred to as the *fan-beam transform* and the *cone-beam transform* for $N = 2$ and $N = 3$, respectively. Feasible cone-beam source trajectories $\boldsymbol{a}(\lambda)$ are schematically depicted in figure 3.1 on page 18.

A general formula that relates $\mathcal{D}$ to the Radon transform $\mathcal{R}$ does not exist, since this relation depends on the particular source trajectory. The following necessary and sufficient condition for complete divergent-beam projection data given by Tuy [124], Finch [25], Smith [112] and Grangeat [32] plays an important role in three-dimensional image reconstruction.

Theorem A.2. The Radon transform $\mathcal{R}$ can be completely obtained from the divergent-beam transform $\mathcal{D}$ without analytical continuation if and only if the source trajectory meets every hyperplane that intersects the object at least in one point.

Definition A.8. The N-dimensional *Fourier transform* $\mathcal{F}$ and its inverse $\mathcal{F}^{-1}$ are defined by

$$F(\boldsymbol{\varrho}) = \mathcal{F} f(\boldsymbol{r}) = \int_{\mathsf{R}^N} f(\boldsymbol{r})\,\mathrm{e}^{-2\pi\mathrm{i}\,\boldsymbol{r}\,\boldsymbol{\varrho}}\,\mathrm{d}^N r\,, \tag{A.8}$$

$$f(\boldsymbol{r}) = \mathcal{F}^{-1} F(\boldsymbol{\varrho}) = \int_{\mathsf{R}^N} F(\boldsymbol{\varrho})\,\mathrm{e}^{2\pi\mathrm{i}\,\boldsymbol{r}\,\boldsymbol{\varrho}}\,\mathrm{d}^N \varrho\,. \tag{A.9}$$

Theorem A.3. The Radon transform $\mathcal{R}$, the parallel-beam transform $\mathcal{P}$, the divergent-beam transform $\mathcal{D}$, the Fourier transform $\mathcal{F}$ and its inverse $\mathcal{F}^{-1}$ are *linear*, i.e., $\forall\, f_1(\boldsymbol{r}), f_2(\boldsymbol{r}) \in \mathsf{H}^N$ and $\forall\, c_1, c_2 \in \mathsf{R}^1$

$$\mathcal{T}\big(c_1\, f_1(\boldsymbol{r}) + c_2\, f_2(\boldsymbol{r})\big) = c_1\, \mathcal{T} f_1(\boldsymbol{r}) + c_2\, \mathcal{T} f_2(\boldsymbol{r})\,, \tag{A.10}$$

where $\mathcal{T}$ denotes one of the above transforms.

A.3 Image reconstruction

The previous section shows clearly that image reconstruction in computed tomography is an inverse problem. The desired object function f can be determined from its projections g if the integral transform that defines g is invertible. In the following, some well-known inversion formulae are given for the Radon transform $\mathcal{R}$. The lower index of g referring to the particular integral operator is therefore omitted in order to simplify the notation.

Theorem A.4. The objection function $f(\boldsymbol{r})$ can be obtained by $(N-1)$ partial differentiations of its Radon transform $g(\hat{\boldsymbol{n}}, s)$ with respect to the variable s,

$$g'(\hat{\boldsymbol{n}}, s) = \frac{\partial^{N-1}}{\partial s^{N-1}} g(\hat{\boldsymbol{n}}, s) \ , \tag{A.11}$$

followed by backprojection of the Hilbert transform of the differentiated data $g'(\hat{\boldsymbol{n}}, s)$ over all directions $\hat{\boldsymbol{n}}$,

$$f(\boldsymbol{r}) = \frac{(-1)^{N/2+1}}{(2\pi)^N} \int\limits_{S^{N-1}} \int\limits_{R^1} \frac{g'(\hat{\boldsymbol{n}}, s)}{\boldsymbol{r} \cdot \hat{\boldsymbol{n}} - s} \, \mathrm{d}s \, \mathrm{d}^{N-1}\hat{n} \, . \tag{A.12}$$

These equations are closely related to the *original inversion formula* derived by Radon [93]. They are, however, of limited use for the practical implementation of an image reconstruction algorithm.

Theorem A.5. The one-dimensional Fourier transform of the projection data $g_{\mathcal{R}}(\hat{\boldsymbol{n}}, s)$ with respect to the variable s at a particular direction $\hat{\boldsymbol{n}}$, which is denoted as $G(\hat{\boldsymbol{n}}, \sigma)$, equals the N-dimensional Fourier transform $F(\boldsymbol{\rho})$ of the object function $f(\boldsymbol{r})$ along a line at direction $\hat{\boldsymbol{n}}$ in frequency space,

$$F(\sigma \, \hat{\boldsymbol{n}}) = G(\hat{\boldsymbol{n}}, \sigma) \ . \tag{A.13}$$

This fundamental formula, which is referred to as the *projection theorem*, the *Fourier slice theorem* and the *central slice theorem* in the literature, is the basis for the method of *direct Fourier reconstruction* for two-dimensional parallel-beam projection data.

Theorem A.6. The object function $f(\boldsymbol{r})$ can be obtained by N-dimensional backprojection of the projection data $g(\hat{\boldsymbol{n}}, s)$,

$$\tilde{f}(\boldsymbol{r}) = \int\limits_{S^{N-1}} g(\hat{\boldsymbol{n}}, \boldsymbol{r} \cdot \hat{\boldsymbol{n}}) \ \mathrm{d}^{N-1}\hat{n} \, , \tag{A.14}$$

followed by N-dimensional filtering of the so-called *layergram* $\tilde{f}(\boldsymbol{r})$ with a filter kernel $h(\boldsymbol{r}) = \mathcal{F}^{-1}H(\boldsymbol{\rho})$ to be defined below,

$$f(\boldsymbol{r}) = \int\limits_{\mathsf{R}^N} \tilde{f}(\boldsymbol{r})\ h(\boldsymbol{r'} - \boldsymbol{r})\ \mathrm{d}^N r' = \mathcal{F}^{-1}\, H(\boldsymbol{\rho})\ \mathcal{F}\, \tilde{f}(\boldsymbol{r})\ . \tag{A.15}$$

Applying this theorem immediately to image reconstruction of parallel-beam projections is denoted as *filtered-layergram* method. Before defining the filter kernel, the technique of *filtered backprojection* is introduced in the following theorem.

Theorem A.7. The function $f(\boldsymbol{r})$ can be calculated by one-dimensional filtering of the projections $g(\hat{\boldsymbol{n}}, s)$ with respect to the variable s employing a kernel $h(s) = \mathcal{F}^{-1}\, H(\sigma)$ to be defined later,

$$g'(\hat{\boldsymbol{n}}, s) = \int\limits_{-\infty}^{+\infty} g(\hat{\boldsymbol{n}}, s)\ h(s' - s)\ \mathrm{d}s' = \mathcal{F}^{-1}\, H(\sigma)\ \mathcal{F}\, g(\hat{\boldsymbol{n}}, s)\ , \tag{A.16}$$

and N-dimensional backprojection of the filtered projections $g'(\hat{\boldsymbol{n}}, s)$ over all directions $\hat{\boldsymbol{n}}$,

$$f(\boldsymbol{r}) = \int\limits_{\mathsf{S}^{N-1}} g'(\hat{\boldsymbol{n}}, \boldsymbol{r}\cdot\hat{\boldsymbol{n}})\ \mathrm{d}^{N-1}\hat{n}\,. \tag{A.17}$$

The frequency spectrum of the one-dimensional *filter kernel* omitted in the previous theorem is given by

$$H(\sigma) = w\left(\frac{\sigma}{\sigma_{\mathrm{max}}}\right)\ \mathrm{rect}\left(\frac{\sigma}{\sigma_{\mathrm{max}}}\right)\ |\sigma|\,. \tag{A.18}$$

The N-dimensional filter $H(\boldsymbol{\rho})$ employed in equation (A.15) equals the one-dimensional filter introduced in equation (A.18) along all lines through the origin, i.e., for $\sigma = \|\boldsymbol{\rho}\|$. The introduction of the ideal low-pass filter

$$\mathrm{rect}(\hat{\sigma}) = \begin{cases} 1 & \text{if} \quad |\hat{\sigma}| \leq 1\,, \\ 0 & \text{if} \quad |\hat{\sigma}| > 1 \end{cases} \tag{A.19}$$

is necessary for the existence of the inverse Fourier transform in equation (A.16) and (A.15), respectively, because the Fourier transform of the projections $G(\hat{\boldsymbol{n}}, \sigma) = \mathcal{F}\, g(\hat{\boldsymbol{n}}, s)$ cannot vanish strictly (unless they are zero everywhere). This follows from the assumption that $f(\boldsymbol{r})$ exhibits compact

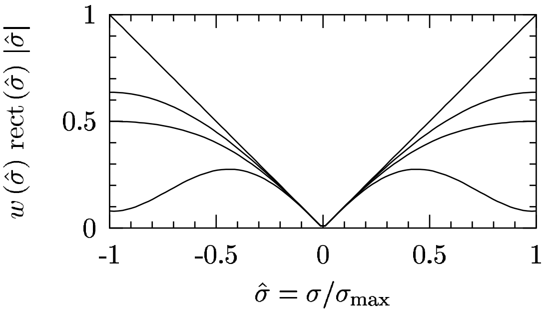

$$
\begin{aligned}
w_{\mathrm{RL}}(\hat{\sigma}) &= 1 \\
w_{\mathrm{SL}}(\hat{\sigma}) &= \mathrm{sinc}\left(\frac{\pi}{2}\,\hat{\sigma}\right) \\
w_{\mathrm{BW}}(\hat{\sigma}) &= \frac{1}{1+\hat{\sigma}^{2k}}\,, \quad k = 1, 2, \ldots \\
w_{\mathrm{GH}}(\hat{\sigma}) &= \nu + (1-\nu)\cos(\pi\,\hat{\sigma})\,, \\
& \quad 0.5 \le \nu \le 1
\end{aligned}
$$

Figure A.1: Ramp filter for image reconstruction regularized by various window functions. From top to bottom, the window proposed by Ramachandran and Lakshminarayanan (RL), the window suggested by to Shepp and Logan (SL), the Butterworth (BW) window for $k = 1$ and the generalized Hamming (GH) window for $\nu = 0.54$ are considered. The GH window is denoted as Hamming window for $\nu = 0.54$ and as Hanning window for $\nu = 0.5$.

support and from the definition of the Radon transform.[2] This regularization is furthermore sufficient for the calculation of the real-space filter kernels $h(\boldsymbol{r})$ and $h(s)$, which also involves an inverse Fourier transform.

The projections, however, are assumed to be *essentially band-limited* with bandwidth σ_{max}, i.e., $G(\hat{\boldsymbol{n}}, \sigma)$ is negligible for $\sigma > \sigma_{\mathrm{max}}$. Essentially band-limited functions admit similar mathematical interpretation as strictly band-limited functions.[3] Theorem A.6 and theorem A.7 are valid in this sense.

Furthermore, various *window functions* $w(\hat{\sigma})$ have been utilized in order to control the tradeoff between spatial resolution and noise propagation directly within the image reconstruction procedure. Some of the standard windows are depicted in figure A.1, which also provides their mathematical definitions.

The Radon inversion formulae presented above may be sufficient for a short introduction into the basic principles of image reconstruction from projections. The numerous methods that have been derived to invert the fan-beam and the cone-beam transform are not presented here. Details on the approximate cone-beam reconstruction technique proposed by Feldkamp, Davis and Kress [24], however, are provided in section 4.5.

[2]For this reason, the reconstruction of finite images is only approximate, even if a complete, continuous projection data set without any noise was available.

[3]In real computed tomography applications, this essential band-limitation comes quite naturally from the finite detector pixel size.

A.4 Image restoration

This section sketches the theory of *projections onto convex sets* (POCS) that is employed for image restoration from incomplete projection data and a priori information. The general idea of POCS is as follows.

Every known property of the unknown object function $f(\boldsymbol{r}) \in \mathsf{H}$ restricts it to lie in some set $\mathsf{C}_k \subset \mathsf{H}$. These *constraint sets* are assumed to be closed and convex.

Definition A.9. A subset C of H is said to be *closed* if it contains all limit elements of sequences $\left\{f^{(t)}(\boldsymbol{r})\right\}$ existing for $t = 0, 1, 2, \ldots$, $f^{(t)}(\boldsymbol{r}) \in \mathsf{C}$ and $f^{(t)}(\boldsymbol{r}) \neq f^{(0)}(\boldsymbol{r})$.

Definition A.10. A subset C of H is said to be *convex* if, together with two arbitrary elements $f_1(\boldsymbol{r})$ and $f_2(\boldsymbol{r})$, it contains also their linear combination $\lambda f_1(\boldsymbol{r}) + (1-\lambda)\, f_2(\boldsymbol{r})$ for all $0 \leq \lambda \leq 1$.

Then for K known properties of the desired object function $f(\boldsymbol{r})$, there are K closed, convex sets C_k, and $f(\boldsymbol{r})$ must lie in their intersection

$$\mathsf{C} = \bigcap_{k=1}^{K} \mathsf{C}_k\,, \tag{A.20}$$

provided C is not empty, i.e., all constraints are consistent. The problem is now to find an $f(\boldsymbol{r}) \in \mathsf{C}$ given the constraints C_k. For this purpose, *constraint operators* $\mathcal{C}_k$ are defined that project[4] a function $f(\boldsymbol{r})$ onto the nearest neighbour $f_k(\boldsymbol{r})$ in C_k,

$$f_k(\boldsymbol{r}) = \mathcal{C}_k\, f(\boldsymbol{r})\ ,\ \min_{f'(\boldsymbol{r}) \in \mathsf{C}_k} \|f(\boldsymbol{r}) - f'(\boldsymbol{r})\| = \|f(\boldsymbol{r}) - f_k(\boldsymbol{r})\|\,. \tag{A.21}$$

The assumption of closed and convex sets C_k guarantees that there exist unique nearest neighbours $f_k(\boldsymbol{r})$.

The desired function $f(\boldsymbol{r})$ could be, in principle, restored in one step by application of the constraint operator $\mathcal{C}$ corresponding to the intersection set C. The operator $\mathcal{C}$, however, is often difficult to derive from the C_k analytically. An iterative restoration procedure is therefore employed in practice that is based on the following important theorem.

[4] The application of such constraint operators is referred to as 'projections' in the theory of POCS. This term is not used in the following in order to avoid potential confusion with the measured projections of an object to be restored.

Theorem A.8. Let there be K closed and convex sets $\mathsf{C}_k \subset \mathsf{H}$. Let $\mathcal{C}_k$ be the constraint operators that map an arbitrary element of H onto its nearest neighbours (in the sense of the norm) within the C_k. Let furthermore be $\mathcal{C}'_k = \mathcal{I} + \lambda_k \left(\mathcal{C}_k - \mathcal{I}\right)$, where $\mathcal{I}$ is the identity operator and $0 < \lambda_k < 2$. The sequence $\left\{f^{(t)}\left(\boldsymbol{r}\right)\right\}$ with $f^{(0)}\left(\boldsymbol{r}\right) \in \mathsf{H}$ defined by

$$f^{(t+1)}\left(\boldsymbol{r}\right) = \mathcal{C}'_K \, \mathcal{C}'_{K-1} \, \ldots \, \mathcal{C}'_1 \, f^{(t)}\left(\boldsymbol{r}\right) \tag{A.22}$$

converges weakly (to be defined below) to an element $f\left(\boldsymbol{r}\right)$ that lies within the intersection C of all sets C_k for $t \to \infty$. The sequence of normed errors $\|f^{(t)}\left(\boldsymbol{r}\right) - f\left(\boldsymbol{r}\right)\|$ is non-increasing with t.

The λ_k referred to as *relaxation parameters* can be adjusted within the above limits in order to control the tradeoff between convergence speed and accuracy of the iterative procedure.

Definition A.11. The sequence $\left\{f^{(t)}\left(\boldsymbol{r}\right)\right\}$ is said to *converge weakly* to $f\left(\boldsymbol{r}\right)$ if for every $f'\left(\boldsymbol{r}\right) \in \mathsf{H}$

$$\lim_{t\to\infty} \langle f^{(t)}\left(\boldsymbol{r}\right), f'\left(\boldsymbol{r}\right)\rangle = \langle f\left(\boldsymbol{r}\right), f'\left(\boldsymbol{r}\right)\rangle \,. \tag{A.23}$$

The sequence $\left\{f^{(t)}\left(\boldsymbol{r}\right)\right\}$ is said to *converge strongly* to $f\left(\boldsymbol{r}\right)$ if

$$\lim_{t\to\infty} \|f^{(t)}\left(\boldsymbol{r}\right) - f\left(\boldsymbol{r}\right)\| = 0 \,. \tag{A.24}$$

Theorem A.9. For every Hilbert space H, strong convergence of a sequence implies weak convergence of this sequence. The converse is true if and only if H is a finite-dimensional linear vector space.

Practical constraints that have been utilized to force consistency of the object function $f\left(\boldsymbol{r}\right)$ with the measured projection data and prior knowledge are described in section 4.6. The proof that these constraints are closed and convex was given previously [83, 139]. The reference image constraint (such as defined in this thesis) is investigated in the following theorems because it is not considered in the publications cited above.

Theorem A.10. The set $\mathsf{C}_{\check{f}} = \left\{f\left(\boldsymbol{r}\right) : |f\left(\boldsymbol{r}\right) - \check{f}\left(\boldsymbol{r}\right)| \leq \varepsilon\left(\boldsymbol{r}\right), \varepsilon\left(\boldsymbol{r}\right) > 0\right\}$ is closed (in the sense of definition A.9).

Proof. Let $\left\{f^{(t)}\left(\boldsymbol{r}\right)\right\}$ be a sequence of elements contained in the set $\mathsf{C}_{\check{f}}$, and let $f\left(\boldsymbol{r}\right)$ be the strong limit of this sequence,

$$L = \lim_{t\to\infty} \|f^{(t)}\left(\boldsymbol{r}\right) - f\left(\boldsymbol{r}\right)\| = \lim_{t\to\infty} \int\limits_{\Omega} \left(f^{(t)}\left(\boldsymbol{r}\right) - f\left(\boldsymbol{r}\right)\right)^2 \, \mathrm{d}^N r = 0 \,. \tag{A.25}$$

Assume there would exist a subset $\Theta \subseteq \Omega$ in which $f(\boldsymbol{r}) - \check{f}(\boldsymbol{r}) < \varepsilon(\boldsymbol{r})$ or $f(\boldsymbol{r}) - \check{f}(\boldsymbol{r}) > \varepsilon(\boldsymbol{r})$, i.e., it would be $f(\boldsymbol{r}) \notin \mathsf{C}_{\check{f}}$. In this case,

$$L = \lim_{t\to\infty} \int\limits_{\Omega-\Theta} \left(f^{(t)}(\boldsymbol{r}) - f(\boldsymbol{r})\right)^2 \mathrm{d}^N r + \lim_{t\to\infty} \int\limits_{\Theta} \left(f^{(t)}(\boldsymbol{r}) - f(\boldsymbol{r})\right)^2 \mathrm{d}^N r \,, \tag{A.26}$$

where the second term is larger than zero, which is obvious when writing

$$f^{(t)}(\boldsymbol{r}) - f(\boldsymbol{r}) = \left(f^{(t)}(\boldsymbol{r}) - \check{f}(\boldsymbol{r})\right) - \left(f(\boldsymbol{r}) - \check{f}(\boldsymbol{r})\right) . \tag{A.27}$$

If the second term in equation (A.26) is larger than zero, then also $L > 0$, which contradicts the definition of $f(\boldsymbol{r})$ in equation (A.25). Therefore, a function $f(\boldsymbol{r})$ that is not contained in the set $\mathsf{C}_{\check{f}}$ cannot be a strong limit of the sequence $\left\{f^{(t)}(\boldsymbol{r})\right\}$. This completes the proof that $\mathsf{C}_{\check{f}}$ is closed. $\square$

Theorem A.11. The set $\mathsf{C}_{\check{f}} = \left\{f(\boldsymbol{r}) : |f(\boldsymbol{r}) - \check{f}(\boldsymbol{r})| \leq \varepsilon(\boldsymbol{r}) \,, \varepsilon(\boldsymbol{r}) > 0\right\}$ is convex (in the sense of definition A.10).

Proof. Let $f_1(\boldsymbol{r})$ and $f_2(\boldsymbol{r})$ two arbitrary functions that are contained in the set $\mathsf{C}_{\check{f}}$. Furthermore, let λ be an arbitrary scalar factor with $0 \leq \lambda \leq 1$ and

$$f(\boldsymbol{r}) = \lambda\, f_1(\boldsymbol{r}) + (1-\lambda)\; f_2(\boldsymbol{r}) \,. \tag{A.28}$$

Then the distance $\varepsilon'(\boldsymbol{r}) = |f(\boldsymbol{r}) - \check{f}(\boldsymbol{r})|$ of $f(\boldsymbol{r})$ from the reference image $\check{f}(\boldsymbol{r})$ is given by

$$\begin{aligned} \varepsilon'(\boldsymbol{r}) &= |\lambda\, f_1(\boldsymbol{r}) + (1-\lambda)\; f_2(\boldsymbol{r}) - \check{f}(\boldsymbol{r})| && \text{(A.29)} \\ &= |\lambda\, f_1(\boldsymbol{r}) - \lambda\, \check{f}(\boldsymbol{r}) + (1-\lambda)\; f_2(\boldsymbol{r}) - (1-\lambda)\; \check{f}(\boldsymbol{r})| \,. && \text{(A.30)} \end{aligned}$$

Using the triangle inequality results in

$$\varepsilon'(\boldsymbol{r}) \leq \lambda\, |f_1(\boldsymbol{r}) - \check{f}(\boldsymbol{r})| + (1-\lambda)\; |f_2(\boldsymbol{r}) - \check{f}(\boldsymbol{r})| \,. \tag{A.31}$$

Since $f_1(\boldsymbol{r})$ and $f_2(\boldsymbol{r})$ are elements of $\mathsf{C}_{\check{f}}$, their distance from the reference image such as occurring in the above equation is equal or smaller than $\varepsilon(\boldsymbol{r})$. This yields $\varepsilon'(\boldsymbol{r}) \leq \varepsilon(\boldsymbol{r})$ and therefore $f(\boldsymbol{r}) \in \mathsf{C}_{\check{f}}$. $\square$

Appendix B

Analytical phantoms

The assessment of the efficacy of reconstruction algorithms is often based on mathematical phantoms. Computer simulations offer the opportunity to investigate various phenomena such as photon statistics and beam hardening independently, which cannot be separated physically in real measurements.

There are basically two methods for simulating X-ray projections.

1. The phantom is represented as voxel model. The projections are then calculated by ray tracing through the discrete volume. To avoid undesired aliasing effects in the simulation, the phantom voxels should be significantly smaller than the detector pixels [30].

2. The phantom is represented as continuous function. The line integrals through the phantom comprising an X-ray projection are then calculated analytically.

The first technique is very flexible for handling arbitrary phantoms. In this thesis, however, the second method was chosen to compute the projections because it avoids discretization errors. The phantoms considered here are composed by superposition of homogeneous ellipsoids. This approach, which has been widely used, is sufficient for most theoretical investigations.

Section B.1 describes the calculation of line integrals through ellipsoids. The simulation of photon statistics and poly-energetic beams is explained in section B.2. Compton scattering is not considered. This effect could be simulated by a convolution of the projection data with a scatter kernel as proposed in [41]. For more complex phantoms, however, the generation of phantom projections by Monte Carlo would be preferable. Section B.3 provides the parameters of the phantoms employed in this thesis.

B.1 Calculation of line integrals

Due to the linearity of the cone-beam transform (see theorem A.3), line integrals can be calculated for each ellipsoid separately.

Let $\boldsymbol{r}$ be an arbitrary vector in a coordinate system that is aligned with respect to a particular ellipsoid, i.e., its origin is located at the centre and its axes are in agreement with the half axes A, B, C of this ellipsoid. Furthermore, let be $\boldsymbol{E} = \left(A^{-2}, B^{-2}, C^{-2}\right) \boldsymbol{I}$, where $\boldsymbol{I}$ is the identity matrix. Using these definitions, the ellipsoid with linear attenuation coefficient μ is represented by the object function

$$f(\boldsymbol{r}) = \begin{cases} \mu & \text{if } \left(\boldsymbol{r}^{\mathrm{T}} \boldsymbol{E}\, \boldsymbol{r}\right)^2 \leq 1\,, \\ 0 & \text{otherwise.} \end{cases} \tag{B.1}$$

Let $\boldsymbol{T}$ be a 4×4 transformation matrix that maps the coordinates of $\boldsymbol{r} = (x, y, z)^{\mathrm{T}}$ with respect to the ellipsoid system onto object coordinates as defined previously. $\boldsymbol{T}$ is composed of a translation and three rotations to account for the position and the orientation of the ellipsoid with respect to the object coordinate system. For a particular view at angle α, the cone-beam geometry is given by the projection matrix $\boldsymbol{P}_\alpha$ that maps object onto detector coordinates; see subsection 4.1.3 for further details. The mapping from ellipsoid coordinates onto detector coordinates is then given by

$$\lambda\, (u, v, 1)^{\mathrm{T}} = \left(\boldsymbol{P}_\alpha \boldsymbol{T}\right) (x, y, z, 1)^{\mathrm{T}}\,. \tag{B.2}$$

For a flat-panel imager, the normalization of the detector coordinates can be directly considered in the above formula as explained in appendix C.

The position $\boldsymbol{r}_{\mathrm{foc}}$ of the focus and the unit vector $\hat{\boldsymbol{r}}_{\alpha,u,v}$ pointing from the focus to the point $(u, v)^{\mathrm{T}}$ on the detector are obtained from $\left(\boldsymbol{P}_\alpha \boldsymbol{T}\right)$ according to equation (4.13) and (4.26), respectively. Provided the focus and the point $(u, v)^{\mathrm{T}}$ are located outside of the ellipsoid, the desired line integral can be calculated by

$$g(\alpha, u, v) = \begin{cases} 2\,\mu \sqrt{q(\alpha, u, v)} & \text{if } q(\alpha, u, v) \geq 0\,, \\ 0 & \text{otherwise,} \end{cases}$$
$$\text{where} \quad q(\alpha, u, v) = \left(\frac{\hat{\boldsymbol{r}}^{\mathrm{T}}_{\alpha,u,v} \boldsymbol{E}\, \boldsymbol{r}_{\mathrm{foc},\alpha}}{\hat{\boldsymbol{r}}^{\mathrm{T}}_{\alpha,u,v} \boldsymbol{E}\, \hat{\boldsymbol{r}}_{\alpha,u,v}}\right)^2 + \frac{\boldsymbol{r}^{\mathrm{T}}_{\mathrm{foc},\alpha} \boldsymbol{E}\, \boldsymbol{r}_{\mathrm{foc},\alpha} - 1}{\hat{\boldsymbol{r}}^{\mathrm{T}}_{\alpha,u,v} \boldsymbol{E}\, \hat{\boldsymbol{r}}_{\alpha,u,v}}\,. \tag{B.3}$$

The analytically exact line integration provided here exhibits significant deviations from the approximation in [49], especially for those lines that intersect an ellipsoid close to its edge. These deviations may even result in different assessments of cone-beam artefacts based on phantom data.

The integration of equation (B.3) over the finite pixel size, however, is impractical to implement. The data acquisition process is therefore simulated by averaging multiple line integrals within each detector pixel.

B.2 Simulation of photon statistics

The simulation of the quantum character of X-rays is based on the following theorem, which is proved, for example, in [41].

Theorem B.1. Let $N_0\,(E;\alpha,u,v)$ denote the average number of photons at energy E that are emitted by a stable X-ray source along a line from the focus at view angle α to the point (u,v) on the detector in one unit of time. Let $t\,(E;\alpha,u,v)$ be the transmittance of the material between the focus and the detector position (u,v) at energy E. Let $\eta\,(E)$ denote the efficiency of the detector at energy E. The number of photons at energy E which reach the point (u,v) without having been absorbed or scattered and are counted by the detector in one unit of time is a sample of a Poisson random variable with parameter $\eta\,(E)\;N_0\,(E;\alpha,u,v)\;t\,(E;\alpha,u,v)$.

The transmittance $t\,(E;\alpha,u,v)$ is obtained from the line integral $g\,(E;\alpha,u,v)$ calculated previously for a particular energy E by

$$t\,(E;\alpha,u,v) = \exp\bigl(-g\,(E;\alpha,u,v)\bigr)\,. \tag{B.4}$$

The signal $I\,(E;\alpha,u,v)$ that is detected is then drawn from a Poisson distribution with the above parameter using the implementation described in [92]. The effective source fluence is estimated for a specific dose according to the conversion factors provided in [97].

The method is capable of simulating poly-energetic X-ray beams. The calculations described above are then carried out for different, discrete energy levels, considering the energy spectrum of the primary beam and the energy-dependent efficiency of the detector. Using such polychromatic phantom data, the effect of beam hardening can be investigated.

B.3 Phantom specifications

The two-dimensional phantom proposed by Shepp and Logan [49], which models a transverse head section, is specified in table B.1 and depicted in figure B.1. This quasi-standard phantom has been widely used in the literature for demonstrating the performance of image reconstruction and image restoration algorithms on ideal, low-contrast data. In various publications, however, the parameters vary slightly.

Number	Centre coordinates		Axis lengths		Tilt	Attenuation
	x	y	A	B	ϕ [deg]	μ/μ_{water}
1	0.0	0.0	0.69	0.92	0.0	2.00
2	0.0	−0.0184	0.6624	0.874	0.0	−0.98
3	0.22	0.0	0.31	0.11	−72.0	−0.02
4	−0.22	0.0	0.41	0.16	72.0	−0.02
5	0.0	0.35	0.21	0.25	0.0	0.01
6	0.0	−0.1	0.046	0.046	0.0	0.01
7	0.0	0.1	0.046	0.046	0.0	0.01
8	−0.08	−0.605	0.046	0.023	0.0	0.01
9	0.06	−0.605	0.023	0.046	0.0	0.01
10	0.0	−0.605	0.023	0.023	0.0	0.01

Table B.1: Parameters of the two-dimensional head phantom. Lengths are given in arbitrary units. The attenuation coefficients resulting from a superposition of all shapes are normalized to the attenuation coefficient of water.

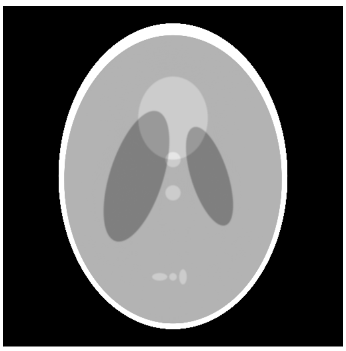

Figure B.1: Two-dimensional phantom suggested by Shepp and Logan. The attenuation range $[0.95, 1.05]$ is linearly scaled to the grey levels available.

Figure B.2 shows a 'water disc' phantom, which is formally defined in table B.2. This phantom comprises 7 circular inserts that represent typical average attenuation coefficients of various tissue types. These value refer (relative to water) to lung (0.25), fat (0.91), pancreas (1.04), heart (1.05), liver (1.06), spongy bone (1.13) and compact bone (1.80). The disc phantom can be used for quantitative simulations considering the photon statistics if the normalized attenuation coefficients are multiplied with the attenuation coefficient of water at a particular energy.

Corresponding tissue type	Centre coordinates x [cm]	y [cm]	Axis lengths A [cm]	B [cm]	Tilt ϕ [deg]	Attenuation μ/μ_{water}
water	0.00	0.00	15.0	15.0	0.0	1.00
lung	0.00	−9.00	3.0	3.0	0.0	−0.75
fat	7.04	−5.61	3.0	3.0	0.0	−0.09
pancreas	8.77	2.00	3.0	3.0	0.0	0.04
heart	3.90	8.11	3.0	3.0	0.0	0.05
liver	−3.90	8.11	3.0	3.0	0.0	0.06
spongy bone	−8.77	2.00	3.0	3.0	0.0	0.13
compact bone	−7.04	−5.61	3.0	3.0	0.0	0.80

Table B.2: Parameters of the two-dimensional water disc phantom. The attenuation coefficients normalized to the attenuation coefficient to water are (after superposition of the shapes) typical average values for the tissue types listed in the left column.

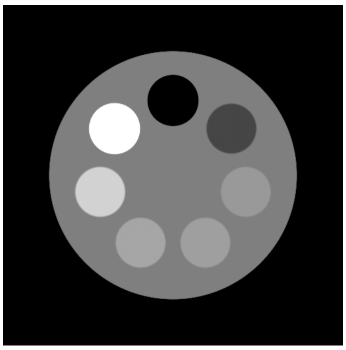

Figure B.2: Two-dimensional water disc phantoms. The seven circular inserts represent lung (0.25), fat (0.91), pancreas (1.04), heart (1.05), liver (1.06), spongy bone (1.13) and compact bone (1.80), clockwise from 12 o'clock. The values in the brackets are the attenuation coefficients normalized to those of water. The grey-scale range is $[0.8, 1.2]$.

Appendix C

Implementation details

In chapter 4, the methods utilized in this thesis are described mathematically based on continuous variables. This appendix provides some details on the efficient practical implementation of the algorithms for discrete data. For a convenient notation, all sampling indices are defined one-based. Zero-based indexing, which might be preferable for a practical computer program, would cause only minor and obvious changes to the algorithms and equations. The following notation is utilized throughout this appendix.

Let $f[i, j, k]$ be a three-dimensional array that stores $I \times J \times K$ samples of the image $f(x_i, y_j, z_k)$ to be reconstructed. The sampling steps Δx, Δy and Δz are assumed to be constant to enable efficient implementations.

Let $g[l, m, n]$ be a three-dimensional array that stores L projections, each of them comprising $M \times N$ samples $g(\alpha_l, u_m, v_n)$ or $g(\alpha_l, \beta_m, v_n)$ for planar or cylindrical detectors, respectively. $g[l, m^*]$ refers to the projections as one-dimensional vectors concatenating all detector rows. The constant sampling steps within each projection are denoted as $\Delta\beta$, Δu and Δv. The view angles α_l are not required to be equally spaced. Although the view index l is always written explicitly, the projections are processed independently whenever possible to decrease the memory load.

Section C.1 explains the normalization of continuous coordinates to obtain the corresponding array indices. The implementation of pre-weighting and filtering of the projections is demonstrated in section C.2. Various back-projection algorithms are introduced section C.3 and discussed concerning their computational efficiency. Section C.4 mentions a few aspects regarding the implementation of reprojection algorithms such as required for iterative reconstruction techniques.

C.1 Normalization of coordinates

Normalized detector coordinates that consider the discretization of the projections are denoted as $\hat{\beta}$, $\hat{u}$ and $\hat{v}$. They are treated as continuous variables, but their integral part refers to the corresponding pixel indices,

$$m = \lfloor \hat{u} \rfloor \quad \text{or} \quad m = \lfloor \hat{\beta} \rfloor \quad \text{and} \quad n = \lfloor \hat{v} \rfloor \,. \tag{C.1}$$

For *flat detectors*, the normalization of the detector coordinates u, v can be considered within the projection matrix such that

$$\lambda \, (\hat{u}, \hat{v}, 1)^{\mathrm{T}} = \hat{\boldsymbol{P}} \, (x, y, z, 1)^{\mathrm{T}} \;, \quad \hat{\boldsymbol{P}} = \boldsymbol{E}^{-1} \, \boldsymbol{P} \,, \quad \boldsymbol{P} = \boldsymbol{E} \, \hat{\boldsymbol{P}} \,, \tag{C.2}$$

where

$$\boldsymbol{E} = \begin{pmatrix} \Delta u & 0 & u_0 \\ 0 & \Delta v & v_0 \\ 0 & 0 & 1 \end{pmatrix} \,, \quad \boldsymbol{E}^{-1} = \begin{pmatrix} \Delta u^{-1} & 0 & -u_0 \, \Delta u^{-1} \\ 0 & \Delta v^{-1} & -v_0 \, \Delta v^{-1} \\ 0 & 0 & 1 \end{pmatrix} \,. \tag{C.3}$$

The matrix $\boldsymbol{E}$ is definitely invertible, since the pixel pitch along both detector axis is positive, i.e., $\Delta u > 0$ and $\Delta v > 0$. The offsets for one-based indexing of the detector matrix are

$$u_0 = -\tfrac{1}{2} \, (M + 1) \; \Delta u \quad \text{and} \quad v_0 = -\tfrac{1}{2} \, (N + 1) \; \Delta v \,. \tag{C.4}$$

The normalization of the projection matrices enables efficient implementations of backprojection and reprojection algorithms to be discussed below. The normalized matrices can be also used in the calculation of line integrals through analytic phantoms described in section B.1 in quite a similar manner.

The normalized projection matrix $\hat{\boldsymbol{P}}$ can be calculated directly by the geometric calibration procedure described in section 4.4 if the positions of the markers in the projections are measured in terms of normalized detector coordinates.

For the decomposition algorithm explained in subsection 4.1.4, the original projection matrix $\boldsymbol{P}$ has to be used. If $\hat{\boldsymbol{P}}$ is given, the normalization has to be reversed before according to equation (C.2). The pixel pitch values Δu, Δv as well as the offsets u_0, v_0 are then assumed to be known with sufficient accuracy. They are, however, not independent of the geometric parameters D, u_{foc}, v_{foc} to be considered in the decomposition.

For *cylindrical detectors*, the coordinate v is handled as described above, but the fan-angle β needs to be calculated separately according to equation (4.1). The normalization is given by

$$\hat{\beta} = \frac{\beta - \beta_0}{\Delta\beta}\,, \tag{C.5}$$

where the offset for one-based indexing is

$$\beta_0 = -\tfrac{1}{2}\,(M + 1 + a)\,\Delta\beta\,, \quad a \in \left\{-\tfrac{1}{4}, 0, \tfrac{1}{4}\right\}\,. \tag{C.6}$$

The introduction of a non-zero alignment a is one way to fulfil the Nyquist condition for sufficient sampling of the projection rays; see subsection 4.2.1 for further explanation.

In practice, the mapping from u into $\hat{\beta}$ by successive application of equation (4.1) and (C.5) is often implemented by means of a single look-up table in order to save computation time.

For the use within voxel-driven backprojection algorithms, such as introduced in section C.3, the projection matrix is normalized using the equation

$$\hat{\boldsymbol{P}} = \boldsymbol{E}^{-1}\left(\frac{1}{p_{34}}\boldsymbol{P}\right)\boldsymbol{T}\,, \tag{C.7}$$

where $\boldsymbol{T}$ is a 4×4 matrix that maps the voxel indices i, j, k onto the corresponding object coordinates x_i, y_j, z_k. The element-wise division of the original projection matrix by p_{34} is necessary to obtain the backprojection weights efficiently as shown in equation (4.28).

For a reconstruction grid comprising $I \times J \times K$ voxels at pitch values Δx, Δy, Δz that is aligned and centred with respect to the object coordinate system, the mapping $\boldsymbol{T}$ is given by

$$\boldsymbol{T} = \begin{pmatrix} \Delta x & 0 & 0 & -\frac{1}{2}\,(I+1)\,\Delta x \\ 0 & \Delta y & 0 & -\frac{1}{2}\,(J+1)\,\Delta y \\ 0 & 0 & \Delta z & -\frac{1}{2}\,(K+1)\,\Delta z \\ 0 & 0 & 0 & 1 \end{pmatrix}\,. \tag{C.8}$$

Any desired rotations and offsets, however, can be considered in the definition of the matrix $\boldsymbol{T}$.

C.2 Weighting and filtering

The implementation of the *projection data weighting* operations is straightforward from a discretization of equation (4.42), (4.45), (4.48) and (4.49). The weights, which vary only in one or two dimensions, can be pre-calculated and stored in corresponding arrays if flex effects do not need to be considered.

The one-dimensional *filtering of the projections* along their rows in equation (4.43) and equation (4.46) can be implemented as discrete convolution,

$$g_2\,[l,m,n] = \sum_{m'=-M}^{M} g_1\,[l,m',n]\;h\,[m-m']\;, \tag{C.9}$$

where $h\,[m]$ stores the coefficients of the discretized filter kernel $h\,(m\,\Delta u)$ or $h\,(m\,\Delta\beta)$, respectively. The convolution sum has, of course, to be truncated to account for the finite length of the arrays. This is omitted for the sake of simplicity in the above formula.

Using the convolution theorem, the filtering step for each detector row can also be implemented in frequency space. In this case, the one-dimensional fast Fourier transform (FFT) of the projection data is first calculated. The actual filtering is then a multiplication with the (analytically pre-calculated) discretized spectrum of the filter kernel. The filtered row is finally obtained by an inverse FFT. This approach, however, requires excessive zero-padding of the input data in order to avoid cyclic convolution.

C.3 Backprojection

Algorithm C.1 describes the implementation of the cone-beam backprojection. The algorithm works voxel-driven, i.e., for each voxel within the field of view, the contributions from each projection considering the distance weight are calculated successively. The projections are processed independently while all contributions are summed into the image array $f\,[i,j,k]$. This algorithm is based on the method by Wiesent et al. [133, 134], but it handles the distance weight in a computationally more efficient way.

The innermost loop of algorithm C.1 comprises four additions, seven multiplications and one division except the calculation of $\tilde{g}$, which is discussed below. The division $1/z_1$ can be realized by a look-up table if fixed-point arithmetic is used. The access of the image array can be considered one-dimensional, since only the index i changes within the innermost loop.

The number of multiplications can be reduced to four as shown in algorithm C.2, provided the successive incrementation of the x, y, z values is sufficiently accurate. Further optimizations such as, for example, the removal of the division from the innermost loop, are possible for ideal cone-beam geometries. Such optimizations, however, are not generally applicable when geometric flex effects need to be accounted for. They are therefore not explained here.

Two-dimensional fan-beam backprojection is a special case of algorithm C.1 or C.2, in which $\hat{\boldsymbol{P}}$ is only a 2×3 matrix. The number of operations is then reduced correspondingly. For parallel-beam backprojection, z_1 is always unity, i.e., the division and four multiplications can be removed.

In algorithms C.1 and C.2, the valid range of voxels $[i_{\min}, i_{\max}]$ within a image row j, k is calculated separately for each projection. Alternatively, look-up tables $i_{\min}[j,k]$ and $i_{\max}[j,k]$ could be pre-calculated in order to process only those voxels that are within the field of view in all projections.

Algorithm C.3 shows the estimation of the contribution from each projection by bilinear interpolation such as usually employed in voxel-driven backprojection techniques. For cylindrical detectors, this algorithm has to be extended by an additional access of a pre-calculated look-up table in order to obtain the index m as discussed above.

Nearest-neighbour interpolation such as shown in algorithm C.4 is normally not sufficient if high-quality images are desired. However, the projections can be pre-interpolated onto a finer grid prior to backprojection in order to apply then a nearest-neighbour interpolation. A computationally efficient implementation of this *stretching method* was presented by Peters [90]. The normalization of the projection matrix in equation C.7 has to be replaced by

$$\hat{\boldsymbol{P}} = \begin{pmatrix} 1 & 0 & 0 \\ 0 & M & -M \\ 0 & 0 & 1 \end{pmatrix} \boldsymbol{E}^{-1} \left(\frac{1}{p_{34}} \boldsymbol{P} \right) \boldsymbol{T} \tag{C.10}$$

in order to be utilized with algorithm C.4. The leftmost, additional normalization matrix accounts for the one-dimensional access of the projections by the index m^*. This efficient form of projection data access cannot be applied to bilinear interpolation, since in this case the normalized detector coordinates are needed (rather than an array index) to calculate the interpolation weights. From this point of view, the stretching method seems to be quite attractive. A detailed comparison of the performance of both methods in terms of computation time and image quality, however, is beyond the scope of this thesis.

Algorithm C.1. *Voxel-driven backprojection template employing a multiplicative processing scheme of the projection matrices.*

$\forall\, i, j, k : f\,[i, j, k] := 0$
for $l := 1, \ldots, L$ do
  calculate $\hat{\boldsymbol{P}}$ by equation (C.7)
  for $k := 1, \ldots, K$ do
    $x''' := \hat{p}_{13}\, k + \hat{p}_{14}$
    $y''' := \hat{p}_{23}\, k + \hat{p}_{24}$
    $z''' := \hat{p}_{33}\, k + \hat{p}_{34}$
    for $j := 1, \ldots, J$ do
      $x'' := \hat{p}_{12}\, j + x'''$
      $y'' := \hat{p}_{22}\, j + y'''$
      $z'' := \hat{p}_{32}\, j + z'''$
      calculate $i_{\min}$ and $i_{\max}$ †
      for $i := i_{\min}, \ldots, i_{\max}$ do
        $x' := \hat{p}_{11}\, i + x''$
        $y' := \hat{p}_{21}\, i + y''$
        $z' := \hat{p}_{31}\, i + z''$
        $\lambda^{-1} := 1/z_1$
        $\hat{u} := x'\, \lambda^{-1}$
        $\hat{v} := y'\, \lambda^{-1}$
        calculate $\tilde{g}$ by algorithm C.3 or C.4
        $f\,[i, j, k] := f\,[i, j, k] + \tilde{g}\ (\lambda^{-1})^2$
      end for i
    end for j
  end for k
end for l

† The interval $[i_{\min}, i_{\max}]$ comprises the indices of all image samples that are projected onto the valid detector range $[u_{\min}, u_{\max}] \times [v_{\min}, v_{\max}]$. This interval (of maximum width) is determined from $\hat{\boldsymbol{P}}$ such that $\forall\, i, i_{\min} \leq i \leq i_{\max}$

$$\begin{aligned} 1 \leq i \leq I\,, \quad & \hat{u}_{\min} \leq (\hat{p}_{11}\, i + x'')/\,(\hat{p}_{31}\, i + z'') \leq \hat{u}_{\max}\,, \\ \hat{p}_{31}\, i + z'' > 0\,, \quad & \hat{v}_{\min} \leq (\hat{p}_{21}\, i + y'')/\,(\hat{p}_{31}\, i + z'') \leq \hat{v}_{\max}\,. \end{aligned} \tag{C.11}$$

The ranges $[\hat{u}_{\min}, \hat{u}_{\max}]$ and $[\hat{v}_{\min}, \hat{v}_{\max}]$ are calculated according to the normalization of the original projection matrix $\boldsymbol{P}$. This transform is straightforward and therefore not documented here.

Algorithm C.2. *Voxel-driven backprojection template employing an additive processing scheme of the projection matrices.*

$\forall\, i, j, k : f\,[i, j, k] := 0$
for $l = 1, \ldots, L$ do
  calculate $\hat{\boldsymbol{P}}$ by equation (C.7)
  $x''' := \hat{p}_{13} + \hat{p}_{14}$
  $y''' := \hat{p}_{23} + \hat{p}_{24}$
  $z''' := \hat{p}_{33} + \hat{p}_{34}$
  for $k := 1, \ldots, K$ do
    $x'' := \hat{p}_{12} + x'''$
    $y'' := \hat{p}_{22} + y'''$
    $z'' := \hat{p}_{32} + z'''$
    for $j := 1, \ldots, J$ do
      calculate $i_{\min}$ and $i_{\max}$ †
      $x' := \hat{p}_{11}\, i_{\min} + x''$
      $y' := \hat{p}_{21}\, i_{\min} + y''$
      $z' := \hat{p}_{31}\, i_{\min} + z''$
      for $i := i_{\min}, \ldots, i_{\max}$ do
        $\lambda^{-1} := 1/z_1$
        $\hat{u} := x'\, \lambda^{-1}$
        $\hat{v} := y'\, \lambda^{-1}$
        calculate $\tilde{g}$ by algorithm C.3 or C.4
        $f\,[i, j, k] := f\,[i, j, k] + \tilde{g}\ \left(\lambda^{-1}\right)^2$
        $x' := x' + \hat{p}_{11}$
        $y' := y' + \hat{p}_{21}$
        $z' := z' + \hat{p}_{31}$
      end for i
      $x'' := x'' + \hat{p}_{12}$
      $y'' := y'' + \hat{p}_{22}$
      $z'' := z'' + \hat{p}_{32}$
    end for j
    $x''' := x''' + \hat{p}_{13}$
    $y''' := y''' + \hat{p}_{23}$
    $z''' := z''' + \hat{p}_{33}$
  end for k
end for l

Algorithm C.3. *Bilinear interpolation of the discrete projection data utilized in the backprojection templates of algorithm C.1 and algorithm C.2*

$m := \lfloor \hat{u} \rfloor$
$n := \lfloor \hat{v} \rfloor$

$\tilde{u} := \hat{u} - m$
$\tilde{v} := \hat{v} - n$

$g_{11} := g\,[l, m, n]$
$g_{12} := g\,[l, m+1, n]$
$g_{21} := g\,[l, m, n+1]$
$g_{22} := g\,[l, m+1, n+1]$

$g_1 := g_{11} + \tilde{u}\ (g_{12} - g_{11})$
$g_2 := g_{21} + \tilde{u}\ (g_{22} - g_{21})$

$\tilde{g} := g_1 + \tilde{v}\ (g_2 - g_1)$

Algorithm C.4. *Nearest-neighbour interpolation of the discrete projection data employed in the backprojection templates of algorithm C.1 and algorithm C.2*

$m^* := \lfloor \hat{u} \rceil + \lfloor \hat{v} \rceil$

$\tilde{g} := g\,[l, m^*]$

C.4 Reprojection

The standard ray-tracing method proposed by Siddon [110] is utilized to implement the reprojection step in iterative image reconstruction or restoration algorithms. Combining a voxel-driven backprojection with a ray-driven reprojection is an efficient technique that avoids cumulative discretization errors in iterative procedures [142].

Bibliography

[1] F. E. A. F. Ali, Z. Nakao, Y.-W. Chen, K. Matsuo, I. Ohkawa. An adaptive backpropagation algorithm for limited angle CT image reconstruction. *IEICE Trans. Fundament.*, E83-A(6), 2000.

[2] J. Ambrose. Computerized transverse axial scanning (tomography): Part 2. Clinical application. *Brit. J. Radiol.*, 46(552):1023–1047, 1973.

[3] S. G. Azevedo, D. J. Schneberk, J. P. Fitch, H. E. Martz. Calculation of the rotational centers in computed tomography sinograms. *IEEE Trans. Nucl. Science*, 37(4):1525–1540, 1990.

[4] J. Balter, H. Sandler, K. Lam, R. Bree, A. Lichter, R. Ten Haken. Measurement of prostate movement over the course of routine radiotherapy using implanted markers. *Int. J. Radiat. Oncol. Biol. Phys.*, 31(1):113–118, 1995.

[5] J. M. Balter, K. L. Lam, H. M. Sandler, J. F. Littles, R. L. Bree, R. K. Ten Haken. Automated localization of the prostate at the time of treatment using implanted radiopaque markers: technical feasibility. *Int. J. Radiat. Oncol. Biol. Phys.*, 33(5):1281–1286, 1995.

[6] H. H. Barrett. The Radon transform and its applications. In E. Wolf, editor, *Progress in Optics*, volume 21, pages 218–285. Elsevier Science Publishers B.V., 1984.

[7] H. H. Barrett. Editorial: Limited-angle tomography for the nineties. *J. Nucl. Medicine*, 31(10):1688–1692, 1990.

[8] R. N. Bracewell. Strip integration in radio-astronomy. *Aust. J. Phys.*, 9:198–217, 1956.

[9] R. N. Bracewell, A. C. Riddle. Inversion of fan-beam scans in radio-astronomy. *Astrophys. J.*, 150:427–434, 1967.

[10] I. N. Bronstein, K. A. Semendjajew. *Taschenbuch der Mathematik.* B. G. Teubner Verlagsgesellschaft, Verlag Nauka, Leipzig, Moskau, 1983.

[11] T. Brückner, R. Lucht, G. Brix. Comparison of rigid and elastic matching of dynamic magnetic resonance mammographic images by mutual information. *Med. Phys.*, 27(10):2456–2461, 2000.

[12] A. Brunetti, B. Golosio. A new algorithm for computer tomographic reconstruction from partial view projections. *Med. Phys.*, 28(4):462–468, 2001.

[13] J. Chen. A theoretical framework of regional cone-beam tomography. *IEEE Trans. Med. Imag.*, 11(3):342–350, 1992.

[14] P. S. Cho, R. H. Johnson, T. W. Griffin. Cone-beam CT for radiotherapy applications. *Phys. Med. Biol.*, 40(11):1863–1883, 1995.

[15] A. M. Cormack. Representation of a function by its line integrals, with some radiological applications. *J. Appl. Phys.*, 34:2722–2727, 1963.

[16] M. Defrise. A short reader's guide to 3D tomographic reconstruction. *Comp. Med. Imag. Graph.*, 25:113–116, 2001.

[17] M. Defrise, R. Clack. A cone-beam reconstruction algorithm using shift-variant filtering and cone-beam backprojection. *IEEE Trans. Med. Imag.*, 13(1):186–195, 1994.

[18] M. Defrise, R. Clack. Filtered backprojection reconstruction of combined parallel beam and cone beam SPECT data. *Phys. Med. Biol.*, 40(9):1517–1537, 1995.

[19] M. Defrise, F. Noo, H. Kudo. A solution to the long-object problem in helical cone-beam tomography. *Phys. Med. Biol.*, 45(3):623–643, 2000.

[20] P. Dreike, D. P. Boyd. Convolution reconstruction of fan beam projections. *Comp. Graph. Imag. Proc.*, 5:459–469, 1976.

[21] M. Ebert, B. A. Groh, M. Partridge, B. M. Hesse, T. Bortfeld. 3D image guidance in radiotherapy: a feasibility study. In M. Sonka, K. M. Hanson, editors, *Proc. SPIE Med. Imag.*, volume 4322, pages 1807–1816, 2001.

[22] R. Fahrig, A. J. Fox, D. W. Holdsworth. Characterization of a C-arm-mounted XRII for 3D image reconstruction during interventional neuroradiology. In Van Metter and Beutel [125], pages 351–360.

[23] R. Fahrig, M. Moreau, D. W. Holdsworth. Three-dimensional computed tomographic reconstruction using a C-arm mounted XRII: Correction of image intensifier distortion. *Med. Phys.*, 24(7):1097–1106, 1997.

[24] L. A. Feldkamp, L. C. Davis, J. W. Kress. Practical cone-beam algorithm. *J. Opt. Soc. Amer. A*, 1(6):612–619, 1984.

[25] D. V. Finch. Cone beam reconstruction with sources on a curve. *SIAM J. Appl. Math.*, 45(4):665–673, 1985.

[26] E. E. Fitchard, J. S. Aldridge, P. J. Reckwerdt, T. R. Mackie. Registration of synthetic tomographic projection data sets using cross-correlation. *Phys. Med. Biol.*, 43(6):1645–1657, 1998.

[27] R. W. Gerchberg. Super-resoluation through error energy reduction. *Opt. Acta*, 21(9):709–720, 1974.

[28] P. Gilbert. Iterative methods for three-dimensional reconstruction of an object from projections. *J. Theor. Biol.*, 36:105–117, 1972.

[29] K. G. A. Gilhuijs, P. J. H. van de Ven, M. van Herk. Automatic three-dimensional inspection of patient setup in radiation therapy using portal images, simulator images and computed tomography data. *Med. Phys.*, 23(3):389–399, 1996.

[30] A. L. Goertzen, F. J. Beekman, S. R. Cherry. Effect of voxel size in CT simulations. In *2000 IEEE NSS – MIC, Book of Abstracts*, Lyon, France, 2000.

[31] R. Gordon, R. M. Rangayyan. Geometric deconvolution: A meta-algorithm for limited view computed tomography. *IEEE Trans. Biomed. Eng.*, BME-30(12):806–810, 1983.

[32] P. Grangeat. Mathematical framework of cone beam 3D reconstruction via the first derivative of the Radon transform. In Herman, Louis, Natterer, editors, *Lecture Notes in Mathematics*, pages 66–97. Springer-Verlag, Berlin, 1991.

[33] M. Grass, T. Köhler, R. Proska. 3D cone-beam CT reconstruction for circular trajectories. *Phys. Med. Biol.*, 45(2):329–347, 2000.

[34] M. Grass, R. Koppe, E. Klotz, R. Proska, M. H. Kuhn, H. Aerts, J. O. de Beek, R. Kemkers. Three-dimensional reconstruction of high contrast objects using C-arm image intensifier projection data. *Comp. Med. Imag. Graph.*, 23:311–321, 1999.

[35] E. Gronenschild. The accuracy and reproducibility of a global method to correct for geometric image distortion in the x-ray imaging chain. *Med. Phys.*, 24(12):1875–1888, 1997.

[36] H. Guan, R. Gordon. Computed tomography using algebraic reconstruction techniques (ARTs) with different projection access schemes: a comparison study under practical situations. *Phys. Med. Biol.*, 41(9):1727–1743, 1996.

[37] G. T. Gullberg, C. R. Crawford, B. M. W. Tsui. Reconstruction algorithm for fan beam with a displaced center-of-rotation. *IEEE Trans. Med. Imag.*, MI-5(1):23–29, 1986.

[38] G. T. Gullberg, B. M. W. Tsui, C. R. Crawford, J. G. Ballard, J. T. Hagius. Estimation of geometrical parameters and collimator evaluation for cone beam tomography. *Med. Phys.*, 17(2):264–272, 1990.

[39] G. T. Gullberg, B. M. W. Tsui, C. R. Crawford, E. R. Edgerton. Estimation of geometrical parameters for fan beam tomography. *Phys. Med. Biol.*, 32(12):1581–1594, 1987.

[40] K. M. Hanson, G. W. Wecksung. Bayesian approach to limited-angle reconstruction in computed tomography. *J. Opt. Soc. Amer. A*, 73(11):1501–1509, 1983.

[41] G. T. Herman. *Image Reconstruction from Projections. The fundamentals of Computerized Tomography.* Academic Press, New York, London, Toronto, Sydney, San Francisco, 1980.

[42] B. M. Hesse, L. Spies, B. A. Groh. Tomotherapeutic portal imaging for radiation treatment verification. *Phys. Med. Biol.*, 43(12):3607–3616, 1998.

[43] G. N. Hounsfield. Computerized transverse axial scanning (tomography): Part 1. Description of system. *Brit. J. Radiol.*, 46(552):1016–1022, 1973.

[44] H. Hu. Multi-slice helical CT: Scan and reconstruction. *Med. Phys.*, 26(1):5–18, 1999.

[45] D. A. Jaffray, D. G. Drake, M. Moreau, A. A. Martinez, J. W. Wong. A radiographic and tomographic imaging system integrated into a medical linear accelerator for localization of bone and soft-tissue targets. *Int. J. Radiat. Oncol. Biol. Phys.*, 45(3):773–789, 1999.

[46] P. M. Joseph, R. A. Schulz. View sampling requirements in fan beam computed tomography. *Med. Phys.*, 7(6):692–702, 1980.

[47] M. Kachelriess, W. A. Kalender. Electrocardiogram-correlated image reconstruction from subsecond spiral computed tomography scans of the heart. *Med. Phys.*, 25(12):2417–2431, 1998.

[48] S. Kaczmarz. Angenäherte Auflösung von Systemen linearer Gleichungen. *Bull. Acad. Pol. Sci. Lett. A*, 6(8):355–357, 1937.

[49] A. C. Kak, M. Slaney. *Principles of computerized tomographic imaging.* IEEE Press, 1999.

[50] W. A. Kalender. *Computertomographie – Grundlagen, Gerätetechnologie, Bildqualität, Anwendungen.* Publicis MCD Verlag, München, 2000.

[51] W. A. Kalender, A. Polacin. Physical performance characteristics of spiral CT scanning. *Med. Phys.*, 18(5):910–915, 1991.

[52] W. A. Kalender, A. Polacin, C. Süß. A comparison study of conventional and spiral CT: An experimental study on the detection of spherical lesions. *J. Comp. Assist. Tomogr.*, 18(2):167–176, 1994.

[53] W. A. Kalender, W. Seissler, E. Klotz, P. Vock. Spiral volumetric CT with single-breath-hold technique, continuous transport, and continuous scanner rotation. *Radiology*, 176(1):181–183, 1990.

[54] J. H. Kim, K. Y. Kwak, S. B. Park, Z. Cho. Projection space iteration reconstruction-reprojection. *IEEE Trans. Med. Imag.*, MI-4(3):139–143, 1985.

[55] H. Kudo, F. Noo, M. Defrise. Cone-beam filtered-backprojection algorithm for truncated helical data. *Phys. Med. Biol.*, 43(10):2885–2909, 1998.

[56] H. Kudo, S. Park, F. Noo, M. Defrise. Performance of quasi-exact cone-beam filtered-backprojection algorithm for axially truncated helical data. *IEEE Trans. Nucl. Science*, 46:608–617, 1999.

[57] H. Kudo, T. Saito. Feasible cone beam scanning methods for exact reconstruction in three-dimensional tomography. *J. Opt. Soc. Amer. A*, 7(12):2169–2183, 1990.

[58] H. Kudo, T. Saito. Derivation and implementation of a cone-beam reconstruction algorithm for nonplanar orbits. *IEEE Trans. Med. Imag.*, 13(1):196–211, 1994.

[59] H. Kudo, T. Saito. Fast and stable cone-beam filtered backprojection method for non-planar orbits. *Phys. Med. Biol.*, 43(4):747–760, 1998.

[60] L. Leksell. The stereotaxic method and radiosurgery of the brain. *Acta Chirurg. Scandinav.*, 231:316–319, 1951.

[61] A. Lent, H. Tuy. An iterative method for the extrapolation of band-limited functions. *J. Math. Anal. Appl.*, 83:554–565, 1981.

[62] J. Li, R. J. Jaszczak, K. L. Greer, R. E. Coleman. A filtered backprojection algorithm for pinhole SPECT with a displaced centre of rotation. *Phys. Med. Biol.*, 39(1):165–176, 1994.

[63] J. Li, R. J. Jaszczak, H. Wang. A cone beam SPECT reconstruction algorithm with a displaced center of rotation. *Med. Phys.*, 21(1):145–152, 1994.

[64] J. Li, R. J. Jaszczak, H. Wang, K. L. Greer, R. E. Coleman. Determination of both mechanical and electronic shifts in cone beam SPECT. *Phys. Med. Biol.*, 38(6):743–754, 1993.

[65] S. Loose, K. W. Leszcynski. On few-view tomographic reconstruction with megavoltage photon beams. *Med. Phys.*, 28(8):1679–1688, 2001.

[66] A. K. Louis. Picture reconstruction from projections in restricted range. *Math. Meth. Appl. Sci.*, 2:209–220, 1980.

[67] A. K. Louis. *Inverse und schlecht gestellte Probleme.* B. G. Teubner, Stuttgart, 1989.

[68] F. Maes, A. Collignon, D. Vandermeulen, G. Marchal, P. Suetens. Multimodality image registration by maximization of mutual information. *IEEE Trans. Med. Imag.*, 16(2):187–198, 1997.

[69] B. P. Medoff, W. R. Brody, M. Nassi, A. Macovski. Iterative convolution backprojection algorithms for image reconstruction from limited data. *J. Opt. Soc. Amer. A*, 73(11):1493–1500, 1983.

[70] T. Melen. *Geometrical Modelling and Calibration of Video Cameras for Underwater Navigation.* PhD thesis, Institutt teknisk kybernetikk, Norges tekniske høgskole, Trondheim, Norway, 1994.

[71] K. Meyer-Waarden. *Bioelektrische Signale und ihre Ableitverfahren.* Schattauer, Stuttgart, New York, 1985.

[72] S. Midgley, R. M. Millar, J. Dudson. A feasibility study for megavoltage cone beam CT using a commercial EPID. *Phys. Med. Biol.*, 43(1):155–169, 1998.

[73] M. A. Mosleh-Shirazi, P. M. Evans, W. Swindell, S. Webb, M. Partridge. A cone-beam megavoltage CT scanner for treatment verification in conformal radiotherapy. *Radiother. Oncol.*, 48:319–328, 1998.

[74] M. J. Murphy. An automatic six-degree-of-freedom image registration algorithm for image-guided frameless stereotaxic radiosurgery. *Med. Phys.*, 24(6):857–866, 1997.

[75] A. Naparstek. Short-scan fan-beam algorithms for CT. *IEEE Trans. Nucl. Science*, NS-27:1112–1120, 1980.

[76] M. Nassi, W. R. Brody, B. P. Medoff, A. Macovski. Iterative reconstruction-reprojection: An algorithm for limited data cardiac-computed tomography. *IEEE Trans. Biomed. Eng.*, BME-29(5):333–341, 1982.

[77] F. Natterer. *The mathematics of computerized tomography.* B. G. Teubner, Stuttgart, 1986.

[78] F. Natterer. Numerical methods in tomography. In A. Iserles, editor, *Acta Numerica 1999.* Cambridge University Press, 1999.

[79] N. Navab, A. R. Bani-Hashemi, M. Mitschke, D. W. Holdsworth, R. Fahrig, A. J. Fox, R. Graumann. Dynamic geometrical calibration for 3D cerebral angiography. In Van Metter and Beutel [125], pages 361–370.

[80] F. Noo, R. Clack, M. Defrise. Cone-beam reconstruction from general discrete vertex sets using Radon rebinning algorithms. *IEEE Trans. Nucl. Science*, 44(3):1309–1316, 1997.

[81] F. Noo, R. Clackdoyle, C. Mennessier, T. A. White, T. J. Roney. Analytic method based on identification of ellipse parameters for scanner calibration in cone-beam tomography. *Phys. Med. Biol.*, 45(11):3489–3508, 2000.

[82] F. Noo, M. Defrise, R. Clackdoyle. Single-slice rebinning method for helical cone-beam CT. *Phys. Med. Biol.*, 44(2):561–570, 1999.

[83] P. Oskoui-Fard, H. Stark. Tomographic image reconstruction using the theory of convex projections. *IEEE Trans. Med. Imag.*, 7(1):45–58, 1988.

[84] A. Papoulis. A new algorithm in spectral analysis and band-limited extrapolation. *IEEE Trans. Circ. Syst.*, CAS-22(9):735–742, 1975.

[85] D. L. Parker. Optimal short scan convolution reconstruction for fan-beam CT. *Med. Phys.*, 9(2):254–257, 1982.

[86] J. Pavkovich. Apparatus and method for reconstructing data. U.S. Patent 4,149,248, 1979.

[87] H. Peng, H. Stark. Direct fourier reconstruction in fan-beam tomography. *IEEE Trans. Med. Imag.*, MI-6(3):209–219, 1987.

[88] H. Peng, H. Stark. One-step image reconstruction from incomplete data in computer tomography. *IEEE Trans. Med. Imag.*, 8(1):16–31, 1989.

[89] H. Peng, H. Stark. Image recovery in computer tomography from partial fan-beam data by convex projections. *IEEE Trans. Med. Imag.*, 11(4):470–478, 1992.

[90] T. M. Peters. Algorithms for fast back- and re-projection in computed tomography. *IEEE Trans. Nucl. Science*, NS-28(4):3641–3647, 1981.

[91] A. Polacin, W. A. Kalender, G. Marchal. Evaluation of section sensitivity profiles and image noise in spiral CT. *Radiology*, 185(1):29–35, 1992.

[92] W. H. Press, S. A. Teukolsky, W. T. Vetterling, B. P. Flannery. *Numerical Recipes in C. The Art of Scientific Computing.* Cambridge University Press, 2nd edition, 1992.

[93] J. H. Radon. Über die Bestimmung von Funktionen durch ihre Integralwerte längs gewisser Mannigfaltigkeiten. In *Ber. Sächs. Akad. Wiss. Math.-phys. Klasse*, volume 69, pages 262–277, Leipzig, 1917. B. G. Teubner.

[94] R. Rangayyan, A. P. Dhawan, R. Gordon. Algorithms for limited-view computed tomography: an annotated bibliography and a challenge. *Appl. Opt.*, 24(23):4000–4012, 1985.

[95] T. Riechert, F. Mundinger. Beschreibung und Anwendung eines Zielgerätes für stereotaktische Hirnoperationen (II. Modell). *Acta Neurochirurg.*, Suppl. 3:308–337, 1955.

[96] P. Rizo, P. Grangeat, R. Guillemaud. Geometric calibration method for multiple-head cone-beam SPECT system. *IEEE Trans. Nucl. Science*, 41(6):2748–2757, 1994.

[97] D. W. O. Rogers. Fluence to dose equivalent conversion factors calculated with EGS3 for electrons from 100 keV to 20 GeV and photons from 11 keV to 20 GeV. *Health Physics*, 46:891–914, 1984.

[98] A. Roguée, C. Picard, C. Ponchut, Y. Trousset. Geometrical calibration of X-ray imaging chains for three-dimensional reconstruction. *Comp. Med. Imag. Graph.*, 17(4/5):295–300, 1993.

[99] A. Roguée, C. Picard, Y. Trousset, C. Ponchut. Geometrical calibration for 3D X-ray imaging. In *Proc. SPIE Med. Imag.*, volume 1897, pages 161–169, 1993.

[100] K. J. Ruchala, G. H. Olivera, E. A. Schloesser, R. Hinderer, T. R. Mackie. Calibration of a tomotherapeutic MVCT system. *Phys. Med. Biol.*, 45(4):N27–N36, 2000.

[101] K. J. Ruchala, G. H. Olivera, E. A. Schloesser, T. R. Mackie. Megavoltage CT on a tomotherapy system. *Phys. Med. Biol.*, 44(10):2597–2621, 1999.

[102] T. Sato, S. J. Norton, M. Linzer, O. Ikeda, M. Hirama. Tomographic image reconstruction from limited projections using iterative revisions in image and transform spaces. *Appl. Opt.*, 20(3):395–399, 1981.

[103] R. W. Schafer, R. M. Mersereau, M. A. Richards. Constrained iterative restoration algorithms. *Proc. IEEE*, 69(4):432–450, 1981.

[104] S. Schaller, F. Noo, F. Sauer, K. C. Tam, G. Lauritsch, T. Flohr. Exact Radon rebinning algorithm for the long object problem in helical cone-beam CT. *IEEE Trans. Med. Imag.*, 19(5):361–375, 2000.

[105] R. F. Schmidt, G. Thews, editors. *Physiologie des Menschen.* Springer, Berlin, Heidelberg, New York, London, Paris, Tokyo, Hong Kong, Barcelona, Budapest, 26. Aufl. edition, 195.

[106] D.-A. Sennst. EKG-Signalverarbeitung für die computertomographische Herzbildgebung. Studienarbeit, Universität Heidelberg, Fachhochschule Heilbronn, 1999.

[107] M. I. Sezan, H. Stark. Image restoration by the method of convex projections: Part 2 – Applications and numerical results. *IEEE Trans. Med. Imag.*, MI-1(2):95–101, 1982.

[108] M. I. Sezan, H. Stark. Tomographic image reconstruction from incomplete view data by convex projections and direct fourier inversion. *IEEE Trans. Med. Imag.*, MI-3(2):91–98, 1984.

[109] L. A. Shepp, B. F. Logan. The fourier reconstruction of a head section. *IEEE Trans. Nucl. Science*, NS-21(3):21–43, 1974.

[110] R. L. Siddon. Fast calculation of the exact radiological path for a three-dimensional CT array. *Med. Phys.*, 12(2):252–255, 1985.

[111] M. D. Silver. A method for including redundant data in computed tomography. *Med. Phys.*, 27(4):773–774, 2000.

[112] B. D. Smith. Image reconstruction from cone-beam projections: Necessary and sufficient conditions and reconstruction methods. *IEEE Trans. Med. Imag.*, 4(1):14–25, 1985.

[113] P. R. Smith, T. M. Peters, R. H. T. Bates. Image reconstruction from a finite number of projections. *J. Phys.*, A6:361–382, 1973.

[114] L. Spies, M. Ebert, B. A. Groh, B. M. Hesse, T. Bortfeld. Correction of scatter in megavoltage cone beam CT. *Phys. Med. Biol.*, 46(3):821–833, 2001.

[115] H. Stark, D. Cahana, H. Webb. Restoration of arbitrary finite-energy optical objects from limited spatial and spectral information. *J. Opt. Soc. Amer. A*, 71(6):635–642, 1981.

[116] H. Stark et al. An investigation of computerized tomography by direct Fourier inversion and optimum interpolation. *IEEE Trans. Biomed. Eng.*, BME-28:496–505, 1981.

[117] W. Swindell. A 4-MV CT scanner for radiation therapy; spectral properties of the therapy beam. *Med. Phys.*, 10(3):347–351, 1983.

[118] W. Swindell, P. M. Evans. Scattered radiation in portal images: A Monte Carlo simulation and a simple physical model. *Med. Phys.*, 23(1):63–73, 1996.

[119] W. Swindell, R. G. Simpson, J. R. Oleson, C.-T. Chen, E. A. Grubbs. Computed tomography with a linear accelerator with radiotherapy applications. *Med. Phys.*, 10(4):416–420, 1983.

[120] K. C. Tam, G. Lauritsch, K. Sourbelle, F. Sauer, B. Ladendorf. Exact (spiral + circles) scan region-of-interest cone beam reconstruction via backprojection. *IEEE Trans. Med. Imag.*, 19(5):376–383, 2000.

[121] K. C. Tam, V. Perez-Mendez. Tomographical imaging with limited-angle input. *J. Opt. Soc. Amer. A*, 71(5):582–592, 1981.

[122] K. C. Tam, S. Samarasekera, F. Sauer. Exact cone-beam CT with a spiral scan. *Phys. Med. Biol.*, 43(4):1015–1024, 1998.

[123] H. Turbell. *Cone-Beam Reconstruction Using Filtered Backprojection.* PhD thesis, Institute of Technology, Linköpings universitet, Sweden, 2001.

[124] H. K. Tuy. An inversion formula for cone-beam reconstruction. *SIAM J. Appl. Math.*, 43(3):546–552, 1983.

[125] R. L. Van Metter, J. Beutel, editors. *Proc. SPIE Med. Imag., Physics of Medical Imaging*, volume 2708, 1996.

[126] L. J. Verhey. Immobilizing and positioning patients for radiotherapy. *Sem. Radiat. Oncol.*, 5(2):100–114, 1995.

[127] S. Vollmar, W. Eschner, K. Wienhard, U. Pietrzyk. Iterative reconstruction of emission tomography data with a-priori-information. In *Proc. Int. Meeting Fully 3D Image Reconstr.*, pages 135–136, Egmond aan Zee, The Netherlands, 1999.

[128] G. Wang, T.-H. Lin, P.-c. Cheng, D. M. Shinozaki. A general cone-beam reconstruction algorithm. *IEEE Trans. Med. Imag.*, 12(3):486–496, 1993.

[129] H. Wang, M. F. Smith, C. D. Stone, R. J. Jaszczak. Astigmatic single photon emission computed tomography imaging with a displaced center of rotation. *Med. Phys.*, 25(8):1493–1501, 1998.

[130] S. Webb. *From the watching of shadows: the origins of radiological tomography.* IOP Publishing Ltd, Bristol, New York, 1990.

[131] Y. Weng, G. L. Zeng, G. T. Gullberg. A reconstruction algorithm for helical cone-beam SPECT. *IEEE Trans. Nucl. Science*, 40:1092–1101, 1993.

[132] S. Wesarg, M. Ebert, T. Bortfeld. Parker weights revisited. *Med. Phys.*, 2001. Submitted.

[133] K. Wiesent, K. Barth, N. Navab, T. Brunner, W. Seissler. Enhanced 3D-reconstruction algorithms for C-arm based interventional procedures. In *Proc. Int. Meeting Fully 3D Image Reconstr.*, Egmond aan Zee, The Netherlands, 1999.

[134] K. Wiesent, K. Barth, N. Navab, P. Durlak, T. Brunner, O. Schuetz, W. Seissler. Enhanced 3-D-reconstruction algorithm for C-arm sys-

tems suitable for interventional procedures. *IEEE Trans. Med. Imag.*, 19(5):391–403, 2000.

[135] M. J. Yaffe, J. A. Rowlands. X-ray detectors for digital radiography. *Phys. Med. Biol.*, 42(1):1–39, 1997.

[136] A. E. Yagle. An explicit closed-form solution to the limited-angle discrete tomography problem for finite-support objects. *Int. J. Imag. Syst. Technol.*, 9:174–180, 1998.

[137] X.-h. Yan, R. M. Leahy. Cone-beam tomography with circular, elliptical and spiral orbits. *Phys. Med. Biol.*, 37(3):493–506, 1992.

[138] D. C. Youla. Generalized image reconstruction by the method of alternating orthogonal projections. *IEEE Trans. Circ. Syst.*, CAS-25(9):694–702, 1978.

[139] D. C. Youla, H. Webb. Image restoration by the method of convex projections: Part 1 – Theory. *IEEE Trans. Med. Imag.*, MI-1(2):81–94, 1982.

[140] G. L. Zeng, R. Clack, G. T. Gullberg. Implementation of Tuy's cone-beam inversion formula. *Phys. Med. Biol.*, 39(3):493–507, 1994.

[141] G. L. Zeng, G. T. Gullberg. A cone-beam tomography algorithm for orthogonal circle-and-line orbit. *Phys. Med. Biol.*, 37(3):563–577, 1992.

[142] G. L. Zeng, G. T. Gullberg. Unmachted projector/backprojector pairs in an iterative reconstruction algorithm. *IEEE Trans. Med. Imag.*, 19(5):548–555, 2000.